LEIBNIZ-INSTITUT
FÜR
ATMOSPHÄREN
PHYSIK

INAUGURAL-DISSERTATION

am Leibniz-Institut für Atmosphärenphysik in Kühlungsborn
zur Erlangung der Doktorwürde
der Mathematisch-Naturwissenschaftlichen Fakultät
der Universität Rostock

Multi-frequency radar observations of polar mesosphere summer echoes: Statistical properties and microphysical results

von

Qiang Li

Abstract: During the years between 2003 - 2007 and in June 2006 measurements of polar mesosphere summer echoes (PMSE) have been performed with the EISCAT VHF and UHF radar (69°N, 19°E) and with the EISCAT Svalbard radar (ESR) and the SOUSY Svalbard radar (SSR, 78°N, 16°E), respectively. Based on these measurements, this thesis concentrates on the frequency dependence of PMSE properties. It starts with an investigation of statistical properties of PMSE at the considered frequencies and then turns to a test of our current understanding and to the determination of microphysical parameters from the observations. The currently most widely accepted theory of PMSE assumes that the echoes originate from turbulence-induced scatter in combination with an enhanced Schmidt number due to the presence of charged ice particles. Therefore, the radar scattering should either come from a spectral range dominated by a k^{-3}-dependence (where k is the wavenumber) or from a spectral range which is dominated by an exponential decay at the smallest spatial scales (i.e., the viscous-convective subrange or the viscous-diffusive subrange). This means that the reflectivity ratio of measurements at two frequencies should be equal to or larger than the ratio of the radar frequencies to the third power. Our experimental results show that more than 94% of the observations are in full accord with this expectation. Based on the above mentioned theory, a new algorithm has been developed to calculate Schmidt numbers and hence radii of the charged ice particles from the volume reflectivity ratios of PMSE simultaneously observed at two well-separated frequencies. We have applied this exercise to the calibrated observations with the above mentioned radars. The resulting particle radii display excellent agreement with expectations from microphysical models and independent observations with satellite and ground-based lidar instruments.

Postal address:
Schloss-Str. 6
18225 Kühlungsborn
Germany

IAP Kühlungsborn
October 2011
IAP Nr. 29/2011
ISSN 1615-8083

LEIBNIZ-INSTITUT
FÜR
ATMOSPHÄREN
PHYSIK
IAP

Multi-frequency radar observations of polar mesosphere summer echoes: Statistical properties and microphysical results

Dissertation
zur
Erlangung des akademischen Grades
doctor rerum naturalium (Dr. rer. nat.)
der Mathematisch-Naturwissenschaftlichen Fakultät
der Universität Rostock

vorgelegt von
Qiang Li, geb. am 17.06.1979 in Hebei, China
aus Rostock

Rostock, 18.03.2011

Gutachter: Prof. Dr. Markus Rapp (Universität Rostock)
Prof. Dr. Tom A. Blix (Universität Oslo, Norwegen)

verteidigt am: 21.10.2011

urn:nbn:de:gbv:28-diss2011-0173-2

Abstract

During the years between 2003 - 2007 and in June 2006 measurements of polar mesosphere summer echoes (PMSE) have been performed with the EISCAT VHF and UHF radar (69°N, 19°E) and with the EISCAT Svalbard radar (ESR) and the SOUSY Svalbard radar (SSR, 78°N, 16°E), respectively. Based on these measurements, this thesis concentrates on the frequency dependence of PMSE properties. It starts with an investigation of statistical properties of PMSE at the considered frequencies and then turns to a test of our current understanding and to the determination of microphysical parameters from the observations. The currently most widely accepted theory of PMSE assumes that the echoes originate from turbulence-induced scatter in combination with an enhanced Schmidt number due to the presence of charged ice particles. Therefore, the radar scattering should either come from a spectral range dominated by a k^{-3}-dependence (where k is the wavenumber) or from a spectral range which is dominated by an exponential decay at the smallest spatial scales (i.e., the viscous-convective subrange or the viscous-diffusive subrange). This means that the reflectivity ratio of measurements at two frequencies should be equal to or larger than the ratio of the radar frequencies to the third power. Our experimental results show that more than 94% of the observations are in full accord with this expectation. Based on the above mentioned theory, a new algorithm has been developed to calculate Schmidt numbers and hence radii of the charged ice particles from the volume reflectivity ratios of PMSE simultaneously observed at two well-separated frequencies. We have applied this exercise to the calibrated observations with the above mentioned radars. The resulting particle radii display excellent agreement with expectations from microphysical models and independent observations with satellite and ground-based lidar instruments.

Zusammenfassung

Im Zeitraum von 2003 - 2007 bzw. im Sommer 2006 wurden Beobachtungen von polaren mesosphärischen Sommerechos (PMSE) mit dem EISCAT VHF- und UHF-Radar (69°N, 19°O) bzw. dem EISCAT Svalbard-Radar (ESR) und dem SOUSY Svalbard-Radar (SSR, 78°N, 16°O) durchgeführt. Im Fokus dieser Untersuchungen steht die Frequenzabhängigkeit der Eigenschaften von PMSE. In einem ersten Schritt werden statistische Eigenschaften der Echos bei verschiedenen Frequenzen bestimmt, wonach der Fokus dann auf die Überprüfung unseres physikalischen Verständnisses und der Ableitung mikrophysikalischer Parameter gelegt wird. Im Rahmen einer derzeit allgemeinen akzeptierten Theorie von PMSE wird angenommen, dass die Echos aus turbulenzinduzierter Streuung in Kombination mit einer erhöhten Schmidt-Zahl aufgrund der Anwesenheit von geladenen Eispartikeln entstehen. Demzufolge sollte die Radarstreuung entweder aus einem spektralen Bereich herrühren, der von einer k^{-3}-Abhängigkeit dominiert wird (dem sogenannten viskos-konvektiven Unterbereich), oder von einem Spektralbereich, der von einem exponentiellen Abfall bei den kleinsten räumlichen Skalen (dem sogenannten viskos-diffusen Unterbereich) dominiert wird (dabei ist k die Wellenzahl). Dies bedeutet, dass das Reflektivitätsverhältnis von Messungen bei zwei Frequenzen gleich dem oder größer als das Verhältnis der Radarfrequenzen zur dritten Potenz sein sollte. Unsere experimentellen Ergebnisse zeigen, dass mehr als 94% der Beobachtungen in Übereinstimmung mit dieser Erwartung sind. Basierend auf der zuvor erwähnten Theorie wurde ein neuer Algorithmus entwickelt, um Schmidt-Zahlen und somit Radien der geladenen Eispartikel aus den Volumenreflektivitätsverhältnissen von PMSE zu berechnen, die bei zwei wesentlich unterschiedlichen Frequenzen simultan beobachtet wurden. Diese Methode wurde auf kalibrierte Beobachtungen mit den oben erwähnten Radars angewandt. Die resultierenden Partikelradien zeigen sowohl eine ausgezeichnete Übereinstimmung mit den Erwartungen aus mikrophysikalischen Modellen als auch mit unabhängigen Beobachtungen von Satelliten und bodengestützten Lidargeräten.

Contents

1 Introduction **3**

1.1 Vertical structure of the atmosphere . . . 3

1.2 Mesosphere and lower thermosphere region . . . 4

1.3 Overview of PMSE . . . 7

1.4 Objectives and structure of this thesis . . . 9

2 Observational results regarding PMSE **11**

2.1 History . . . 11

2.2 Morphology . . . 11

2.3 Climatology . . . 13

2.4 Frequency dependence . . . 15

2.5 Factors leading to PMSE . . . 16

2.5.1 Ice particles . . . 16

2.5.2 Electron number density . . . 18

2.5.3 Turbulence . . . 19

3 Theory **23**

4 Experimental facilities and data sets **29**

4.1 Incoherent scatter radars . . . 29

4.2 The EISCAT VHF and UHF radar . . . 30

4.2.1 Configuration . . . 31

4.2.2 Data . . . 31

4.3 The ESR and the SSR . . . 32

4.3.1 Configuration . . . 33

4.3.2 Data . . . 34

5 Results: statistical properties of PMSE **35**

5.1 Observations at frequencies of 53.5 and 500 MHz . . . 35

5.1.1 PMSE occurrence rates . . . 35

5.1.2 Volume reflectivities . . . 38

5.2 Observations at frequencies of 224 and 930 MHz . . . 39

5.2.1 PMSE-occurrence rates . . . 40

5.2.2 Volume reflectivities . . . 41

5.3 Temporal variability of PMSE at 224 MHz . . . 41

5.3.1 Year-to-year variation . . . 43

5.3.2 Seasonal variation . . . 46

5.3.3 Diurnal variation . . . 49

6 Results: factors leading to UHF PMSE **53**
6.1 Introduction . . . 53
6.2 Turbulence parameters . . . 53
6.2.1 Comparisons between the ESR and SSR . . . 54
6.2.2 Comparisons between the EISCAT VHF and UHF radar . . . 59
6.3 Electron densities . . . 61

7 Results: microphysical parameters derived from radar observations **65**
7.1 Test of the TWLS-theory . . . 66
7.2 Microphysical parameters derived from radar measurements . . . 68
7.2.1 Measurements with the ESR and SSR . . . 70
7.2.2 Measurements with the EISCAT VHF and UHF radar . . . 72
7.2.3 Comparison to SOFIE results . . . 74
7.3 Summary . . . 77

8 Results: electron densities in the presence of PMSE **79**
8.1 Introduction . . . 79
8.2 Method to derive Λ from the radar observations . . . 81
8.3 Statistical results of electron densities in the presence of PMSE . . . 83

9 Conclusions and outlook **85**
9.1 Conclusions . . . 85
9.2 Outlook . . . 87

A Tables **91**

B List of abbreviations **95**

Chapter 1

Introduction

1.1 Vertical structure of the atmosphere

The terrestrial atmosphere surrounding the Earth is a complex natural laboratory composed of a variety of gases and suspended aerosols which is essential for respiration and protects life from outer space. In the atmosphere, molecular nitrogen (N_2) and molecular oxygen (O_2) predominate by volume – they occupy 78% and 21%, respectively – whereas the minor constituents e.g., carbon dioxide, water vapor, ozone and aerosols play a crucial role in the thermal and dynamical structure of the atmosphere. In addition, the atmosphere is host to various physical and chemical processes that determine the distribution of the atmospheric constituents.

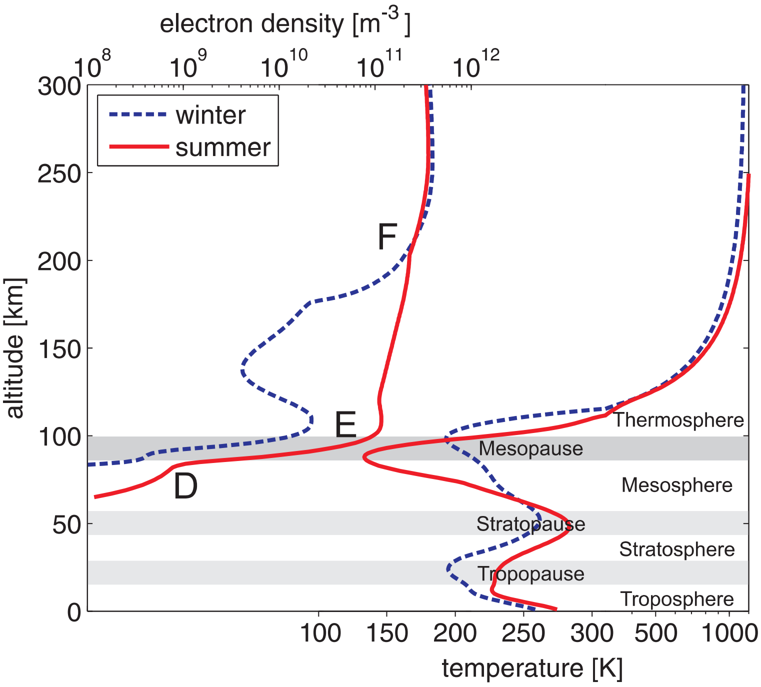

Figure 1.1: Profiles of temperature (lower abscissa) and electron densities (upper abscissa) derived from IRI-2001 model [*Bilitza*, 2001] for high latitude (69°N). The solid lines show the results in summer whereas the dashed lines in winter. The different layers of the atmosphere and the ionospheric regions (D, E, and F) are indicated in the insert.

One of the pronounced properties of atmosphere is its layered structure characterized by variation in temperature. According to the variation of temperature against altitude, the atmosphere is conventionally divided into four layers as troposphere, stratosphere, mesosphere, and thermosphere. A typical example at high latitudes is shown in Figure 1.1 (lower abscissa). The upper boundary of each layer is termed as 'pause' which is characterized by the maximum in the temperature variation.

The troposphere, also called the lower atmosphere, starts from the ground up to ∼8 km at the poles and to ∼15 km at the equator and is bounded above by the tropopause. The troposphere is mostly heated from below by transport of energy from the earth surface and hence the temperature reveals a decrease with altitude. The layers above the tropopause up to ∼90 km are the stratosphere and mesosphere which are referred to as the middle atmosphere and separated by the stratopause at ∼50 km. The temperature in the stratosphere increases with altitude due to absorption of solar ultraviolet radiation by ozone (O_3). The temperature in the mesosphere, however, decreases with altitude due to decreasing absorption of solar radiation and increasing cooling by CO_2 radiative emission. Temperature profiles shown in Figure 1.1 reveal a pronounced seasonal variation with a temperature anomaly near mesopause. I.e., there is an extreme thermal structure with mean minimum temperatures of ∼130 K above the summer pole [e.g., *Lübken*, 1999] which are below the frost point and freeze water vopar into ice clouds. The thermosphere extending from the mesopause (near ∼90 km) up to ∼1000 km along with the mesosphere is called the upper atmosphere that consequently extends from ∼50 km to 1000 km. The temperature in the thermosphere starts to dramatically increase with altitude. The energy balance of the thermosphere is primarily controlled by external sources: heating from absorption of solar radiation and auroral particle precipitation, collisions between thermal electrons, ions, and neutrals, heating from exothermic ion-neutral chemistry and neutral-neutral chemistry, energy conversion and transport processes including Joule heating, heating from atomic oxygen recombinations, and heating from O_2 absorption in the Schumann-Runge continuum and bands. In addition, the atmosphere can also be divided into homosphere and heterosphere according to the fact whether the atmospheric constituents are well mixed by turbulence. The boundary between them is called turbopause which lies near the mesopause.

The ionosphere extending from ∼60 km to more than 1000 km is a natural laboratory of plasma. The ionosphere is of practical importance since it is the source of plasma for the magnetosphere and serves as medium for shortwave broadcasting and long-range communication. According to the electron number density, the ionosphere can be divided into regions D, E, and F (also well known as subdivision of F_1 and F_2 region) shown in Figure 1.1 (upper abscissa). From Figure 1.1, the electron density increases from $\sim 10^8$ electrons/m^3 at 60 km to $\sim 10^{11}$ electrons/m^3 at 100 km and reveals a strong seasonal variation, i.e., larger electron density in the summer than in the winter. However, the peak electron density of the F_2 region at middle latitudes is larger in winter than in summer [*Appleton*, 1937; *Appleton and Piggott*, 1954]. Furthermore, D and F_1 region will disappear during night whereas D region at high latitudes can retain due to the ionisation by particle precipitation [e.g., *Friedrich and Kirkwood*, 2000]. Ionospheric D-region at high latitudes is very important for our current study since it covers the altitudes of the mesopause region where the ice particles exist and hence become charged due to electron attachment which plays a crucial role on the creation of polar mesosphere summer echoes (PMSE) [e.g., *Rapp and Lübken*, 2004].

1.2 Mesosphere and lower thermosphere region

The mesosphere and lower thermosphere (MLT) region, extending from ∼50 to 120 km and covering ionospheric D-region and lower E-region, contains the coldest part of the terrestrial atmosphere (i.e., the polar summer mesopause) where a number of fascinating geophysical phenomena, e.g., polar mesosphere summer echoes (PMSE) and noctilucent clouds (NLC), have been observed. The MLT region has long been of considerable scientific interest since the last several decades and even today under increasing concern due to its unique properties. On the one hand, scientists have suggested that the mesosphere is a more sensitive indicator of the global climate change than the troposphere, which has been suspected to be attributed to anthropogenic activities [e.g., *Thomas*, 1996]. On the other hand, the MLT region is a transition region influenced by the dynamical processes from above and below and contains a variety of physical processes, namely, that gravity waves propagating from below break and produce turbulence [e.g., *Lindzen*, 1981]; solar radiation and high-energy particle precipitation cause the variation of ionization and affects the composition [e.g., *Friedrich and Kirkwood*, 2000]; meteors from outer space ablate and produce condensation nuclei for mesospheric ice formation [e.g., *Rapp and Thomas*, 2006]. These processes are of considerable importance for this study since they are a prerequisite for the creation of PMSE which will be shown in detail later.

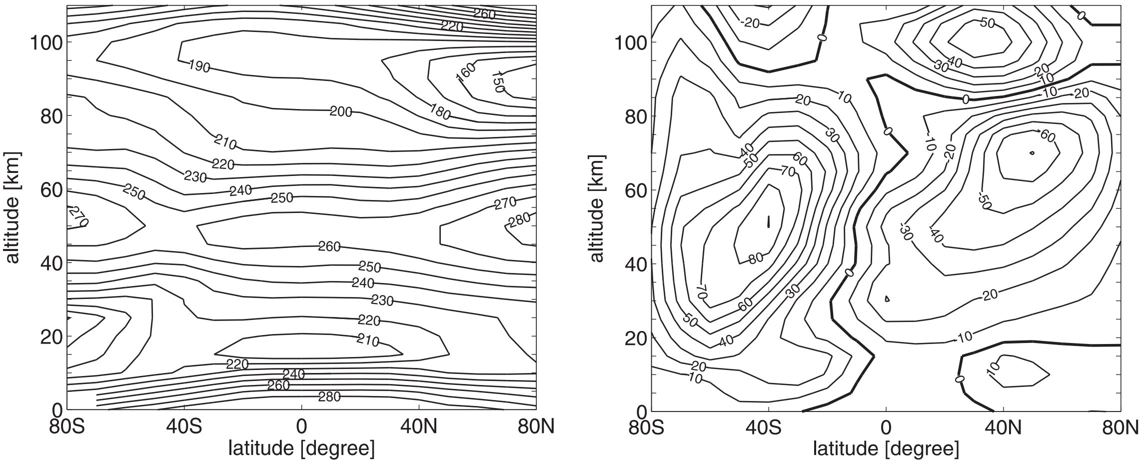

Figure 1.2: Latitudinal variations of atmospheric temperatures and zonal winds derived from the CIRA-86 [*Fleming et al.*, 1988] for middle July: (left) mean temperature in K; (right) mean zonal wind in m/s, positive numbers indicating eastward wind.

The mesopause region around 88 km is characterized by the lowest temperatures of the terrestrial atmosphere reaching ∼130 K above the summer pole which is about 60 K colder than above the winter pole. This thermal structure is contrary to the expectation from standard radiative equilibrium theory since the atmosphere at polar latitudes is continually sunlit in mid-summer whereas totally in dark in mid-winter. The cause of the mesopause inversion was suggested as adiabatic cooling and/or warming associated with vertical movements induced by dynamical processes such as gravity waves [e.g., *Garcia*, 1989]. A global circulation assumed to be forced by gravity waves results in the process that air masses well up and expand adiabatically above the summer pole leading to a temperature drop, flow towards the winter pole somewhere above the mesopause, and then sink adiabatically into the lower altitudes above the winter pole leading to a temperature rise [e.g., *Becker and Schmitz*, 2003]. Gravity waves that are thought to be excited, for example, by tropospheric winds flowing over steep orography propagate from below with increasing amplitude until they become unstable and break just below the mesopause [e.g., *Reid et al.*, 1988; *Fritts and Alexander*, 2003]. As a consequence, this process deposits energy and momentum in the region of wave breaking and induces a drag force on the flow of the mesosphere. I.e., this drag force reverses the natural eastward flow of the zonal wind induced by the thermal wind balance [*Thomas*, 1991]. Figure 1.2 shows latitudinal variations of mean temperatures and zonal winds deduced from the model results of CIRA-86 (the COSPAR International Reference Atmosphere), an empirical model which is also based on a collection of many observations and provides monthly mean values of atmospheric temperature and zonal wind with global coverage [*Fleming et al.*, 1988]. In line with the physical process of energy and momentum deposition at the mesopause described above, comparison between the two panels of Figure 1.2 reveals that the polar summer mesopause with the lowest temperatures is also the place where the zonal wind changes its directions, i.e., from eastward flow to westward flow above the polar summer mesopause.

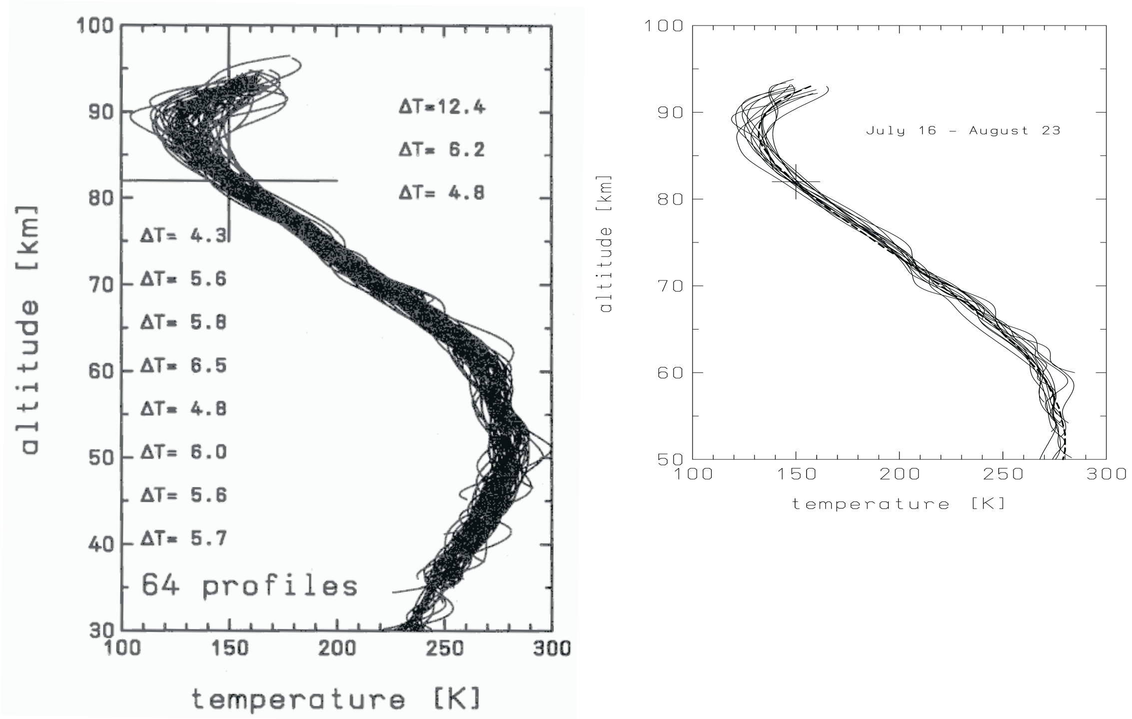

Figure 1.3: Altitude profiles of falling sphere (FS) temperatures: (left) A total of 64 FS temperature profiles observed at Andøya (69°N, 16°E) between mid-May and mid-August in various years (1987, 1991, 1992, 1993, 1995, 1997) with the standard deviation ΔT indicated at the corresponding altitudes [from *Lübken*, 1999]; (right) A total of 17 FS temperature profiles observed at Spitsbergen (78°N, 16°E) from 16 July to 23 August 2001 [from *Lübken and Müllemann*, 2003b]. The temperature of 150 K at 82 km is marked by a cross for comparison.

The above description of the thermal structure in the MLT region provides a global sense. We now turn to an in situ measurements with sounding rockets in the Arctic regions where our observations were obtained. In order to derive the seasonal variation of temperatures in the polar middle atmosphere, a total of 89 falling sphere flights at Andøya (69°N, 16°E) as well as later a total of 24 falling sphere flights at Spitsbergen (78°N, 16°E) were carried out [*Lübken*, 1999; *Lübken and Müllemann*, 2003b]. The individual temperature profiles observed in the core summer months are shown in Figure 1.3. Comparisons between each other show very small variations in temperatures. When comparing the temperatures at the mesopause, one should recognize the ∼10° difference between Andøya and Spitsbergen since the transition from summer to winter at 78°N occurs after approximately the end of August which is significant later compared to at 69°N. After a detailed comparison, *Lübken and Müllemann* [2003a] summarized that in the summer season the mesopause at 78°N is somewhat higher (by ∼1 km) and at the end of the summer season somewhat colder (by ∼5–6 K) compared to 69°N. These findings are consistent with the model calculations by *von Zahn and Berger* [2003] with COMMA/IAP (the Cologne Model of the Middle Atmosphere/Version of Leibniz Institute of Atmospheric Physics [*Berger and von Zahn*, 1999]). The calculation of the temperature using COMMA/IAP is shown in Figure 1.4 (see caption for details). The mesopause altitudes show an increase with increasing latitudes (i.e., tending to increase from the mid latitudes to the polar latitudes) whereas the mesopause temperatures drop with increasing latitudes.

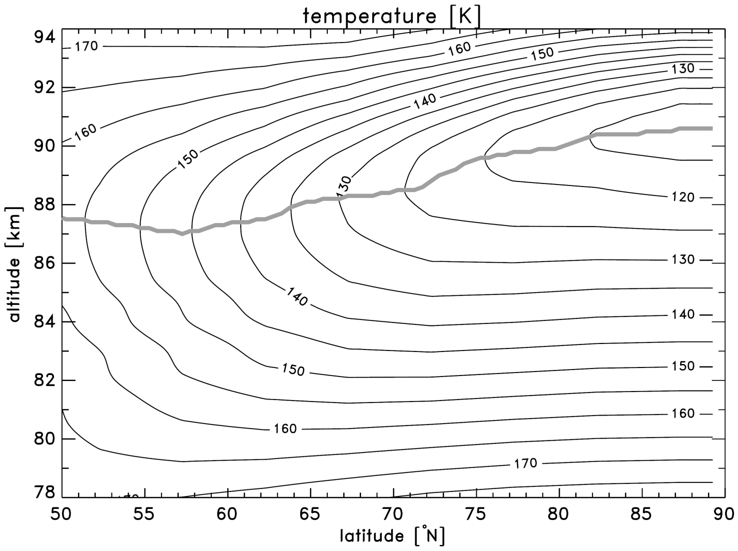

Figure 1.4: Calculated zonal mean temperature versus latitude and altitude for the mesopause region at mid and polar latitudes on 21 June using COMMA/IAP [*von Zahn and Berger*, 2003]. The mesopause indicated as grey line increases from ∼87 km at 55°N to 90 km at 80°N whereas the temperatures decrease from 150 K to as low as 110 K.

1.3 Overview of PMSE

In the late 1970s, VHF radars operating at frequencies of about 50 MHz observed extremely strong radar echoes from around the summer mesopause regions at polar as well as, to a lesser extent, at mid latitudes [*Ecklund and Balsley*, 1981; *Czechowsky et al.*, 1979]. These are later termed polar mesosphere summer echoes or PMSE [*Röttger et al.*, 1988; *Hoppe et al.*, 1988]. Since the first detection, PMSE have been intensely investigated during the last three decades since they are not only a fascinating geophysical phenomenon intriguing numerous experimental and theoretical developments but also a suitable tool for monitoring physical processes and their variability in the middle atmosphere [see *Rapp and Lübken*, 2004, for a review].

As of today, observations of PMSE have been conducted with radars operating at different frequencies ranging from 2.78 MHz to 1.29 GHz. When surveying the literature, however, it appears that most systematic studies of PMSE conducted to date were made with radars at the 'standard' frequency of ∼50 MHz [e.g., *Ecklund and Balsley*, 1981; *Hoffmann et al.*, 1999;

Huaman et al., 2001; *Bremer et al.*, 2003; *Morris et al.*, 2004, 2007; *Kirkwood et al.*, 2007a; *Zecha and Röttger*, 2009] whereas systematic studies of PMSE at other frequencies are rather scarce and mainly restricted to a few case studies [see *Rapp and Lübken*, 2004, for an overview of PMSE observations at different frequencies]. A large number of observations confirmed that PMSE exclusively occur during summer and exist in the mesopause region, more precisely, within the altitude range between ∼80 and ∼92 km. The occurrence in distinct layers is one of the striking properties of PMSE which frequently occur in double or even multiple layers. The available experimental record impressively demonstrates that the absolute scattering cross section of PMSE (more typically expressed as the radar volume reflectivity which is the scattering cross section per unit volume) reveals an enormous frequency dependence such that simultaneous and common-volume observations at more than one frequency should also be an ideal tool for studying the validity of theoretical expectations. Furthermore, PMSE are closely correlated with other phenomena in the mesosphere such as noctilucent clouds (NLC), gravity waves and tidal waves, and electron densities.

It is common belief that charged ice particles in the nanometer size range play a crucial role in the creation of PMSE. These ice particles form in the polar summer mesopause environment that is characterized by an extreme thermal structure. Mean minimum temperatures of about 130 K are attained at ∼88 km resulting in substantial supersaturation with respect to ice [*Lübken*, 1999]. This close relation of PMSE to ice particles is considerably proved by a multitude of independent observations: i.e., temperature measurements within PMSE consistently show that the echoes occur in just the altitude range where the air is indeed supersaturated [*Lübken et al.*, 2002, 2004]. Furthermore, simultaneous and common-volume observations of PMSE with radars and noctilucent clouds with optical instruments have shown that NLC typically occur at the lower edge of a PMSE layer [e.g., *Nussbaumer et al.*, 1996; *von Zahn and Bremer*, 1999; *Lübken et al.*, 2004; *Klekociuk et al.*, 2008; *Hervig et al.*, 2011]. Note that NLC have long been known to be direct evidence for ice particles at mesopause levels which can even be observed with the naked eye under favorable conditions [see *Thomas*, 1991, for a comprehensive review]. These common volume observations indicate that PMSE are indicative of the total population of ice particles whereas the visible NLC require that the particles have grown to sizes in excess of ∼20 nm [see *Rapp and Lübken*, 2004; *Rapp and Thomas*, 2006, for more details regarding ice microphysics and PMSE and NLC]. Finally, in situ observations of (charged) ice particles in PMSE-layers have unequivocally demonstrated that the presence of these particles is the primary prerequisite for the existence of PMSE [e.g., *Havnes et al.*, 1996, 2001; *Mitchell et al.*, 2001; *Croskey et al.*, 2001; *Blix et al.*, 2003; *Smiley et al.*, 2003].

Due to the extremely large signal strength, assumptions attributing PMSE to incoherent scatter from the plasma of the ionospheric D-region as well as to the conventional turbulent backscatter from ionisation irregularities in the mesosphere are easily ruled out. In the frame of the Bragg condition, efficient radio backscatter only occurs when irregularities in the refractive index (mainly given by the electron number density in the mesosphere) possess a scale equal to half the radar wavelength, i.e., the Bragg wavelength for monostatic radars. There is now strong evidence that the creation of these irregularities in the electron densities results from turbulent transport of charged ice particles. At PMSE-altitudes (∼80–90 km), the Bragg wavelengths of typically used VHF radars is in the range of some meters (e.g., 3 m for radars operating at 50 MHz) which falls into the viscous subrange of neutral turbulence where any irregularities of electron density should be rapidly destroyed by molecular diffusion. It was proposed by *Kelley et al.* [1987] and *Cho et al.* [1992], however, that the existence of large cluster ions and charged ice particles should result in the reduction of electron diffusivity due to ambipolar forces. The destruction of small scale irregularities should hence be reduced such that Bragg-scale irregularities may still exist and lead to strong backscatter observed as PMSE. This process can be described by means of an enhanced Schmidt-number, i.e., $Sc = \nu/D_e > 1$, where ν is the kinematic viscosity of air, and D_e is the electron diffusion coefficient, which in turn quadratically depends on the particle radius . From the studies of *Batchelor* [1959], the power spectrum of the tracers extends to much smaller scales than the spectrum of turbulence itself and hence reveals a so-called viscous convective subrange characterized by a k^{-1}-dependence (in the one-dimension case) in the presence of charged ice particles. Importantly, in situ measurements of neutral and plasma density fluctuations have since proven the occurrence of larger Schmidt numbers of up to 4000 [*Lübken et al.*, 1994, 1998; *Strelnikov et al.*, 2009].

The above described theory regarding the creation of PMSE can be summarized that the echoes originate from turbulence-induced scatter in combination with a large Schmidt number caused by the presence of charged ice particles. This has since been further extended by several authors [*Rapp and Lübken*, 2003, 2004; *Lie-Svendsen et al.*, 2003; *Rapp et al.*, 2008; *Nicolls et al.*, 2009; *Strelnikova and Rapp*, 2011; *Varney et al.*, 2011] and will be referred to as the 'turbulence with large Schmidt-number'-theory (termed as the TWLS-theory in short) in the remainder of this thesis. Note further that alternative theories invoking plasma instabilities due to large electric fields [e.g., *D'Angelo*, 2005] or metal coatings on the ice particles [*Bellan*, 2008] have been seriously questioned based on independent observations and theoretical arguments [*Shimogawa and Holzworth*, 2009; *Rapp and Lübken*, 2009]. In addition, earlier theoretical attempts and/or objections against this turbulence-based theory e.g., dust hole scatter [*Havnes et al.*, 1990], opalescence [*Trakhtengerts*, 1994; *Trakhtengerts and Demekhov*, 1995], charged dust diffusive waves [*Hocking and Röttger*, 1983], vertical convergence [*Reid*, 1997], plasma instability [*Blix*, 1999] have previously been ruled out based on available experimental facts and/or theoretical arguments as discussed in detail in *Cho and Röttger* [1997], *Rapp and Lübken* [2004], and *Rapp et al.* [2008].

1.4 Objectives and structure of this thesis

This thesis is dedicated to the experimental investigation of PMSE with the EISCAT radars and SOUSY radar in the frame of the CAWSES (Climate And Weather of the Sun-Earth System) priority program. The major subject is to further fill the gap of systematic PMSE studies at higher frequencies than 50 MHz, i.e., 224, 500, and 930 MHz and to study the dependence of PMSE on different radar frequencies (hence different Bragg wavelengths) based on simultaneous and common-volume observations. In addition, we test the standard theory of PMSE (i.e., the TWLS-theory) [*Rapp and Lübken*, 2004; *Rapp et al.*, 2008] using calibrated signals and apply this theory to observations to derive the microphyisical parameters of the involved ice particles.

The main objectives of this thesis are to achieve

- Statistical properties of PMSE at frequencies of 224, 500, and 930 MHz including volume reflectivities, occurrence rates and their frequency dependence.
- Factors leading to the occurrence of PMSE in the UHF range (i.e., at very small spatial scales).
- Test of the TWLS-theory of PMSE with simultaneous and common-volume observations at two well-separated frequencies and application of the theory to derive microphysical parameters of the involved ice clouds.

- Statistics of electron density depletion at PMSE layers.

This thesis is organized as follows: Chapter 2 and 3 review our current knowledge of PMSE regarding experiment and theory, respectively. Chapter 4 gives a short description of the experimental details and data sets. The main results are then presented in the subsequent chapters (Chapters 5–8). In Chapter 5 we analyze the PMSE observations with respect to occurrence rates and probability distributions of volume reflectivities and compare them at different frequencies (Sections 5.2 and 5.3). In addition, the rather large data base of PMSE observations with the EISCAT VHF radar at 224 MHz is used to study the temporal variability of PMSE, i.e., year-to-year, seasonal as well as diurnal variations (Section 5.4). In Chapter 6 the factors involved in the occurrence of PMSE in the UHF range (here at 500 and 930 MHz) are considered by comparing electron densities and spectral widths (indicative of turbulence) in the presence and absence of UHF-PMSE. In Chapter 7 we first test the TWLS-theory of PMSE with a large number of simultaneous and common-volume observations (Section 7.1). We then apply this theory to the observations to derive microphysical parameters of the involved ice clouds (Section 7.2). The derived results are further compared to independent measurements with the Solar Occultation For Ice Experiment (SOFIE) onboard the Aeronomy of Ice in the Mesosphere (AIM) spacecraft as well as with the ALOMAR RMR lidar (Section 7.3). In Chapter 8 the statistics of electron density depletions in PMSE layers are derived from radar observations. Finally, Chapter 9 concludes this study with a presentation of the main results of this thesis as well as suggestions for future work.

Chapter 2

Observational results regarding PMSE

2.1 History

In the end of 1970s, the Poker Flat MST (Mesosphere-Stratosphere-Troposphere) radar at a frequency of 50 MHz observed very strong echoes at the altitudes between ~78 and 95 km with a maximum reaching an average of 30 dB at ~86 km in summer [*Ecklund and Balsley*, 1981]. These radar echoes were later termed polar mesosphere summer echoes or PMSE [*Röttger et al.*, 1988; *Hoppe et al.*, 1988]. Since the initial observation, PMSE have subsequently been studied in details with radars operating at a variety of frequencies between 2.78 MHz and 1.29 GHz [*Rapp and Lübken*, 2004] whereas most systematic studies of PMSE were carried out with radars at the 'standard' frequency of ~50 MHz. After three decades of measurements there are a number of long-term observational data sets around the world available for the studies of PMSE (Table A.1 lists the MST radars dedicated to study PMSE as well as incoherent scatter (IS) radars used to study PMSE). The CEDAR (Coupling, Energetics, and Dynamics of Atmospheric Regions) data base contains the 7-year original data set conducted with the Poker Flat MST radar which goes back to as far as 1979 [*Ecklund and Balsley*, 1981]. The ALOMAR (Arctic Lidar Observatory for Middle Atmosphere Research) SOUSY radar installed in July 1994 along with its successor the ALWIN (ALOMAR Wind) radar has been run for more than 10 years and achieved a rich source of continuous observations of PMSE. Long-term observations with other MST radars e.g., ESRAD (Esrange MST radar), OSWIN (Ostsee wind radar), SSR (SOUSY Svalbard radar) et al., are now also available for the systematic studies of PMSE. Furthermore, PMSE observations with the EISCAT radars have been performed using appropriate programs, e.g., 'arcdlayer'-experiment, and achieved sufficient data set based on very intensive PMSE campaigns at Tromsø. In this chapter, we will present the statistical properties of PMSE and their connections with turbulence, noctilucent clouds (NLC) and other phenomena in the ambient environments based on the observational results.

2.2 Morphology

Figure 2.1 shows a typical example of PMSE observations conducted with the SOUSY Svalbard radar on 20 July 2001. During this 24-hour period, very strong echoes were observed in approximately the same altitude range between ~80 and 92 km with the signal-to-noise ratio (SNR) up to 30 dB. These echoes reveal some pronounced variations in their morphology,

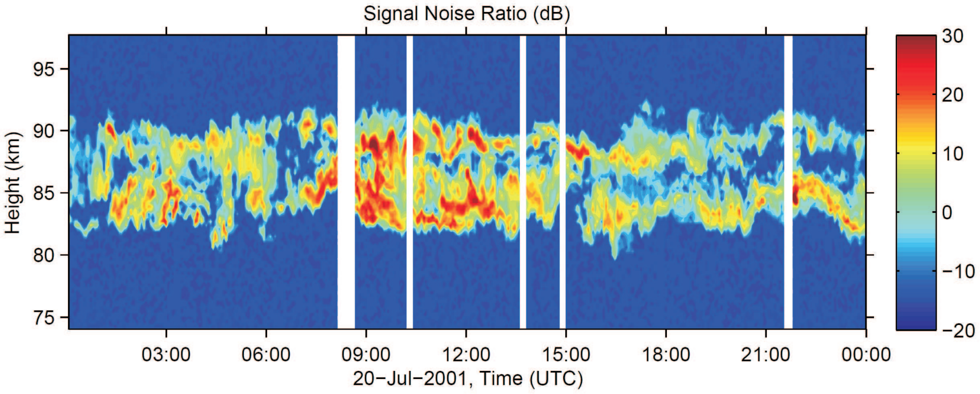

Figure 2.1: Height-time-intensity plot of PMSE observed with the SOUSY Svalbard radar at 53.5 MHz during an entire day. The color scales indicate the signal-to-noise ratio (SNR) whereas white gaps mark short interruptions resulting from transmitter inhabits due to local air traffic security. This figure is reproduced from *Zecha and Röttger* [2009].

such as wave-like variations. In addition, PMSE appear in one continuous layer as well as, more frequently, in two or more vertically separated layers.

As already evident from the first detection of PMSE by *Ecklund and Balsley* [1981], these echoes are much stronger in summer than in other seasons and hence reveal a pronounced seasonal variation [*Balsley et al.*, 1983; *Bremer et al.*, 2003]. PMSE exist near mesopause region, more precisely, within the altitude range between ∼80 and 92 km. Recently, *Lübken et al.* [2009b] presented that PMSE were seldom detected above ∼92 km. This has been attributed to the effect of large values of molecular viscosity which effectively destroys any small-scale structures at these altitudes. After surveying the literature, we thereby give a short summary of the most pronounced properties of PMSE as follows:

- The occurrence in distinct layers is one of the striking properties of PMSE and the layers of PMSE reveal double or multiple structures separated by a few kilometers (see Figure 2.1) [e.g., *Zecha and Röttger*, 2009].

- Generally, PMSE occur in layers as thin as the best radar range resolution of 150 m and up to a few kilometers in thickness [*Franke et al.*, 1992].

- PMSE layers are frequently lifted up and down in height up to a few kilometers with a vertical velocity up to 8–10 m/s [*Röttger and LaHoz*, 1990]. *Röttger and LaHoz* [1990] also found abrupt jumps in the Doppler spectra.

- The backscatter cross section of PMSE can change by 2 orders of magnitude within a few minutes [*Bremer et al.*, 1996b].

- The wave-like structure of PMSE can most likely be attributed to the modulation of gravity waves as well as tidal waves [*Hoffmann et al.*, 2005, 2008].

- PMSE observations reveal aspect sensitivity. There are large aspect sensitivities in the lower part of the PMSE layer and small aspect sensitivities in the upper part of the PMSE layer [e.g., *Czechowsky et al.*, 1988].

- Very strong radar echoes are observed not only at polar latitudes but also at middle latitudes and hence reveal a pronounced latitudinal dependence as well as longitudinal dependence [*Rapp and Lübken*, 2004; *Latteck et al.*, 2008]. Furthermore, debates have long been existing on the interhemisphere difference of PMSE [*Latteck et al.*, 2007; *Morris et al.*, 2009].

2.3 Climatology

As the name says, PMSE occur exclusively in summer and hence reveal a pronounced seasonal variation, which has long been derived from the first detection [*Ecklund and Balsley*, 1981]. This is very similar with the case of NLC, a direct evidence of existing ice particles due to the extremely low temperatures of the mesopause region in the period between the end of May and mid August. Intrigued by this similarity, several authors have tried to relate the occurrence of PMSE to the occurrence of ice particles and found that PMSE occur where the degree of water ice saturation S is larger than 1 [*Lübken*, 1999; *Lübken et al.*, 2004]. Here S is the ratio between the actual water vapor partial pressure and the saturation vapor pressure over ice. Figure 2.2 shows the typical seasonal variation of the occurrence rate of PMSE observed with the 53.5 MHz ALWIN radar at Andenes (69°N, 16°E) during the years 1999, 2000, and 2001 [*Bremer et al.*, 2003]. The main characteristics show a steep increase in occurrence during end of May/beginning of June, a rather high level near 90% in the middle of June until the middle/end of July, and a moderate decrease during August. The observations shown in Figure 2.2 are in general agreement with independent observations with radars at ∼50 MHz from different geophysical latitudes [*Zecha et al.*, 2003; *Bremer et al.*, 2006; *Zecha and Röttger*, 2009] and different longitudes [*Balsley and Huaman*, 1997; *Kirkwood et al.*, 1998] as well as with radar at 224 MHz [*Palmer et al.*, 1996].

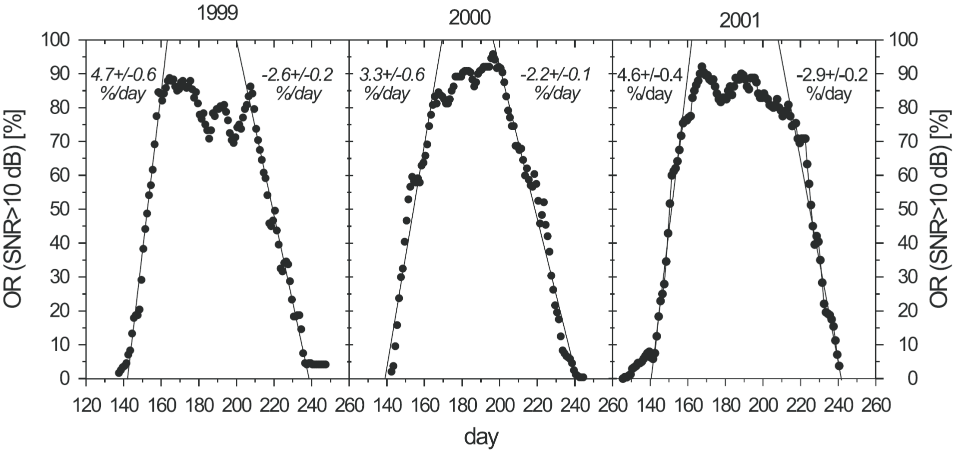

Figure 2.2: Seasonal variation of the occurrence rate of PMSE with SNR larger than 10 dB from observations with the ALWIN radar at Andenes during the years 1999, 2000, and 2001. The straight lines indicate the gradients at the beginning and end of the PMSE seasons. This figure is reproduced from *Bremer et al.* [2003].

In addition, statistical observations reveal that PMSE are characterized with other temporal variations than seasonal variation, e.g., year-to-year (long-term) variation and semidiurnal variation. The long-term variation of the PMSE occurrence was firstly derived by *Bremer et al.* [2003] who analyzed the observations conducted with the ALOMAR SOUSY radar during the years 1994–1997 and with the ALWIN radar during the years 1999–2001. Recently, *Bremer et al.* [2009] extended the data set from 1994 to 2008 and reconsidered the long-term variation of the PMSE occurrence at polar latitudes as well as at mid latitudes with the OSWIN radar at Kühlungsborn (54°N, 12°E). The authors compared the occurrence rates of PMSE at 53.5 MHz with the solar Ly-α radiation and geomagnetic Ap index and found a positive correlation for both cases (see Figure 2.3), which indicates that the long-term variations of PMSE mainly depend on the variations in the background ionization. Please note that the dominant ionization sources at the PMSE altitudes are from the ionization of NO due to Ly-α and high-energy particle precipitation indicated by Ap index.

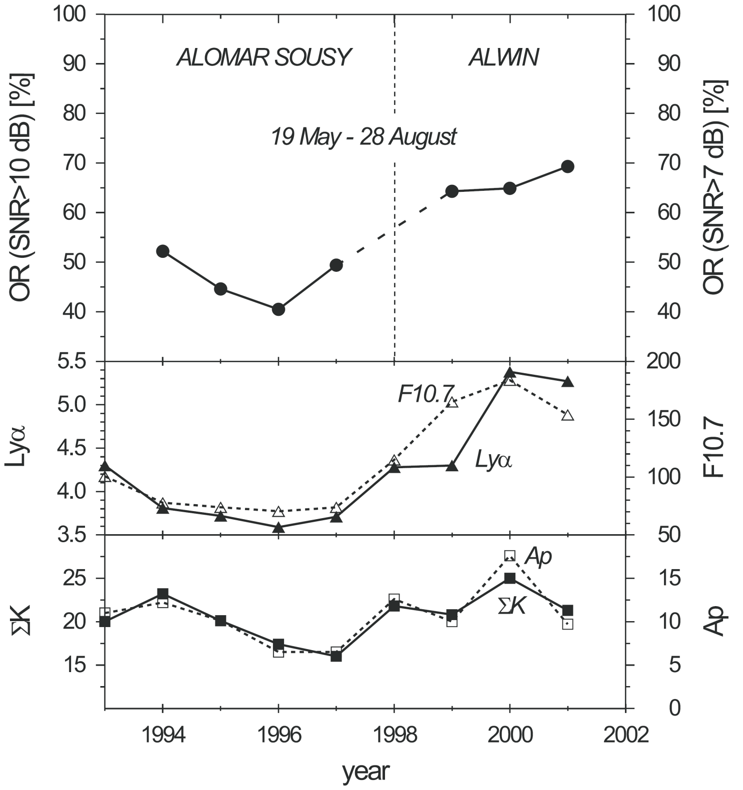

Figure 2.3: Comparison of year-to-year variations between the occurrence rates of PMSE at 53.5 MHz (upper panel) and corresponding variations of the solar radiation (Ly-α and 10.7 cm radio flux in the middle panel) and geomagnetic activity (global Ap index and local ΣK index in the lower panel). This figure is reproduced from *Bremer et al.* [2003].

As for shorter time scales, diurnal and/or semidiurnal variations are one of the prominent characteristics of PMSE. I.e., diurnal variations are dominated by a maximum around local noon and a minimum around 19:00–20:00 LT which is in phase with similar semidiurnal variations in NLC properties. It is suggested that the diurnal pattern is caused by a superposition of temperature variations due to the semidiurnal tide [*Hoffmann et al.*, 1999] as well as the diurnal variation of ionization caused by both solar Ly-α radiation as well as particle precipitation [*Klostermeyer*, 1999]. PMSE also show some variations with a period of about 5 days. These variations have been shown in the observations of temperature, zonal wind and NLC (or polar mesosphere clouds, the layer of ice particles observed from above with optical instruments onboard satellite) which are correlated with the passage of 5-day planetary waves [*Kirkwood and Stebel*, 2003; *von Savigny et al.*, 2007; *Merkel et al.*, 2008]. These waves could also modulate PMSE resulting in strong 5-day variations in occurrence [*Zecha and Röttger*, 2009]. Furthermore, other short-term variations of PMSE have been identified to be correlated with solar and geomagnetic activities as well as dynamical phenomena, e.g., gravity waves [*Bremer et al.*, 2001; *Hoppe and Fritts*, 1994, 1995].

2.4 Frequency dependence

In the frame of classical turbulence, any structures smaller than the inner scale (the transition region between the inertial subrange and the viscous subrange, which is tens of meters in the mesosphere) should be rapidly destroyed by molecular diffusion. The detection of strong echoes with radars at ∼50 MHz (3-m Bragg scale) did surprise the researchers and intrigued them to investigate PMSE in more frequency ranges. So far, PMSE have been observed at a variety of frequencies between ∼2.78 MHz and 1.29 GHz. However, it appears that most systematic studies of PMSE were carried out at ∼50 MHz [e.g., *Ecklund and Balsley*, 1981; *Bremer et al.*, 2003; *Kirkwood et al.*, 2007b; *Latteck et al.*, 2008; *Morris et al.*, 2009; *Zecha and Röttger*, 2009] whereas systematic studies of PMSE at other frequencies are rather scarce and mainly restricted to a few case studies [see *Rapp and Lübken*, 2004, for an overview of PMSE observations at different frequencies]. Note that it is very difficult to detect PMSE with MF (medium frequency) and HF (high frequency) radars due to the low system power, the rough height resolution, and other scattering processes contributing to the overall received power-values. However, PMSE-like echoes in the MF and HF ranges have been determined by the close relation with the simultaneous VHF (very high frequency) PMSE as well as the similarity of their general features with PMSE [*Bremer et al.*, 1996a; *Karashtin et al.*, 1997; *Kelley et al.*, 2002; *Liu et al.*, 2002; *Ramos et al.*, 2009]. For the case of measurements at higher frequencies, PMSE have been reported on VHF at 224 MHz [*Hoppe et al.*, 1988; *Palmer et al.*, 1996; *Hocking and Röttger*, 1997; *Röttger and LaHoz*, 1990] as well as on UHF (ultra high frequency) at 430 MHz [*Varney et al.*, 2007; *Nicolls et al.*, 2009], 500 MHz [*Hall and Röttger*, 2001; *Röttger*, 2001], 930 MHz [*Röttger et al.*, 1990; *La Hoz et al.*, 2006; *Rapp et al.*, 2008], and 1290 MHz [*Cho and Kelley*, 1992]. However, the reason for this poor statistics of PMSE in the UHF range is indeed of geophysical origin. Especially, the PMSE occurrence at 930 MHz is extremely rare and mainly restricted to the core summer seasons and PMSE at 1290 MHz have only been reported once by *Cho and Kelley* [1992]. The available observations imply that the VHF range is the most favorable frequency band for the detection of PMSE.

According to theory and based on several data points, PMSE reveal a tremendous dependence of the observed volume reflectivities (= the backscattering cross section per unit volume) on the radar frequency. Figure 2.4 shows altitude profiles of volume reflectivities simultaneously measured with the ALWIN radar (53.5 MHz) and the EISCAT VHF and UHF radar (224 MHz and 930 MHz, respectively). The comparison between the volume reflectivities at three frequencies clearly demonstrates a strong frequency dependence of PMSE: from the minimum frequency of 53.5 MHz to the maximum frequency of 930 MHz, the volume reflectivities vary by as much as six orders of magnitude [*Rapp et al.*, 2008]. The same finding has been mentioned by *Röttger et al.* [1990] who compared the simultaneous measurements of PMSE with the CUPRI (Cornell University Portable Radar Interferometer) radar at 49 MHz and the EISCAT UHF radar at 930 MHz. Table A.2 gives an overview of PMSE studies with calibrated radars at different frequencies together with the derived absolute volume reflectivities. Please note that the listed different measurements of volume reflectivities were not performed at the same time and same location and hence at different geophysical situation. However, the available experimental record impressively demonstrates that the volume reflectivities at different frequencies clearly reveal an enormous decrease with increasing frequencies (or decreasing Bragg scales) such that simultaneous and common-volume observations at more than one frequency should be an ideal tool for studying the validity of theoretical expectations of PMSE. Along that line, *Rapp et al.* [2008] and *Belova et al.* [2007] considered case studies of PMSE observations with a radar operating at 53.5 MHz (ALWIN) and the EISCAT VHF and UHF radar at 224 MHz and 930 MHz. It is also one of the objectives of this thesis to test theory of PMSE and quantify the frequency dependence of PMSE based on such large number of observations that reliable statements on the statistical behavior of the phenomenon can be made (see Chapter 3 for details).

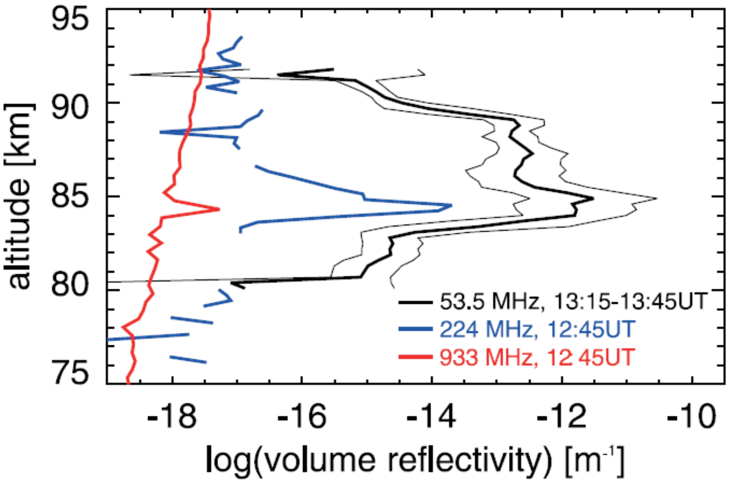

Figure 2.4: Altitude profiles of volume reflectivities observed with the ALWIN radar (black lines) and the EISCAT VHF and UHF radar (blue and red lines) on 5 July 2006. EISCAT measurements were obtained at 12:45 UT. ALWIN data are shown as mean plus/minus one standard deviation of the signal measured in the period from 13:15 to 13:45 UT. This figure is reproduced from *Rapp et al.* [2008].

2.5 Factors leading to PMSE

Observational facts show that PMSE reveal the similar properties, e.g., seasonal variations and existing altitude ranges, with another mesospheric phenomenon NLC. The latter has long been known as direct evidence of existing ice particles whereas the creation of PMSE is much more complicated and depends on other factors in addition to ice particles. According to the currently most widely accepted theory of PMSE which assumes that the echoes originate from turbulence-induced scatter aided by a large Schmidt number caused by the presence of charged ice particles (termed the TWLS-theory), PMSE are closely correlated with the turbulence strength, the electron density, and the properties of the ice particles involved.

2.5.1 Ice particles

The mesopause region in summer is the coldest part of the terrestrial atmosphere with mean minimum temperatures of ∼130 K which are already below the frost point allowing ice particles to form and grow at altitudes between ∼80 and 90 km. Measurements of the falling sphere temperatures with sounding rockets have been conducted in the PMSE layers and the comparison between the PMSE and temperatures shows that these radar echoes indeed occurred in exactly the altitude range where the degree of saturation of water vapor over ice S is larger than 1 due to the low temperatures [*Inhester et al.*, 1994; *Lübken et al.*, 2002]. The ice particles on the order of nanometers existing in the vicinity of PMSE have been confirmed from both direct and indirect evidence. Electron density depletion (or biteout) is one of the most pronounced properties of the PMSE environment that the electron density is depleted as much as, typically, one order of magnitude below the undisturbed background. The occurrence of electron density depletion is considered as evidence of the existence of ice particles which act as an efficient sink for electrons [e.g., *Ulwick et al.*, 1988]. Noctilucent clouds (NLC), occurring between 80 and 85 km, have long been known as a direct manifest of the available ice particles with the size in excess of ~20 nm [*Witt*, 1969; *Lübken*, 1999; *Hervig et al.*, 2001]. NLC are a summer-time phenomenon in both hemispheres from about 5 weeks before solstice to 7 weeks afterwards [see *Thomas*, 1991, for an overview]. Therefore, NLC reveal a similar seasonal variation as PMSE. The potential relationship between PMSE and NLC has been noticed since the initial observations of PMSE [*Ecklund and Balsley*, 1981] and further studied with common-volume observations of PMSE and NLC [*Nussbaumer et al.*, 1996; *von Zahn and Bremer*, 1999; *Lübken et al.*, 2004]. Figure 2.5 shows the first common-volume observations of PMSE with the ALOMAR SOUSY radar and NLC with the ALOMAR RMR lidar at Andenes, Norway (69°N) [*Nussbaumer et al.*, 1996]. Evidently, there is a close relationship between the two phenomena with the NLC layer located at the lower edge of the PMSE layer. The finding was later confirmed as a common scenario (63% of all observations) by *von Zahn and Bremer* [1999] based on more sufficient statistics. In addition, this close coupling between PMSE and NLC was also obtained in Spitsbergen (78°N) [*Lübken et al.*, 2004].

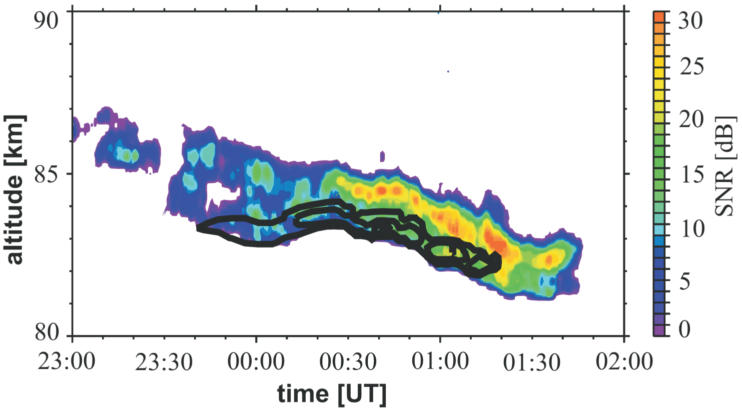

Figure 2.5: Common-volume observations of PMSE and NLC on 30–31 July 1994 at Andenes. PMSE detected with the ALOMAR SOUSY radar are shown as a function of altitude and time (in dB, see color bar) whereas NLC detected with the ALOMAR RMR lidar locate exactly at the lower edge of the radar echoes (see black contour lines). This figure is reproduced from *Nussbaumer et al.* [1996].

The first direct in situ measurements of (charged) ice particles in the PMSE environment have been carried out with a Faraday-cup-like instrument (known as the 'DUSTY'-detector) which is used to measure the charge number density associated with the particles [*Havnes et al.*, 1996]. The close coupling between the radar backscatter profile and the charge density of ice particles as a function of altitude has been obtained with the first common-volume observations of PMSE with the ALWIN radar and of charge density of ice particles with the rocket (MD-06, see Figure 2.6) [see *Havnes et al.*, 2001, for the details]. The existence of charged ice particles has been further confirmed by several independent observations [*Mitchell et al.*, 2001, 2003; *Smiley et al.*, 2003]. Recently, *Megner et al.* [2009] reported the presence of large ice particles with rocket photometers during the ECOMA/MASS campaign at Andøya in 2007 and independent observations on the same sounding rocket allowed determination of corresponding particle radii in the range of 20–30 nm [*Rapp et al.*, 2009].

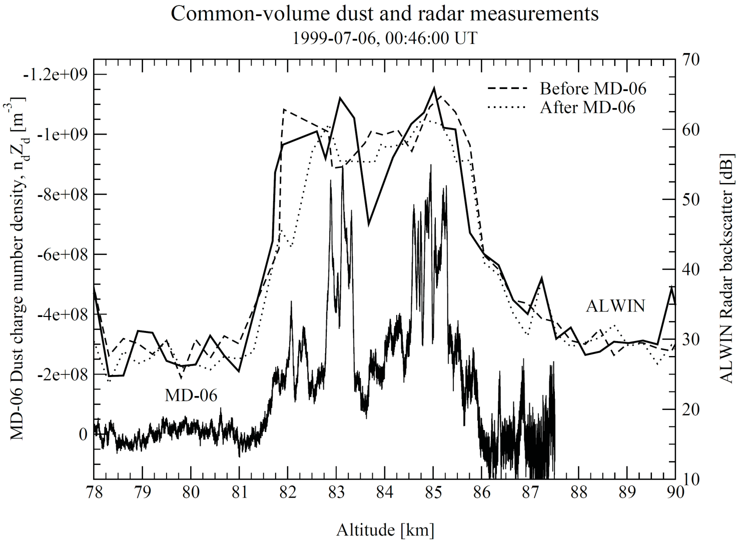

Figure 2.6: Altitude profiles of the radar SNR measured with the ALWIN radar for the time closest to the payload passage (full line) and ∼1–2 min before and after (dashed line and dotted line, respectively). Altitude profiles of charged ice particles given by the value of $|Z_A|N_A$ are shown for comparison. This figure is reproduced from *Havnes et al.* [2001].

2.5.2 Electron number density

It is well known that PMSE are the radio backscatter originating from irregularities in the refractive index which is mainly controlled by the electron number density in the mesosphere. Hence, sufficient electron number density is one of the prerequisites for the occurrence of PMSE. In addition, the occurrence of PMSE is closely correlated with the ratio between the charge number density of ice particles $|Z_A|N_A$ and the free electron density n_e, i.e., $|Z_A|N_A/n_e$. The increase of n_e (hence the decrease of $|Z_A|N_A/n_e$) results in the increase of electron diffusivity. The irregularities in electron density, due to ambipolar forces between electron density and charged ice particles, should be destroyed and PMSE should vanish. Therefore, PMSE layers reveal a complex dependence on electron densities. There are several independent indications that a lower electron density exists below which PMSE cannot occur [*von Zahn and Bremer*, 1999; *Latteck et al.*, 1999b; *Goldberg et al.*, 2001]. *Rapp et al.* [2002] quantified the lower limit of the electron density for PMSE occurrence as ∼300–500 electrons/cm^3, which can be understood in terms of the standard theory of the scattering of VHF waves in the D region. On the other hand, there might be also a limit of electron density above which PMSE cannot occur [e.g., *Rapp et al.*, 2002]. However, this is far more complicated to be conclusive.

The free electrons existing near mesopause regions play an important role on the occurrence of PMSE. A direct proof comes from the active modulation of PMSE using HF-heating. During the artificially induced modulation of PMSE, these radar echoes immediately disappeared when the heater was switched on and immediately reappeared when the heater was switched off [e.g., *Chilson et al.*, 2000]. These observations have been explained by *Rapp and Lübken* [2000, 2003] in the scope of temperature dependence of electron diffusion in the PMSE environment consisting of electrons, ions, and charged ice particles. With the heater on, heating electrons increase the electron diffusivity resulting in the destruction of irregularities in the electron density and the absence of PMSE. With the heater off, the electron temperatures immediately fall back immediately and return to the previous diffusion state thereby leading to the recovery of PMSE. Furthermore, several independent investigations show that PMSE reveal a clear dependence on the electron density enhancements which are caused by solar and geomagnetic activities [e.g., *Bremer et al.*, 2006, 2009].

2.5.3 Turbulence

It is explained in detail for example in *Hocking* [1989] that the Doppler spectral width yields information regarding the velocity variance of the detected scatterers in the radial direction which is closely dependent on the turbulent energy dissipation rate. A comparison of the spectra of incoherent signals from the ionospheric plasma and coherent scatter from PMSE layers [*Röttger and LaHoz*, 1990] demonstrates that the coherent spectra in the condition of PMSE are much narrower than those for the case of incoherent scatter signals. In addition, the spectral widths (hence the turbulent energy dissipation rates) of PMSE layers reveal an increase with increasing altitudes [e.g., *Czechowsky et al.*, 1988] which indicates that the enhanced neutral air turbulence is one of the prerequisites of PMSE at higher altitudes.

Aspect sensitivity describes the dependence of the radar echoes on the zenith angle of the tilted radar beam. If the target media is specular, backscatter (for a monostatic radar) can only be observed when the zenith angle is zero indicating large aspect sensitivity. In contrast, if the target media is isotropic (i.e., turbulent), backscatter can be observed equally at any direction indicating small aspect sensitivity. First measurements used to study aspect sensitivity of PMSE with the ALOMAR SOUSY radar at 53.5 MHz was reported by *Czechowsky et al.* [1988] who show large aspect sensitivity in the lower part of the PMSE layers and small aspect sensitivity in the upper part of the PMSE layers. This is in full agreement with the spectral width of PMSE, i.e., more turbulent (isotropic) in the upper part of the PMSE layers and more specular (anisotropic) in the lower part of the PMSE layers.

The best way to investigate the correlation between turbulence and PMSE is to perform direct measurements of turbulent energy dissipation rates in the PMSE layers. The pioneer studies have been carried out by *Lübken et al.* [1993] who performed the first direct measurement of turbulent energy dissipation rate in a PMSE layer as well as by *Lübken et al.* [2002] who summarized the first 8 sounding rocket flights. *Rapp and Lübken* [2003] extended the data set presented by *Lübken et al.* [2002] and compared the occurrence rates of PMSE observed with the ALOMAR VHF radar and neutral air turbulence from the sounding rocket flights in a climatological sense. Figure 2.7 from the study of *Rapp and Lübken* [2003] shows that turbulence indeed occurs in the entire altitude range in the presence of PMSE. In addition, the turbulence occurrence rate is larger at altitudes above ∼86 km but smaller below that altitude compared to the PMSE occurrence rate. It is well estimated that the PMSE layers comprise charged ice particles in the nanometer size range which quadratically determine the decay time of irregularities (see Chapter 3 for details). Hence, irregularities can retain for quite a while due to the presence of charged ice particles after neutral air turbulence has ceased ('fossil'-turbulence).

For the case that the turbulence occurrence rate is smaller than the PMSE occurrence rate at altitudes below ∼86 km, one should notice the fact that the radar receives backscatter from a volume of ∼7 km in diameter whereas the rocket probes a much smaller volume with a diameter of ∼5 cm at 85 km. From Figure 2.8, very strong turbulence (no turbulence)

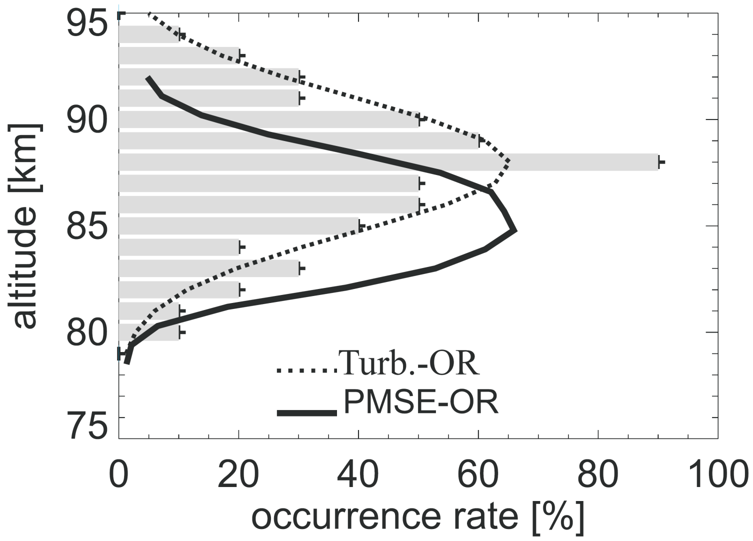

Figure 2.7: Comparison between the occurrence rates of PMSE (solid line) and neutral air turbulence (histogram and dashed line). The figure is reproduced from *Rapp and Lübken* [2003].

will be measured if the rocket flies through Point A (B) whereas the measurement of PMSE is an average value of backscatter from the entire radar volume, which results in the biased observations of lower occurrence rate of turbulence than PMSE.

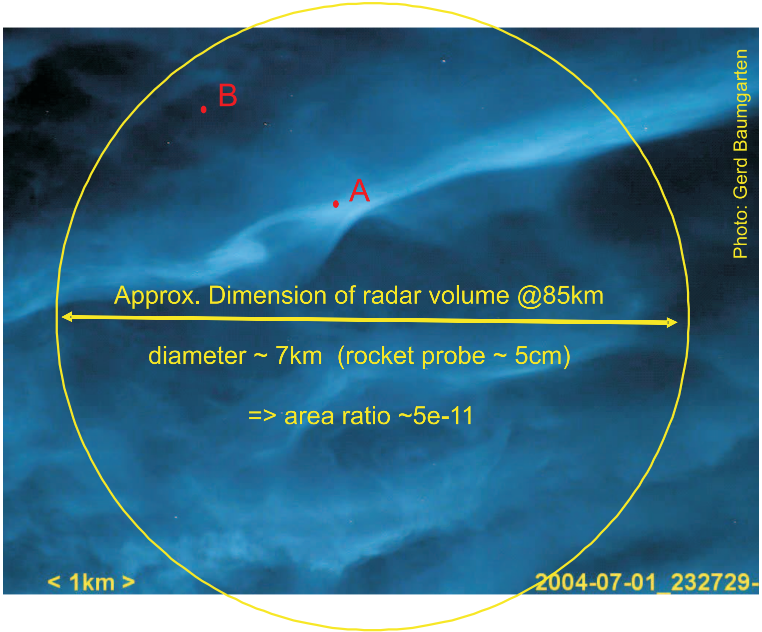

Figure 2.8: Comparison of the volume dimension between radars and sounding rockets. The area ratio is as small as ∼5e-11. Courtesy of M. Rapp.

Chapter 3

Theory

Since the initial observations of PMSE, numerous experimental and theoretical investigations in the research community were carried out to resolve the physical processes responsible for the creation of this intriguing phenomenon. There are two evident mechanisms assumed to cause radar scatter from the PMSE altitudes, i.e., (1) incoherent scatter from the plasma of ionospheric D-region due to the motion of the electrons highly coordinated by damped ion-acoustic waves and coherent scatter, (2) the scatter from the irregularities in the electron density distributions. According to the Bragg scatter condition, coherent scatter only occurs when the irregularities in the refractive index (mainly given by the electron density in the mesosphere) possess a scale corresponding to half the radar wavelength which is 3 m for a 50 MHz radar [*Tatarskii*, 1971].

The refractive index n of the atmosphere is a function of atmospheric temperature, pressure, electron density, and an appropriate humidity variable, such as partial pressure of water vapor. An empirical expression of n at radio frequencies between HF and UHF is written in the following equation:

$$n - 1 = \frac{0.373 p_{H_2O}}{T^2} + \frac{77.6 \times 10^{-6} p_a}{T} - \frac{40.3 n_e}{f_c^2} \tag{3.1}$$

where p_{H_2O} is the partial pressure of water vapor in mb, p_a is the atmospheric pressure in mb, T is the absolute temperature in K, n_e is the electron density in m^{-3} and f_c is the critical frequency and given by $f_c = 9 \times 10^{-6}\sqrt{n_e}$ in MHz [*Balsley and Gage*, 1980]. At the right side of Equation 3.1, the first two terms represent the contributions due to bound electrons inherent in density fluctuations of water vapor and dry air, respectively. They are normally more important in the troposphere and stratosphere (below ~50 km). The third term, however, only begins to become significant at altitudes above 50 km and dominant at PMSE altitudes. I.e., the irregularities in the refractive index for PMSE observations are mainly given by the electron density fluctuations caused by neutral air turbulence which in turn is produced by gravity waves propagating from the troposphere as well as by the presence of large positive ion clusters and charged aerosols due to ambipolar forces [*Kelley et al.*, 1987; *Cho et al.*, 1992].

The assumption that PMSE originate from incoherent scatter was easily ruled out due to the low electron densities of ionospheric D-region (equivalent reflectivities of 5×10^{-19} m^{-1} for incoherent scatter compared with 10^{-12} m^{-1} for PMSE signals at 50 MHz). On the other hand, PMSE must be a consequence of coherent scatter due to the large echo intensities as well as the very narrow Doppler spectra [*Röttger and LaHoz*, 1990]. However, the early efforts to attribute the generation mechanism of PMSE to neutral air turbulence led to a paradox that the typical mesospheric turbulence is not strong enough to account for the observed radar cross sections [*Balsley et al.*, 1983; *Hocking*, 1985]. Figure 3.1 shows the energy spectrum of turbulence (or a tracer for turbulent motion) for typical mesospheric condition. This spectrum can be split into several parts based on the physical processes that dominate at the corresponding scales. According to the prediction by *Kolmogorov* [1941], the process of turbulent motions in the atmosphere is described as follows: (1) energy from large-scale mean flows and waves (energy subrange) is converted to turbulent eddies by instabilities, and (2) the eddy kinetic energies are transferred to smaller eddies by vortex stretching mechanism (buoyancy subrange and inertial subrange) until (3) the eddies become so small to be destroyed by molecular viscosity (viscous subrange). In this thesis, the inertial subrange (where the inertial forces are dominating) and viscous subrange (where the kinetic energies are dissipated to heat by viscous forces) are under our interest. For one-dimension velocity fluctuations, the spectrum is characterized by a wavenumber dependence of $k^{-5/3}$ in the inertial subrange whereas by a much faster drop off (a dependence of $\sim k^{-7}$) in the viscous subrange. The Bragg wavelength has to be larger than the inner scale of turbulence (marked in Figure 3.1) in order to avoid rapid destruction of the irregularities in the electron density distribution. In the classical turbulence theory, the inner scale can be calculated as $l_0^H = 9.90 \cdot \eta_K = 9.90 \cdot (\nu^3/\epsilon)^{1/4}$, where $\eta_K = (\nu^3/\epsilon)^{1/4}$ is termed as Kolmogorov microscale, ν is the kinematic viscosity, and ϵ is the turbulent energy dissipation rate [*Heisenberg*, 1948; *Lübken*, 1997]. In order to satisfy $l_0^H = 3$ m (for a radar frequency of 50 MHz), we use $\nu = 1\ \mathrm{m^2/s}$ as an appropriate value at the summer mesopause and arrive at an energy dissipation rate of $\epsilon \sim 100$ W/kg, corresponding to a heating rate of 8640 K/d ($dT/dt = 0.0864 \cdot \epsilon$, where dT/dt on K/d and ϵ on mW/kg) which is far too large and unrealistic in comparison to the typical values on the order of 10–20 K/d based on the experimental data [*Lübken et al.*, 2002].

Since there is no doubt that the occurrence of PMSE is strongly dependent on the existence of structures in the electron density distribution [e.g. *Lübken et al.*, 1993], the major tasks to explain the generation mechanisms of PMSE are to identify the physical processes responsible for the creation of these structures which are unlikely produced by the neutral air turbulence alone. However, it was proposed by *Kelley et al.* [1987] and *Cho et al.* [1992] that the existence of large cluster ions and charged ice particles should result in the reduction of electron diffusivity due to ambipolar forces. The destruction of these small-scale irregularities should hence be restrained such that irregularities possessing Bragg scales of the VHF radars have the opportunity to exist thereby leading to strong backscatter observed as PMSE. This situation is described by a parameter termed Schmidt number $Sc = \nu/D$, where ν is the kinematic viscosity of air and D is the electron diffusion coefficient. If Sc is significantly larger than 1, the power spectrum can extend to much smaller scales and hence should reveal a so-called viscous convective subrange between the inertial subrange and the viscous subrange which is characterized by a k^{-1} dependence (see Figure 3.2) [*Batchelor*, 1959], i.e., the power spectrum of such tracers extends to much smaller scales than the spectrum of the turbulent velocity field itself. In other words, if the electron diffusion coefficient is much smaller than the kinematic viscosity of air, the irregularities in the electron density distribution at the Bragg scale of a VHF or even UHF radars could have the chance to persist and lead to the radar backscatter observed as PMSE.

In summary, there are two prerequisites, i.e., charged ice particles and neutral air turbulence responsible for the creation of PMSE according to the work by *Cho et al.* [1992]. Importantly, it was well confirmed that PMSE are closely correlated with another mesospheric phenomenon, i.e., noctilucent clouds (NLC) which have long been known as direct evidence for ice particles of nanometer size existing near the summer polar mesopause from the optical observations [*Nussbaumer et al.*, 1996; *von Zahn and Bremer*, 1999]. Furthermore, electron

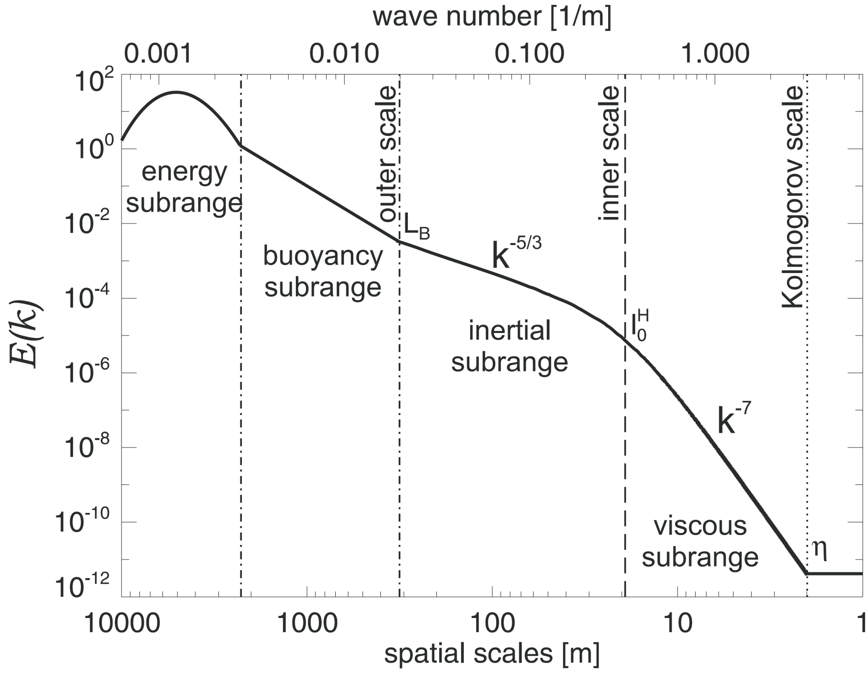

Figure 3.1: Energy spectrum of a passive turbulent tracer for typical mesospheric conditions. The spectrum was derived using the spectral model of *Heisenberg* [1948] for the altitude of ~85 km (i.e., kinematic viscosity $\nu = 1m^2/s$) and mean dissipation rate ($\epsilon = 0.7mW/kg$) as measured by *Lübken et al.* [2002]. The upper abscissa represents the spatial scales of a turbulent structure l, which is converted from the wavenumber k, i.e., $l = 2\pi/k$. This Figure is reproduced from *Strelnikov* [2006].

density depletion or biteout at the PMSE altitudes were observed with sounding rockets [*Ulwick et al.*, 1988; *Inhester et al.*, 1990; *Lübken et al.*, 1998] as well as with the EISCAT UHF radar [*Röttger et al.*, 1990] which was interpreted as the electron attachment on the subvisible ice particles with typical radii of ~10 nm [*Reid*, 1990; *Rapp and Lübken*, 2001]. In addition, the assumption of the existing subvisible ice particles was directly proven with rocket-borne observations [*Havnes et al.*, 1996; *Mitchell et al.*, 2001; *Smiley et al.*, 2003; *Rapp et al.*, 2009] and further supported by an active HF heating experiment [*Chilson et al.*, 2000]. The heating experiments were theoretically explained by *Rapp and Lübken* [2000, 2003] that the enhanced electron temperature counteracted the reduction of electron diffusion due to the charged ice particles. However, the coexistence of neutral air turbulence and PMSE was partially doubted by, for example, *Lübken et al.* [1993, 2002] who carried out common-volume measurements of neutral air turbulence with sounding rockets and PMSE revealing that neutral air turbulence only existed in the upper part of the altitude ranges with PMSE and concluded that other physical processes than neutral air turbulence must be involved in the generation mechanism of PMSE.

It is a common feature of PMSE conditions that the lower part of PMSE does not coexist with neutral air turbulence but with large ice particles optically observed as NLC (radius > 20 nm) [*Rapp et al.*, 2003b]. The existence of charged ice particles can compensate the PMSE-favorite condition in the absence of neutral air turbulence since the lifetime of the irregularities strongly depends on the radii of ice particles. Figure 3.3 shows the decay time for a decay by 10 dB as a function of ice particle radii in the scope of electron diffusion in the vicinity of charged ice particles. Evidently, for ice particles smaller than 10 nm the decay

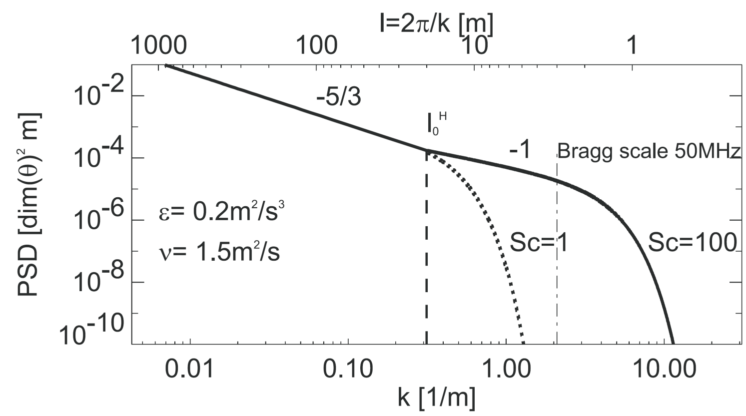

Figure 3.2: Power spectral density of a passive tracer θ for two different Schmidt number of $Sc = 1$ and $Sc = 100$, respectively. The upper abscissa represents wavelengths converted from wavenumbers. The numbers '-5/3' and '-1' indicate the wavenumber dependence at the scales shown. The vertical dashed line indicates the inner scale and the vertical dashed-dotted line indicates the Bragg scale of a 50 MHz radar. This Figure is reproduced from *Rapp and Lübken* [2004].

time is rather short (< 10 min). Due to the quadratic dependence of the decay time on the ice particle radii, the decay time is already 40 min for ice particles with a radius of 20 nm and even ∼4 hours for ice particles with a radius of 50 nm which do exist in an NLC environment.

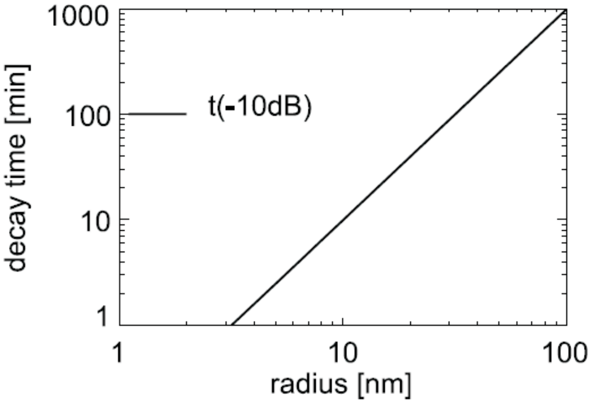

Figure 3.3: Radar scatter decay time for a relative reflectivity decrease by 10 dB after the PMSE generation mechanism has ceased. This figure is reproduced from *Rapp and Lübken* [2003].

Having this relation at hand, we may go back to the dilemma presented by *Lübken et al.* [1993, 2002] who found there was no neutral air turbulence present at the lower part of PMSE (say below ∼85 km) and hence no generation mechanisms for the creation of the small scale fluctuations in the electron densities. For particles with a radius larger than say 15 nm, their long lifetime (∼22.5 min) 'freezes' in the plasma structures (they originate from turbulent advection and are hence termed as 'fossil' turbulent structures [*Woods et al.*, 1969; *Cho et al.*, 1996]) such that PMSE also occur in the absence of neutral air turbulence. Furthermore, the model ideas presented by *Rapp and Lübken* [2003] can indeed explain the statistics of PMSE observations based on the available data of turbulence observations [*Rapp et al.*, 2003a].

Therefore there is a consensus among the researchers regarding the scattering mechanisms of PMSE that the charged ice particles in a nanometer size range play a crucial role on the generation of PMSE. The current standard theory of PMSE with the largest acceptance in the scientific community can be summarized that the echoes originate from turbulence-induced scatter in combination with a large Schmidt number caused by the presence of charged ice particles (the TWLS-theory). This theory has since been further extended by several authors [*Rapp and Lübken*, 2004; *Lie-Svendsen et al.*, 2003; *Rapp et al.*, 2008; *Nicolls et al.*, 2009; *Strelnikova and Rapp*, 2011; *Varney et al.*, 2011].

In the frame of the TWLS-theory of PMSE, *Rapp et al.* [2008] have deduced the theoretical expression of the radar volume reflectivities in the viscous convective subrange of turbulence:

$$\begin{aligned} \eta &= 8\pi^3 \cdot \frac{f_\alpha \cdot q \cdot Ri}{Pr^t} \cdot \frac{\sqrt{\epsilon\nu}}{N^2} \cdot \widetilde{M_e}^2 \cdot r_e^2 \cdot \frac{1}{k^3} \cdot \exp\left(-\frac{2\eta_K^2}{Sc} \cdot k^2\right) \\ &= C(\epsilon, n_e, N, H_n) \times \frac{1}{k^3} \cdot \exp\left(-\frac{2\eta_K^2}{Sc} \cdot k^2\right) \end{aligned} \qquad (3.2)$$

where ϵ is the turbulent energy dissipation rate, ν is the kinematic viscosity, N is the buoyancy frequency, $k = 4\pi/\lambda$ is the Bragg wavenumber of the radar, $\eta_K = (\nu^3/\epsilon)^{\frac{1}{4}}$ is the Kolmogorow microscale, r_e is the classical electron radius, and $Sc = \nu/D_e$ is the Schmidt number introduced in Chapter 1. $\widetilde{M_e}$ is the reduced potential refractive index gradient, i.e., $\widetilde{M_e} = \frac{n_e N^2}{g} - \frac{dn_e}{dz} - \frac{n_e}{H_n}$ which depends on the electron number density n_e, the buoyancy frequency, and the density scale height H_n. Finally, f_α, q, Ri and Pr^t are all 'constants' (i.e., they are constant for a given event) derived from either theory or by comparison with observations (see Appendix A in *Rapp et al.* [2008] for more details).

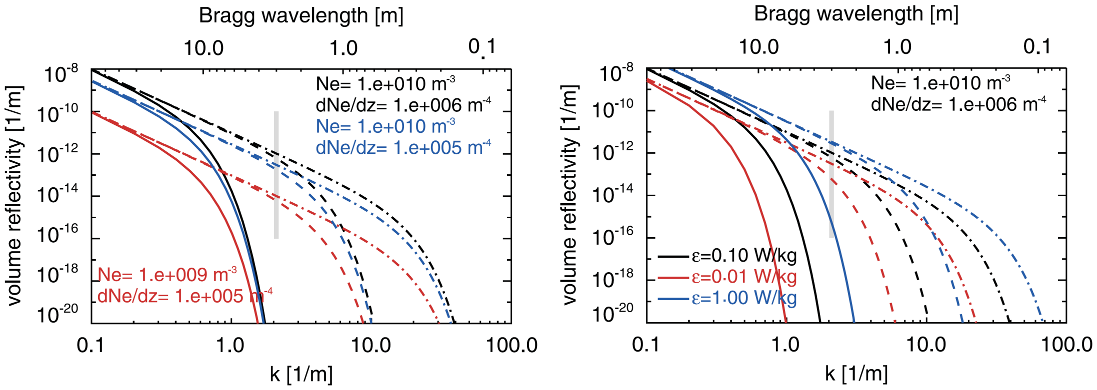

Figure 3.4: Left panel: calculated volume reflectivities for turbulent backscatter for a turbulent energy dissipation rate of 0.1 W/kg and electron number densities ne and electron number density gradients dne/dz indicated in the insert. Solid, dashed and dashed-dotted lines were calculated for $Sc = 1$, 50 and 1000, respectively. The grey vertical bar indicates the range of values observed by the ALWIN radar (Bragg wavelength of ∼3 m). Right panel: same as left panel, but for different values of the turbulent energy dissipation rate ϵ and fixed electron number densities ne and electron number density gradients dne/dz. This figure is reproduced from *Rapp et al.* [2008].

With further consideration on Equation 3.2, please note that the radar volume reflectivity at a given wavenumber is mainly determined by three important parameters, i.e., ϵ is the turbulent energy dissipation rate and the Kolmogorov microscale $\eta_K = (\nu^3/\epsilon)^{1/4}$ depends on ϵ; $\widetilde{M_e}$ can be derived from the electron number densities and the electron number density gradients; Schmidt number Sc is closely correlated with the size of ice particles, given by $Sc = 6.5 \cdot r_A^2$ where r_A is the radii of charged ice particles involved. Figure 3.4 illustrates the spectral dependence of the volume reflectivities for different combinations of the Schmidt number, the turbulent energy dissipation rate, and the electron density and its gradient. We note that the Schmidt number plays an overwhelming role that it can change the volume reflectivities at a given wavenumber k by several orders of magnitude, an effect which is more significant for smaller scales (i.e., higher frequencies of radars). For a fixed Schmidt number, however, also the turbulent energy dissipation rate and the electron density and its gradient may modify the volume reflectivities by considerable factors.

The first experimental test of this theory was presented by *Rapp et al.* [2008] who analyzed the simultaneous and common-volume observations of PMSE with the EISCAT VHF and UHF radar operating at 224 MHz and 930 MHz, respectively. During a short period of 5 minutes when both radars observed PMSE, they argued that the Schmidt number Sc was about constant with a value larger than 1000. Please note that this assumption of Sc is geophysically reasonable since it has long been well confirmed that the charged ice particles with radii r_A up to 100 nm do exist near the polar summer mesopause ($Sc = 6.5 \cdot r_A^2$). They finally found the volume reflectivities η are proportional to the factor $\sqrt{\epsilon} \times \widetilde{M_e}^2$ as expected from the TWLS-theory. In addition, the simultaneous observations with the ALWIN and the EISCAT VHF/UHF radar at three different frequencies allowed to compare the observed volume reflectivities η to theory assuming an appropriate value of Schmidt number. With an assumption of a Schmidt number $Sc = 2500$ *Rapp et al.* [2008] reached the best fit between the simulations and observations (see their Figure 8).

Chapter 4

Experimental facilities and data sets

In this thesis, measurements of PMSE were carried out using the EISCAT radars and the SOUSY radar at different frequencies. The EISCAT Svalbard radar (ESR) and the SOUSY Svalbard radar (SSR), collocated in Spitsbergen (78°N, 16°E), are operating at 500 and 53.5 MHz, respectively, whereas the EISCAT VHF and UHF radar, collocated in Tromsø (69°N, 19°E), are operating at 224 and 930 MHz, respectively. The aim of this section is to present a short description of the corresponding experimental details. This chapter begins with an introduction of incoherent scatter and the available incoherent scatter radars around the world as well as the highlight of the EISCAT radars (Section 4.1). This part is followed by a description of the configuration of the radars and the layout of the data set (the EISCAT VHF and UHF radar in Section 4.2 and the ESR and SSR in Section 4.3, respectively).

4.1 Incoherent scatter radars

Incoherent scatter (IS) or Thomson scatter is the scatter of electromagnetic radiation from free electrons in the ionospheric plasma which are mainly coupled with the much slower, massive positive ions. Hence the parameters such as their temperature and velocity can be derived from the spectra of the received signals. When an electromagnetic wave is transmitted, e.g., by a radar, into ionosphere, the electric field of the incident wave accelerates the electrons or/and ions, consequently causing them emit radiation at the same frequency as the incident wave and thus the wave is scattered. For an electron, the cross section of incoherent scatter is only $\sigma_{IS} = 6.65 \times 10^{-29}$ m^2. With the electron density of 10^{10} m^{-3} at 85 km, the equivalent volume reflectivity is 6.65×10^{-19} m^{-1} which is much weaker compared with the coherent scatter of PMSE (10^{-12} m^{-1} at a frequency of 50 MHz). Hence it has been assumed that incoherent scatter is undetectable for a very long time. It is proposed by *Gordon* [1958], however, that incoherent scatter from the ionospheric plasma should be detectable using high-power and large-aperture radars, leading to the possibility to probe ionosphere based on incoherent scatter. This idea was soon confirmed by *Bowles* [1958] who recorded the very first incoherent scatter echoes from the ionosphere using a radar with a frequency of 41 MHz and a peak power of 4–6 MW. In addition, the observed signals were much stronger than expected and the bandwidth was less than the receiving filter bandwidth, which is attributed to the influence of ions in the plasma. The unexpected findings demonstrated the profound potential of incoherent scatter radars (ISR) in the exploration of the atmosphere. It is now well known that a number of parameters of ionospheric plasma, e.g., electron density, ion temperature, plasma velocity etc, can be deduced from the spectra of incoherent scatter signals. Today, there are a handful of ISRs built around the world, i.e., Arecibo, Jicamarca, Sondrestrom, Millstone Hill, Irkutsk, Kharkov, MU, EAR, ALTAIR, AMISR and EISCAT ISR, making a network of the powerful ground-based sounding instruments for the study of the atmosphere.

The European Incoherent Scatter scientific association (EISCAT) is an international association supported by research organizations in China, Finland, France (until end 2006), Germany, Japan, Norway, Sweden and the United Kingdom. The EISCAT operates three Incoherent Scatter radar systems, i.e., the ESR located near Longyearbyen (78°N, 16°E) on the north polar island of Spitsbergen which is part of the archipelago Svalbard and the EISCAT VHF and UHF radar at Ramfjordmoen near Tromsø, Norway (69°N, 19°E) with two additional UHF (930 MHz) receiver stations located in Kiruna, Sweden, and Sodankylä, Finland, respectively. See Figure 4.1 for the locations of the here operated radars. The EISCAT radars are generally used to study the interaction between the Sun and the Earth as revealed by disturbances in the ionosphere and magnetosphere. Due to their locations at high latitudes, nevertheless, they have been used to observing PMSE with appropriate programs (mainly the modulations termed 'arc-dlayer' and 'manda') in the last decades [e.g., *Röttger et al.*, 1988; *Hoppe et al.*, 1988; *Röttger et al.*, 1990; *Rapp et al.*, 2008].

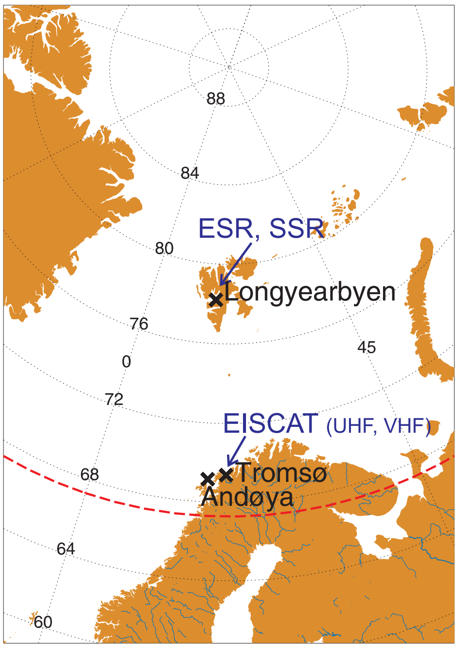

Figure 4.1: The locations of the here used radars: the ESR and SSR collocated near Longyearbyen (78°N, 16°E) on Svalbard; the EISCAT VHF and UHF radar collocated near Tromsø (69°N, 19°E), Norway.

4.2 The EISCAT VHF and UHF radar

The EISCAT VHF radar operates at 224 MHz corresponding to a Bragg wavelength of 67 cm, using four 30m×40m steerable parabolic cylinder antennas. The full antenna has a half-power full-width of 1.2°×0.85° and maximum peak power of 3 MW. During the period of all here described observations, half of the antennas were working and hence the VHF radar was run with a peak power of 1.5 MW and a 3-dB beam width of 1.2°×1.7° corresponding to an oval diameter of 1.8km×2.5km at the altitude of 85 km. The EISCAT UHF radar operates at 930 MHz corresponding to a Bragg wavelength of 16 cm, using a fully steerable parabolic dish with a diameter of 32 meters. It was run with a peak power of 2 MW and the 3-dB beam width is 0.5° corresponding to a diameter of 0.7 km at the altitude of 85 km. Detailed descriptions of the EISCAT VHF and UHF radar can be found in *Baron* [1986] and *Folkestad et al.* [1983], respectively. PMSE were successfully detected for the first time with the EISCAT VHF radar in the summer of 1987 [*Hoppe et al.*, 1988; *Röttger et al.*, 1988] and with the EISCAT UHF radar in the summer of 1988 [*Röttger and LaHoz*, 1990].

4.2.1 Configuration

EISCAT designed 7 pulse modulation schemes for common programs (CP). Based on them, different experiment programs (special programs or SP) were designed and run for different scientific desires. These special programs yield different time and altitude resolution and different range coverage (see *Turunen et al.* [2002] and www.eiscat.com for details). In order to deal with a homogeneous data set, we only consider PMSE observations from the year 2003 onward. All corresponding observations with the EISCAT VHF and UHF radar were conducted using the so-called 'arc-dlayer' modulation. This is designed for the study of the ionospheric D-region and lower E-region covering the PMSE altitudes which is poorly studied with incoherent scatter radars due to the low electron density. Note that 'arc-dlayer' is a further development of another low altitude modulation described in detail in *Turunen et al.* [2002]. For special periods we also consider observations made with a special version of 'arc-dlayer' termed as 'arc-dlayer-ht'. This special version has a higher time resolution but covers the same height range and has the same height resolution as 'arc-dlayer'. Further technical parameters of our observations as well as more details on the experiment configuration are summarized in Table 4.1 and 4.2, respectively.

4.2.2 Data

The primary data deduced from the experiment programs with the EISCAT VHF and UHF radar is the autocorrelation function (ACF) that is the Fourier transform of the power spectral density (PSD). The ACF has 127 lags with a lag interval of 1.35 ms for 'arc-dlayer' and 1.56 ms for 'arc-dlayer-ht' (see Table 4.2 for more details) giving a frequency resolution of 2.89 Hz for 'arc-dlayer' and 2.51 Hz for 'arc-dlayer-ht' (see Table 4.2 for more information). The data acquisition channels of both radars cover altitudes from 59.7 to 139.5 km with a range resolution of 300 m (i.e., height resolution owing to the radar beam vertically pointing for all the observations). The integration time depends on the experiment and analysis, but was 5 sec for 'arc-dlayer'-experiment and 2 sec for 'arc-dlayer-ht'-experiment.

The measurements analyzed in this thesis were carried out with the EISCAT VHF radar during 2003–2007 (total of 523 hours with more than 300 hours of PMSE-detection) and also with the UHF radar in July 2004–2005 (total of 76 hours). A detailed list of the simultaneous VHF- and UHF-observations is presented in Table A.4. Note that there are only a handful of PMSE observations with the EISCAT UHF radar reported in the literature so far [*Turunen et al.*, 1988; *Collis et al.*, 1988; *Röttger et al.*, 1990; *La Hoz et al.*, 2006; *Belova et al.*, 2007; *Rapp et al.*, 2008; *Naesheim et al.*, 2008]. Since the two radars are collocated, these measurements are very well suited for investigating the frequency dependence of PMSE and provide an excellent experimental possibility to test any potential theory of PMSE.

Table 4.1: Radar system parameters

	EISCAT VHF	EISCAT UHF
Frequency (MHz)	224	930
Wavelength λ (m)	1.34	0.32
Bragg wavelength $\lambda/2$ (m)	0.67	0.16
Bragg wavenumber $4\pi/\lambda$ (m^{-1})	9.38	39.27
Antenna gain (dBi)	46	48
Half-power beam width (°)	1.2×1.7 (half antenna)	0.5
Peak power (MW)	1.5 (half antenna)	2
Range resolution (m)	300	300
System temperature (K)	250-350	110

Table 4.2: Experiment configuration

	arc_dlayer		arc_dlayer_ht	
	VHF	UHF	VHF	UHF
Time resolution (s)	5	5	2	2
Number of samples	128	128	128	128
Lag resolution (ms)	1.35	1.35	1.562	1.562
Spectral resolution (Hz)	2.9	2.9	2.51	2.51
Velocity resolution (m/s)	1.942	0.47	1.68	0.4

The measurements by the EISCAT radars are routinely analyzed in terms of electron number densities (or 'apparent' electron densities for the case of PMSE) by comparing measured power values to the measurements of a calibration source of known brightness temperature and by using IS theory. From previous comparison of pure incoherent scatter echoes (where the volume reflectivity is directly proportional to electron density) with ionosonde data this technique is known to yield volume reflectivities within an accuracy of ~10% [*Kirkwood et al.*, 1986]. In our case, the analysis was done using the well documented 'GUISDAP' software package and taking into account measurements with the local ionosonde (see *Lehtinen and Huuskonen* [1996] and www.eiscat.se for details). Such derived apparent electron number densities can be converted to volume reflectivities using the well known relation

$$\eta = \sigma \times N_e \tag{4.1}$$

where $\sigma = 5 \times 10^{-29}$ m^2 is half the scattering cross section σ_e of an electron ($\sigma = \sigma_e \times (1 + T_e/T_i)^{-1} = \sigma_e/2$) and N_e is the 'apparent' electron number density [e.g., *Röttger and LaHoz*, 1990]. With 'apparent', we mean that the signal is certainly not a measure of real electron density but due to coherent scatter of PMSE which is superposed to the real electron density for data acquisition.

4.3 The ESR and the SSR

Just like the EISCAT VHF and UHF radar, the EISCAT Svalbard Radar (ESR) is also an incoherent scatter radar which is operating at 500 MHz corresponding to a Bragg wavelength of 30 cm. It comprises two parabolic dish antennas, a fixed field-aligned 42-m antenna and a fully steerable 32-m antenna, approximately, 130 m apart. During our experiment, however, only the 32-m steerable dish was run with a peak power of 0.8 MW and a 3-dB beam width of 1.2° corresponding to a diameter of 1.8 km at the altitude of 85 km. The SOUSY Svalbard Radar or SSR is an MST radar operating at 53.5 MHz corresponding to a Bragg wavelength of 2.8 m. It was constructed on Svalbard in 1998, particularly conceived for the studies of PMSE. The radar system has been operated by the Max-Planck-Institute for Solar System Research and by the University of Tromsø with substantial support by the Leibniz-Institute of Atmospheric Physics at Rostock University. The SSR uses the main basic components of the mobile SOUSY VHF radar [*Czechowsky et al.*, 1984]. Detailed descriptions of the ESR and SSR can be found in *Wannberg et al.* [1997] and *Röttger* [2001], respectively. Previous studies of PMSE using the ESR and SSR were published by *Hall and Röttger* [2001] and *Röttger* [2001] for the case of the ESR and, for example, by *Lübken et al.* [2004] and *Zecha and Röttger* [2009] for the case of the SSR.

Due to the unique location, the SSR is a very valuable facility since it can continually monitor PMSE at high polar latitude [e.g., *Zecha and Röttger*, 2009] attributing to study the statistical properties and the latitude dependence of PMSE. The SSR is also collocated with the 31-MHz NSMR radar (Nippon/Norway Svalbard Meteor) and the SPEAR (Space Plasma Exploration by Active Radar) system which is a new polar cap HF radar facility. Combined observations hence allow to be carried out to study the properties of PMSE at different frequencies with the ESR [e.g., *Röttger*, 2001] and the correlation of PMSE with the temperatures and horizontal winds observed with the NSMR [e.g., *Hall et al.*, 2002]. Furthermore, other sounding techniques also can be involved for collocated observations such as with rockets and lidars [e.g., *Lübken et al.*, 2004; *Strelnikov et al.*, 2006].

4.3.1 Configuration

The antenna system of the SSR consists of 356 four-element Yagis in an almost circular array used for both transmission and reception. Besides the vertical beam direction, the antenna can also be steered to 5° zenith angle in north-east, south-east, south-west and north-west azimuths corresponding to a diameter of 7.4 km at the altitude of 85 km, which is much larger compared to the ESR (a diameter of 1.8 km at 85 km). During the period of our experiment, only the measurements with the vertical beam were conducted. For the mesosphere study, a 20-bit complementary code with 2 μs baud length was applied, corresponding to a range resolution of 300 m. During periods of the initial operations 1999–2001 and 2003–2004, the SSR was run at a peak power around 70 kW and an antenna gain of 33 dB [*Zecha and Röttger*, 2009]. For the measurements in 2006, however, the SSR was run using the 4-kW driver (pre-amplifier) but not the final amplifier resulting in a reduced peak power of 4 kW. Furthermore, due to the damage of half of the antennas assumed the SSR was run with a low antenna gain of 30 dB (see Table 4.3 for the system parameters of the SSR in details). These are the reasons why the occurrence rates of PMSE in 2006 were much lower (see Chapter 5) compared to the results in the earlier years shown by *Zecha and Röttger* [2009].

Just like the EISCAT VHF and UHF radar, the ESR also allows different experimental programs designed for different scientific desires. During the campaign observing PMSE with the ESR and SSR in June 2006, the observations with the ESR were conducted with a special program of 'jurg3' which is developed by J. Röttger. The ESR was operated in a special complementary code mode. This for the first time allowed the ESR to be used with the height resolution of 300 m which is equal to the height resolution of the SSR.

Further technical parameters of the ESR and SSR as well as more details on the experiment configuration are summarized in Table 4.3.

Table 4.3: ESR and SSR system parameters. For easier comparison to the earlier study by [*Röttger*, 2001], experiment parameters from this previous study are also listed in brackets.

	ESR	SSR
Frequency (MHz)	500	53.5
Wavelength (m)	0.60	5.61
Antenna gain (dBi)	42.5	30.0 (33.0)
Half-power beam width (°)	1.23	5 (4.5)
Peak power (MW)	0.8	0.004 (0.06)
Radar code	complementary, no phase flip	complementary, with phase flip
Number of code bauds	128 (32)	20
System efficiency (assumed)	0.8	0.8
Baud length (μs)	2 (6)	2
Range resolution (m)	300 (900)	300
Number of coherent integration	4 × 2 (# × code pairs)	16 × 2 × 2 (# × code pairs × phase flip)
System temperature (K)	60	3000

4.3.2 Data

The measurements we report here were obtained in June 2006. During this period, the SSR was run continuously, whereas the ESR was run for 1–4 hours during 18 days around noon. A detailed list with the exact times of ESR-operation and the hours during which PMSE were observed is presented in Table A.3. The primary data deduced from the experiment programs with the ESR are autocorrelation function (i.e., ACF) as well as the undecoded raw data which were decoded to time series. The ACF has 600 lags (with 4 incoherent integration done) with a lag interval of 2.5 ms giving a frequency resolution of 0.33 Hz. For the SSR, the data dumps, each with 128 data points, are ~10 sec long time series with 64 coherent integration done online to reduce the data flow. From these measurements signal power values, vertical velocities, and spectral widths were determined from 6 sec long time series in the case of the ESR, and 10 sec long time series in the case of the SSR, respectively. In order to compare the ESR and SSR observations, both data sets were projected onto a joint time grid with 1 min resolution. That is, 10 (6) spectra of 6 sec (10 sec) long ESR (SSR) time series were first corrected for their Doppler velocity and then incoherently averaged over 10 (6) spectra. We note that unlike in the study of *Zecha and Röttger* [2009], the SSR was constantly pointed vertically, i.e., no Doppler beam swinging experiments were performed such that no horizontal wind information is available from the PMSE-observations itself. In addition both radars were calibrated and power values were converted to absolute volume reflectivities for quantitative comparison to each other and to theory. Corresponding results are described in the next section.

Chapter 5

Results: statistical properties of PMSE

It is introduced in Chapter 2 that studies of PMSE have been most intensely carried out with radars at about 50 MHz during the last 30 years providing a general picture of the statistical features of PMSE. However, systematic studies of PMSE at higher frequencies than 50 MHz are rather scarce leading to poor statistics of PMSE at these frequencies [see *Rapp and Lübken*, 2004, for an overview of PMSE observations at different frequencies]. Based on the theoretical expectation as well as the available experimental record, PMSE reveal a tremendous frequency dependence, namely, that the PMSE occurrence rate and volume reflectivity drastically drop with increasing radar frequencies (hence decreasing Bragg wavelengths). Furthermore, very few observations of PMSE have been carried out using calibrated radars and more than one frequency at the same time and same place. A cautionary note should since be kept in mind when one draws any conclusions on the frequency dependence of PMSE due to the different configuration of different radar systems (hence operating radars should be calibrated) as well as the different geophysical situation (hence operating radars should be collocated). In the current study, the aim is to further fill the gap of systematic PMSE studies at frequencies higher than the 'standard' 50 MHz and also to obtain further insight into the frequency dependence of PMSE. We hence consider observations of PMSE with the ESR (500 MHz) and SSR (53.5 MHz) in the summer of 2006 as well as with the EISCAT VHF radar (224 MHz) in summer seasons between 2003 and 2007 and with the EISCAT UHF radar (930 MHz) in July 2004 and 2005. With 5 summers of observations with the EISCAT VHF radar, we proceed with the study of the temporal variability of PMSE at 224 MHz, which has been frequently done with radars at ∼50 MHz [e.g., *Bremer et al.*, 2006, 2009].

5.1 Observations at frequencies of 53.5 and 500 MHz

In this section, we will proceed with the statistical properties of PMSE in term of occurrence rate and volume reflectivity derived from the observations at frequencies of 53.5 and 500 MHz.

5.1.1 PMSE occurrence rates

Figure 5.1 shows two typical examples of simultaneous PMSE observations with the ESR and SSR on 18 and 20 June 2006, respectively. In the two cases shown in Figure 5.1 both radars show prominent echoes in approximately the same altitude range, where, however, the

SSR-echoes generally extend over a larger altitude range than the ESR-echoes.

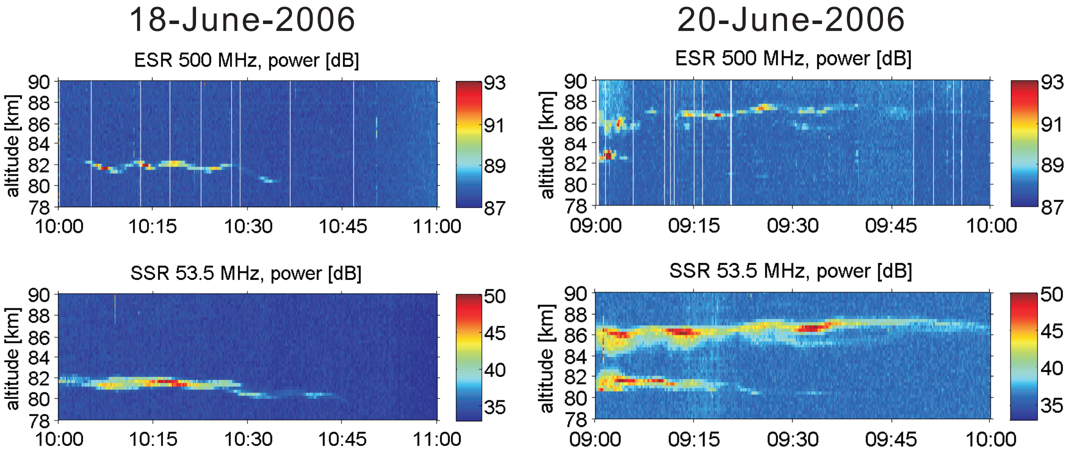

Figure 5.1: Height-time-intensity plots of the radar echoes observed with the (top) ESR at 500 MHz and (bottom) SSR at 53.5 MHz on (left) 18 and (right) 20 June 2006. White vertical lines in the top plots indicate times where meteor echoes were removed.

In a first step, all of the observations obtained in 2006 (see Table A.3) were used to infer occurrence rates as a function of altitude. In this study, occurrence rate is defined as the percentage of PMSE events in all the observations which possess a time resolution of 1 min. For the case of the ESR-data set, this analysis was carried out on single power profiles, where echoes which extended more than three standard deviations above the mean noise level (equivalent to an SNR-threshold of +0.5 dB) were identified as PMSE. We note that any choice of a threshold for PMSE is somewhat arbitrary. In this case, our choice was mainly driven by the detectability of the rather weak echoes observed by the ESR and revealed to be the optimum compromise between the requirement to miss as few as possible real PMSE but also to suppress as many as possible false detections. In addition, in order to avoid false PMSE-detections in the ESR-data due to possible contamination by occasionally detectable incoherent scatter, we also investigated the corresponding spectral widths. These are expected to be much larger in the case of incoherent scatter at this frequency and in the 80–90 km altitude range as compared to the coherent scatter of PMSE [e.g., *Röttger and LaHoz*, 1990]. For the case of the SSR-data set, we adopted the methodology used by *Zecha and Röttger* [2009] who defined a SNR-threshold of -10 dB for PMSE-detection for similar observing conditions (see Figure 5.2 and further details provided in the figure caption).

Resulting altitude profiles of the occurrence rates for both frequencies are shown in Figure 5.3. The occurrence rates for the ESR are much smaller than those for the SSR. Furthermore, ESR PMSE occurred in a considerably narrower altitude range, i.e., between 81 and 88 km whereas SSR PMSE were observed in the entire altitude range between 80 and 92 km.

Since ESR observations were restricted to hours from 9–13 UT, we further compare the SSR PMSE-occurrence rate observed in the same period to the SSR PMSE-occurrence rate for all observations. This comparison shows that the SSR PMSE-occurrence rate is actually significantly larger during the 9–13 UT period than during the entire day. In Figure 5.4, we show the mean diurnal variation of the PMSE occurrence rate inferred from the SSR observations in June 2006 as a function of altitude and time. The maximum PMSE occurrence rate was observed at local noon (i.e., 09:00–10:00 UT) whereas the minimum occurred near 21:00–22:00 UT more or less over all the altitudes. This is in line with the diurnal pattern of

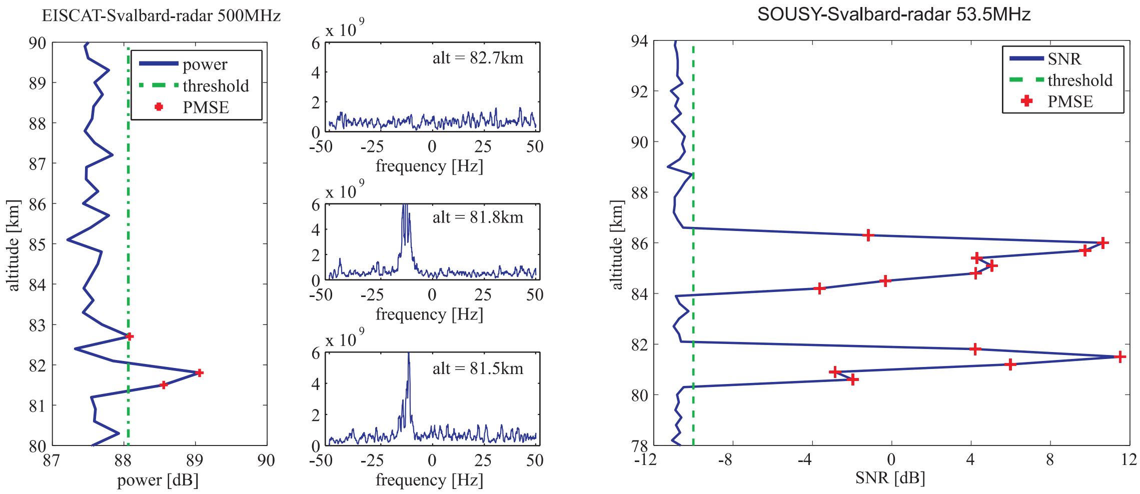

Figure 5.2: Left: ESR PMSE are defined as the echoes extending more than three standard deviations above the mean noise level and the power spectrum of the potential PMSE revealing a narrow spectral widths. Hence, the echoes at 81.5 and 81.8 km are PMSE signals whereas the echo at 82.7 km without revealing any narrow spectrum is assumed due to occasional enhancement of incoherent scatter, i.e., not PMSE. Right: SSR PMSE are defined as the echoes larger than a SNR-threshold of -10 dB.

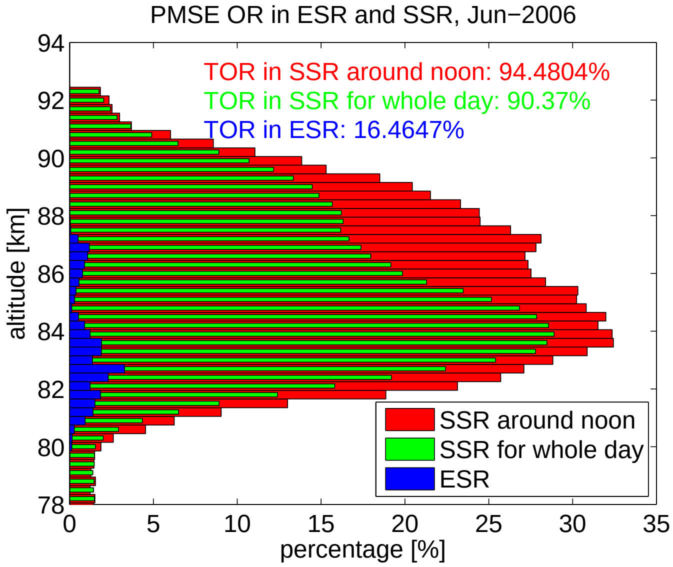

Figure 5.3: Comparison of PMSE occurrence rates at 500 MHz (blue) and 53.5 MHz (red and green) respectively derived from the ESR and SSR observations in June 2006. In the case of SSR-observations, the red histogram shows the PMSE occurrence rate during 9–13 UT, i.e., during the period when the ESR was run. The green histogram shows the PMSE occurrence rate observed with the SSR for all observations. The total occurrence rate (TOR), which indicates whether PMSE occurred in at least one altitude channel, is indicated in the insert.

PMSE occurrence at Svalbard described by *Zecha and Röttger* [2009] who found a maximum PMSE occurrence around local noon based on the SSR measurements during the years 1999–2001 and 2003–2004. According to *Zecha and Röttger* [2009] this maximum can be explained by the diurnal variation of solar UV and particle precipitation and corresponding enhanced

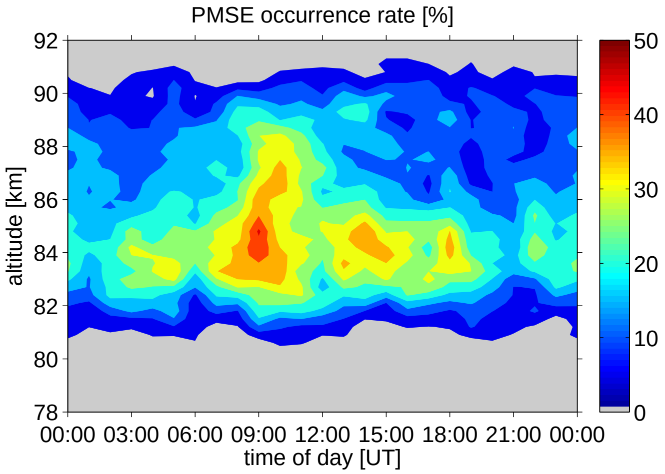

Figure 5.4: Diurnal variation of PMSE occurrence rate at 53.5 MHz as a function of altitude and time derived from the same observations as in Figure 5.3. The maximum occurrence was observed over a wide height range at the local noon (09:00–10:00 UT) which is in line with the work by *Zecha and Röttger* [2009].

electron densities at PMSE altitudes during the same period.

We also note in passing the apparent two maxima-structure of these profiles which is likely related to the influence of long period gravity waves on the layering of the ice particles. The interested reader is referred to *Hoffmann et al.* [2005, 2008] for a detailed discussion of this mechanism including additional references. In addition, *Zecha and Röttger* [2009] provide a detailed statistical analysis of the multi-layer occurrence in PMSE observed by the SSR in previous years.

5.1.2 Volume reflectivities

For a further quantitative comparison of our measurements with the ESR at a Bragg wavelength of 30 cm and the SSR at a Bragg-wavelength of 2.8 m, we next converted the measurements to absolute volume reflectivities, i.e., scattering cross sections per unit volume. In the case of the ESR, this was done on the basis of a noise calibration, i.e., a well known calibration noise source was switched on during each pulse reception interval and fed into the receiver system [see *Wannberg et al.*, 1997, their Figure 5]. By normalization of the received echo power to that of the calibration noise source, measured power-values were converted to values in units of Watts. Making additionally use of the radar equation and using the radar system parameters given in Table 4.3 volume reflectivities were finally derived. From previous comparison of pure incoherent scatter echoes (where the volume reflectivity is directly proportional to electron density) with ionosonde data this technique is known to yield volume reflectivities within an accuracy of ~10% [*Kirkwood et al.*, 1986]. Note that the latter estimate includes the variation of transmitted ESR-power which is routinely measured and logged during ESR operation.

In the case of the SSR, a delay line calibration was performed and verified against an additional noise calibration as described in detail in *Latteck et al.* [2008]. For the delay line calibration, the transmitter output itself is fed into the receiver input using a directional coupler and delaying the transmitted pulse by 100 μs (corresponding to a range of 15 km) using an ultra-sonic delay line. Since the transmitted power can be measured within an accuracy of less than 1% (i.e., better than 100 W at a transmitter output of a few kilowatts) this allows to express any received signal in absolute units within an accuracy of a few percent. Making again use of the radar equation and using the radar system parameters given in Table 4.3 volume reflectivities are derived. Unlike in the case of the ESR, a statement on the accuracy of this calibration procedure is more difficult, since independent measurements of the volume reflectivity are not available. However, based on the accuracy with which the delay line calibration can be carried out (accuracy of a few percent, see above) and also based on the variation of transmitted power which was regularly measured during the radar experiments described here we estimate the accuracy of this calibration to be on the order of a few ten percent.

We note that there could be additional systematic errors originating from the radar system parameters as summarized in Table 4.3 and as needed for the calculation of volume reflectivities. Where not measured directly, stated quantities were derived on a 'best effort' basis (e.g., the SSR antenna gain had to be calculated).

As the final result of this exercise, histograms of the volume reflectivities η obtained from PMSE observations with the ESR and SSR in June 2006 are presented in Figure 5.5. η-values obtained from the ESR and SSR observations fall within the range from 2.5×10^{-19} m^{-1} to 1×10^{-17} m^{-1} and from 5×10^{-16} m^{-1} to 6.3×10^{-12} m^{-1}, respectively. This means that SSR η-values at a Bragg wavelength of 2.8 m are on average more than three orders of magnitude larger than ESR η-values at a Bragg wavelength of 30 cm. A more detailed comparison of the volume reflectivities at these two frequencies along with an in depth discussion in terms of our theoretical understanding of PMSE is presented in Chapter 7.

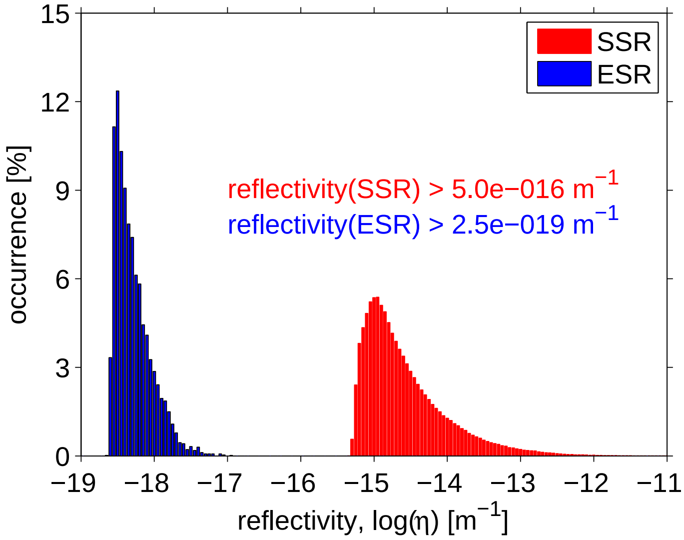

Figure 5.5: Histograms of absolute volume reflectivities at 500 MHz and 53.5 MHz derived from ESR (blue) and SSR (red) observations in June 2006. Minimum detectable values for both radars are indicated on the plot.

5.2 Observations at frequencies of 224 and 930 MHz

In this section, we will deal with the statistical properties of PMSE in occurrence rate and volume reflectivities derived from observations at frequencies of 224 and 930 MHz.

5.2.1 PMSE-occurrence rates

In Figure 5.6 we present two typical examples of simultaneous PMSE observed with the EISCAT VHF and UHF radar on 13 July 2004 and 09 July 2005, respectively. Note that during these two measurements, the HF heating facilities in the EISCAT Tromsø radar site were run. The details of the heating experiments were described by *Naesheim et al.* [2008]. *Naesheim et al.* [2008] demonstrated that the heating led to identical effects at both frequencies. For the current purpose, however, we are only interested in the undisturbed (i.e., not affected by heating) state of the echoes. In the current analysis, the heating parts of the observations were hence excluded from the data sets and the remaining observations were integrated over 1 min intervals. From Figure 5.6, we see that pronounced echoes were simultaneously observed by both radars for a quite long duration. The VHF echoes, however, generally extend over a larger altitude range than the UHF echoes and show more variations in the morphology (sometimes appearing with double-layer or even multi-layer structures), whereas the UHF echoes appear intermittently as a very thin layer.

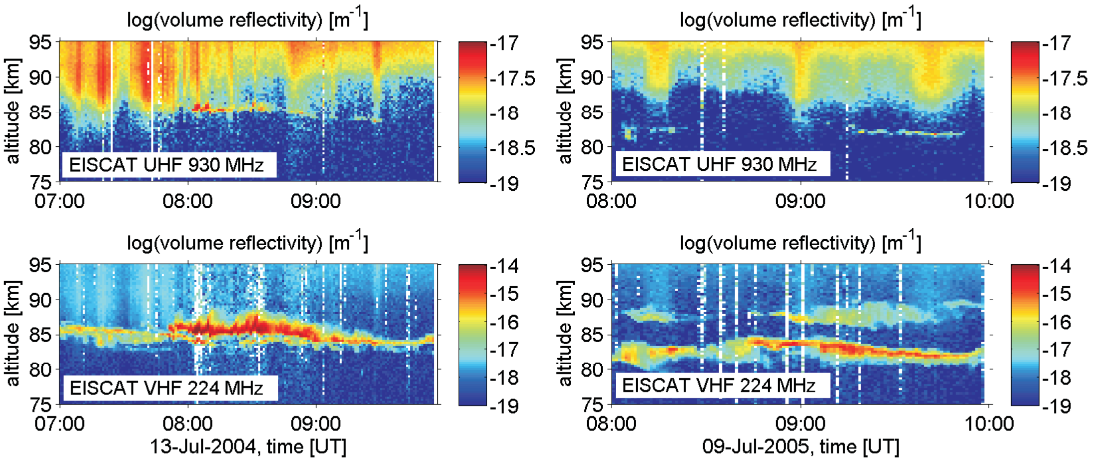

Figure 5.6: Volume reflectivities deduced from the observations with the EISCAT UHF radar (top) at 930 MHz and the EISCAT VHF radar at 224 MHz (bottom) on 13 July 2004 (left) and 09 July 2005 (right), respectively. The heating parts were removed before being integrated into 1 min. Blanks in all panels indicate times where meteor echoes were removed.

The EISCAT VHF and UHF radar are both incoherent scatter (IS) radar. The observations are hence a superposition of coherent scatter from PMSE and incoherent scatter from the ambient plasma at mesospheric altitudes. In order to isolate altitudes with PMSE, we inferred the occurrence rate based on power profiles. Following the methodology used by *Li et al.* [2010] (or see Section 5.1.1), the analysis was carried out on single power profiles, where echoes which extended more than three standard deviations above the mean noise level were identified as PMSE. For the case of UHF PMSE, the echoes are much weaker and most of the coherent scatter does not stand well out of the incoherent scatter. In order to avoid missing too many of the already scarce UHF PMSE we derived the threshold manually (effectively resulting in a PMSE-threshold of slightly below 3 standard deviations above background) and this analysis was limited to the height range of 80–88 km compared to the height range of 78–94 km for the case of VHF PMSE. In addition, in order to avoid the occasional contamination by incoherent scatter we also investigated the corresponding spectral widths of the potential PMSE derived by the above process, since it is known that the spectral widths are much smaller in the case of the coherent scatter of PMSE as compared to the incoherent scatter of the surrounding electron density [e.g., *Röttger and LaHoz*, 1990].

Figure 5.7 shows the resulting altitude profiles of the occurrence rates of VHF PMSE in different years between 2003 and 2007 and also the overall results for the 5 years of observations. The total occurrence rates (PMSE occur in at least one altitude channel) are indicated in the insert, respectively. In every year, VHF PMSE occurred almost in the entire altitude range between 80 and 91 km with the largest occurrence rate between 84 and 86 km. In addition, the result in 2004 shows the largest value with a total occurrence rate of 73%, which is consistent with the occurrence rate of NLC observed by the ALOMAR RMR lidar (69°N, 16°E) [*Fiedler et al.*, 2009]. A comparison between PMSE occurrence and NLC occurrence as well as a discussion of other factors affecting PMSE occurrence will be discussed in detail in Section 5.3. For the comparison of the PMSE occurrence rates inferred from the VHF and UHF observations, we made use of the simultaneous observations with both radars in July 2004 and 2005 (see also Table A.4), when UHF PMSE were detected over a considerably long period. Derived altitude profiles of the occurrence rates at both frequencies are shown in Figure 5.8. UHF PMSE show much smaller occurrence rates than VHF PMSE. Furthermore, UHF PMSE were observed in a considerably narrower altitude range, i.e., between 81 and 87 km.

Compared with the occurrence of PMSE observed with the ALWIN radar (53.5 MHz) at Andenes (69°N, 16°E) which shows up to 80% even in the long term average [*Bremer et al.*, 2009], the occurrence of PMSE observed with the EISCAT VHF radar at 224 MHz is quite low. In addition, the occurrence of PMSE observed with the EISCAT UHF radar at 930 MHz is even much lower than that with the EISCAT Svalbard radar at 500 MHz which reached 16% in June 2006 (see Section 5.1.1).

5.2.2 Volume reflectivities

In Figure 5.9 we present the statistical distribution of all volume reflectivities η as well as their normalized distribution versus altitude for the PMSE observations during different years from 2003 to 2007. The overall results of the five years are shown in the lower right panel. This shows that η values derived from the VHF observations fall within the range from 1×10^{-18} m^{-1} to 1.9×10^{-13} m^{-1}. The maxima of η, however, are quite different for the observations in different years. Corresponding η values for the years from 2003 to 2007 are listed in Table 5.1.

Making again use of the observations in July 2004 and 2005 with the EISCAT VHF and UHF radar, we next compared the volume reflectivities of PMSE observations at these two frequencies. Histograms of η as well as corresponding altitude-resolved distributions are presented in Figure 5.10. η-values obtained from the EISCAT VHF and UHF observations fall within the range from 1.35×10^{-18} m^{-1} to 1.58×10^{-14} m^{-1} with the maximum around 10^{-17} m^{-1} and from 1.95×10^{-19} m^{-1} to 7.01×10^{-18} m^{-1} with the maximum smaller than 10^{-18} m^{-1}, respectively. Focusing on the lower panels, we would like to stress that there are two patches in the distribution of the UHF PMSE which are consistent with corresponding maxima of the η-distribution for VHF PMSE around 86 km and 82–84 km. In Section 7.1, comparisons between the PMSE reflectivities at these two frequencies will be discussed further in terms of our theoretical understanding of PMSE.

5.3 Temporal variability of PMSE at 224 MHz

Unlike the continuously operated MST-radars at ~50 MHz, observations with the EISCAT radars were only performed on a campaign basis. However, over the years from 2003 to 2007

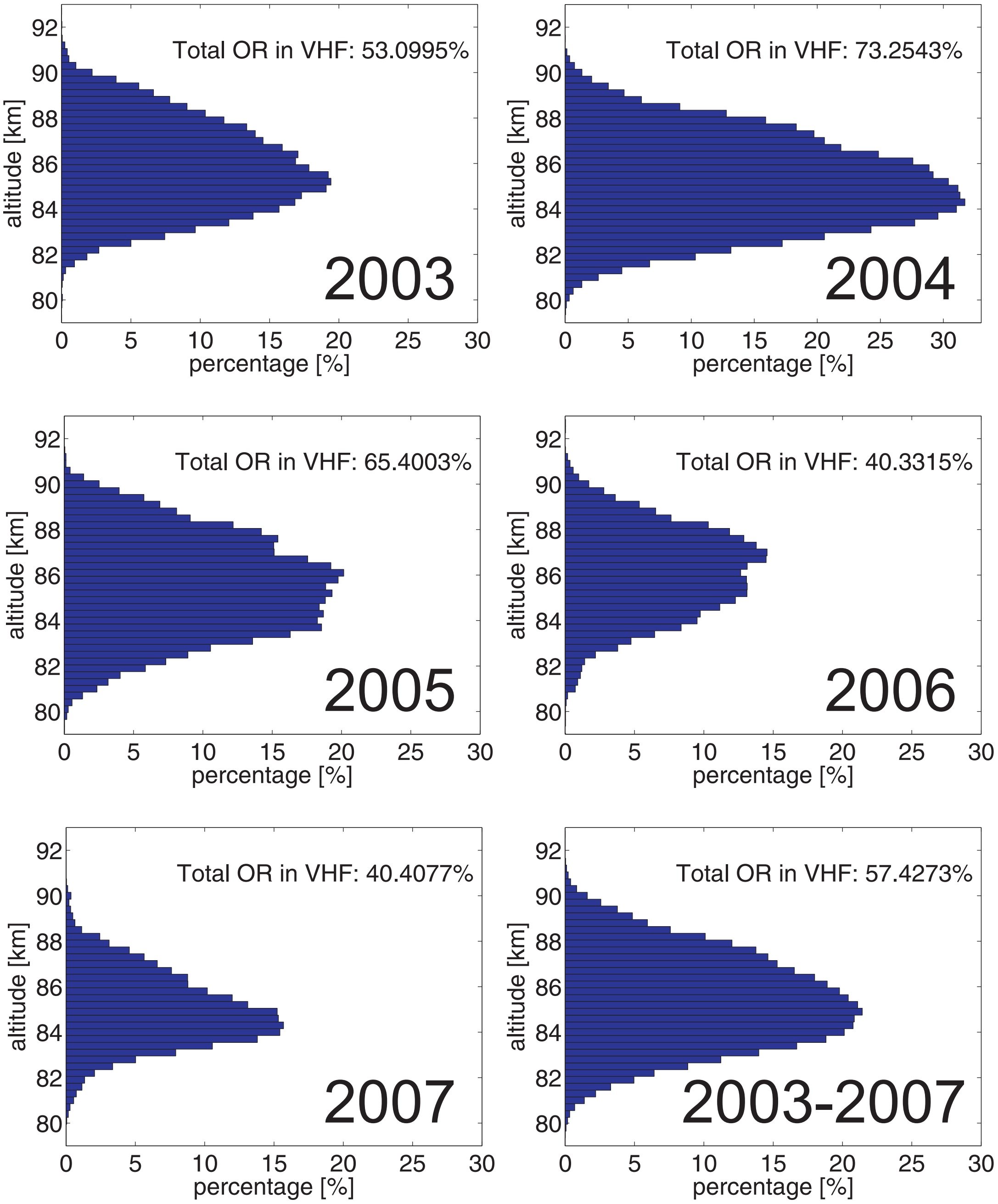

Figure 5.7: The occurrence rate of PMSE observed with the EISCAT VHF radar in different years from 2003 to 2007. The last panel (rightmost and lowermost) shows the statistical results for all the observations in these 5 years. The total occurrence rate, defined as PMSE occurred in at least one altitude channel, is indicated in the insert. The lengths of the observations in 2003–2007 are 124, 173, 65, 76 and 85 hours, respectively. During the five years, PMSE occurred at 224 MHz in the height range of 80–91 km and the maximum occurrence is 21% around 85 km.

a total of 523 hours of PMSE observations were carried out with the EISCAT VHF radar. Figure 5.11 gives an overview of the data coverage with respect to season and time of day. This reveals that taking all these observations together should allow us to derive reasonable

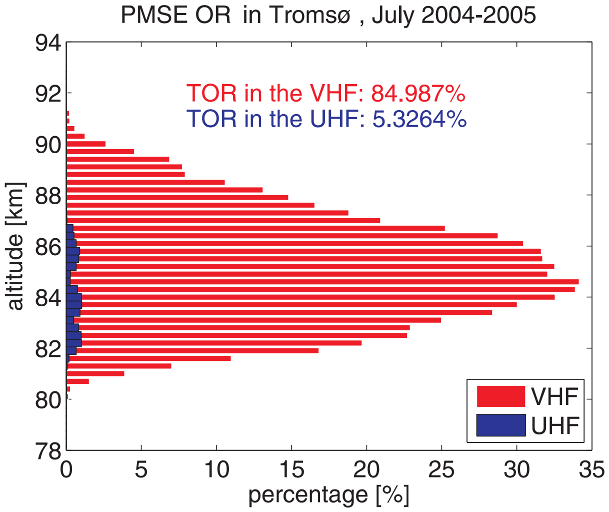

Figure 5.8: Comparison of PMSE occurrence rate at 930 MHz (in blue) and 224 MHz (in red) respectively derived from the EISCAT UHF and VHF observations in July 2004 and 2005. The total occurrence rates are indicated in the insert.

Table 5.1: η values (m^{-1}) derived at different years between 2003 and 2007

Year	2003	2004	2005	2006	2007
max	1.98e-014	1.35e-013	1.97e-014	1.05e-013	1.89e-013
mean	1.30e-016	2.60e-016	1.09e-016	3.45e-016	4.51e-016
median	2.21e-017	1.98e-017	1.32e-017	2.27e-017	2.13e-017
min	1.11e-018	1.01e-018	1.00e-018	1.04e-018	1.10e-018

estimates of both seasonal as well as diurnal variation patterns of PMSE at 224 MHz. Note that the statistics available to us represent a significant improvement over the only previous statistical study of PMSE at 224 MHz by *Palmer et al.* [1996] who only had ∼50 hours of VHF PMSE observations available (compared to the more than 523 hours used in this study). In contrast, however, Table A.4 shows that the same cannot be said regarding the UHF-observations, such that a statistical analysis of these measurements will for different years or months not yield meaningful results. Coming back to the VHF-data, Figure 5.11 shows that measurements in June and July are approximately evenly distributed among the different years from 2003 to 2007. Hence we will also tentatively investigate year-to-year variations based on these data, thereby keeping, however, always in mind that the statistics of year-to-year variations are comparably poor. Corresponding results are presented below.

5.3.1 Year-to-year variation

In Figure 5.12, we show the total occurrence rates of PMSE as seasonal mean values for the time interval from 1 June to 31 July. This shows that the occurrence rates of PMSE at 224 MHz reveal significant year-to-year variations. One of the intriguing questions regarding this year-to-year variation is whether this variability is mainly driven by the variability of mesospheric ice clouds or by the variability of other factors affecting PMSE like ionization.

In order to compare the occurrence rates of PMSE with the occurrence rates of NLC, we here reproduce the year-to-year variation of seasonal mean NLC occurrence rates as obtained

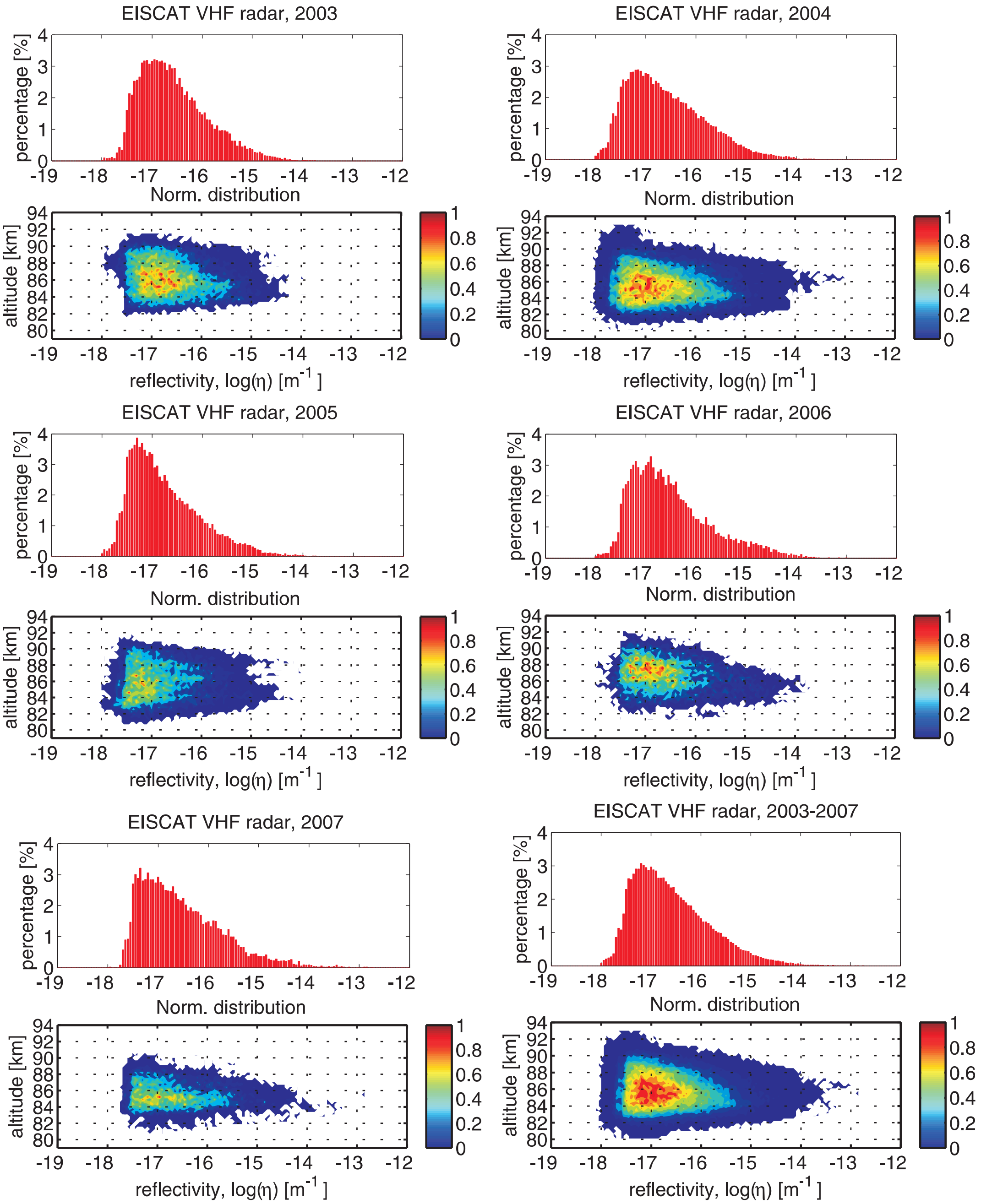

Figure 5.9: Relative occurrence of reflectivities (upper panels) and normalized distribution of the reflectivities along the altitudes (lower panels) obtained with EISCAT VHF radar (from left to right, from upper to lower) in different years from 2003 to 2007, respectively. The results derived from the sum of all the 5-year observations are shown in the last panel.

from observations with the ALOMAR RMR lidar at a horizontal distance of ∼130 km from Tromsø [*Fiedler et al.*, 2009]. Corresponding results have been overplotted in Figure 5.12 in red. The occurrence rates shown here represent the so-called long-term NLC-record at ALOMAR. This only includes clouds with a brightness in excess of the long-term detection limit of the ALOMAR RMR lidar (i.e., for backscattering coefficients $\beta > 4 \times 10^{-10}\mathrm{m}^{-1}\mathrm{sr}^{-1}$). It is striking that the occurrence rates of PMSE at 224 MHz show a similar year-to-year

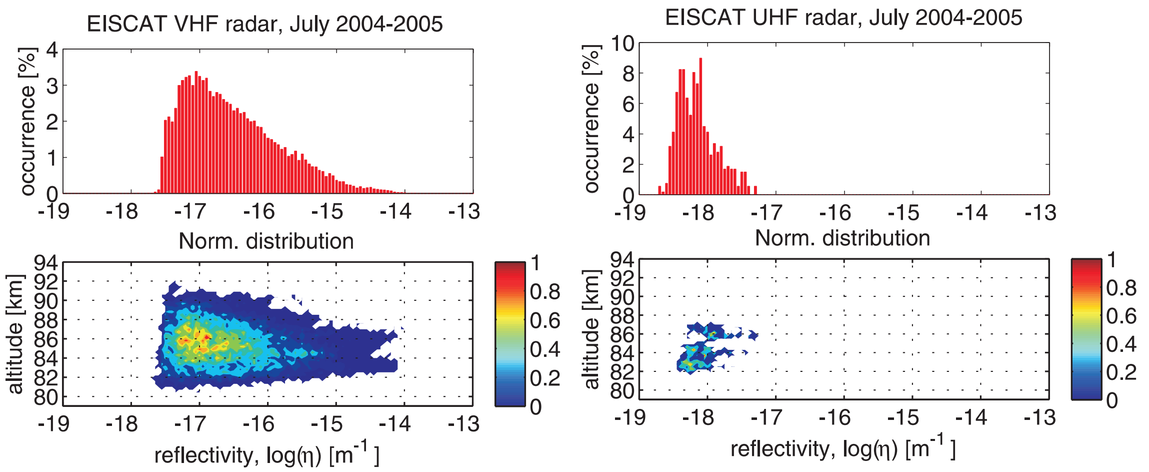

Figure 5.10: Relative occurrence of reflectivities (upper panels) and normalized distribution of the reflectivities along the altitudes (lower panels) obtained with EISCAT VHF radar (left panels) and EISCAT UHF radar (right panels) in July 2004 and 2005.

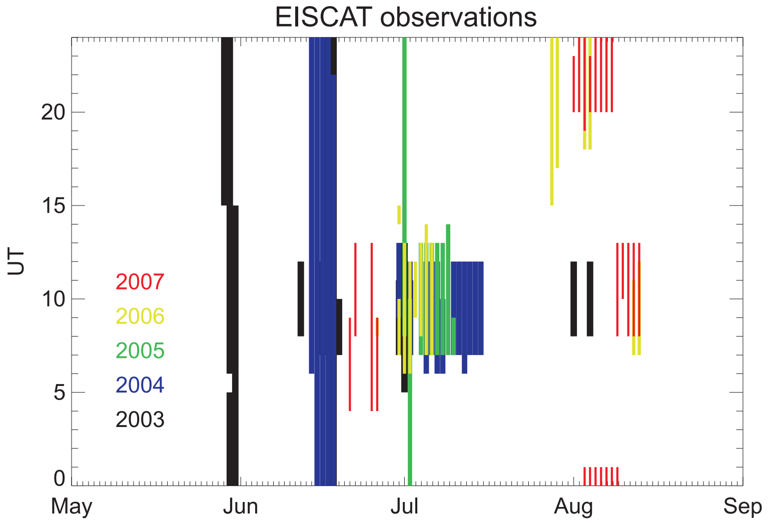

Figure 5.11: Distribution of observations during the years 2003–2007 against time (UT) and season. Large majority of them were carried out during local noon.

variation as the NLC. Furthermore, in order to study the relationship between NLC and PMSE at different frequencies, we reproduce the year-to-year variation of the occurrence rates of PMSE observed with the ALOMAR wind (ALWIN) radar (53.5 MHz) [*Bremer et al.*, 2009](see the black lines with triangles in Figure 5.12). Again, we use seasonal mean values for the time interval from 1 June to 31 July. Interestingly, the year-to-year variations of the occurrence rates of PMSE at 53.5 MHz are quite different from those at 224 MHz and hence are also quite different from the NLC occurrence rate.

We next consider the relation between the year-to-year variation of PMSE at 224 MHz and D-region ionization. The latter is mainly determined by solar radiation and high-energy particle precipitation. We make use of the solar Lyman α and geomagnetic Ap index to derive the dependence of PMSE on the solar activity and geomagnetic activity, since Ly-α is the dominant ionization source (ionization of NO) in ionospheric D region and Ap index is an indicator of the high-energy particle precipitation.

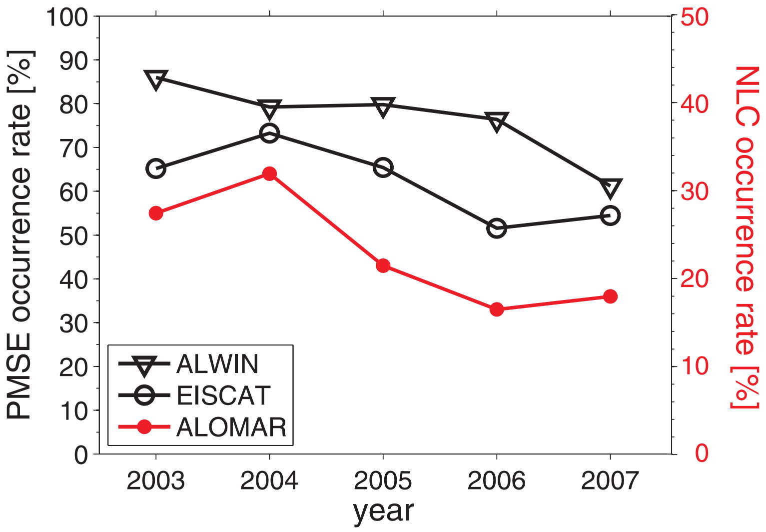

Figure 5.12: Comparison between PMSE occurrence rates (left ordinate) observed with ALWIN and EISCAT VHF radars and NLC occurrence rate (right ordinate) with ALOMAR RMR lidar in different years from 2003 to 2007.

In Figure 5.13, we show the correlations between the mean occurrence rate of PMSE and the solar Lyman α radiation (upper panel) and between PMSE and the geomagnetic Ap index (lower panel). Again, we restricted this analysis to data from June and July (8 values each, since there are no observations in June 2005 and July 2007). On the one hand this guarantees that the statistics are comparable for different years, and on the other hand this also makes sure that mesospheric temperatures are rather stable and do not have such large gradients as in May and in August. Both cases show a positive correlation, which indicates that the occurrence rate of PMSE at 224 MHz does increase with increasing ionization level. The deduced correlation of PMSE occurrence and Lyman α is less significant (88%) than with Ap index (93%). A similar analysis was recently reported by *Bremer et al.* [2009] for data obtained with the ALWIN radar at 53.5 MHz. Compared with the results of PMSE at 53.5 MHz, our observations show a less significant correlation between PMSE occurrence and the ionization level depending on Ly-α radiation and Ap index. The low level of significance for the correlation between the occurrence rates of PMSE at 224 MHz and the Ap index could partly be caused by the fact that the data set has poor statistics at local midnight (see upper panel of Figure 5.16), since it is thought that precipitating particles dominate the ionization level at midnight.

In summary, we find that PMSE at 224 MHz show a better match with NLC than PMSE at 53.5 MHz whereas the latter appear to show a stronger correlation with ionization. This may tentatively be interpreted as meaning that the properties (sizes) of ice particles play a more important role for PMSE at higher frequencies. Clearly, this point will require more attention in the future and should be reconsidered based on much larger and more homogeneous data sets than the one presented here.

5.3.2 Seasonal variation

The seasonal variation of PMSE occurrence rate is one of the striking features of PMSE [*Ecklund and Balsley*, 1981] and has been shown to be caused by the seasonal variation of the mesosphere temperature. I.e., PMSE occurrence maximizes when minimum temperature

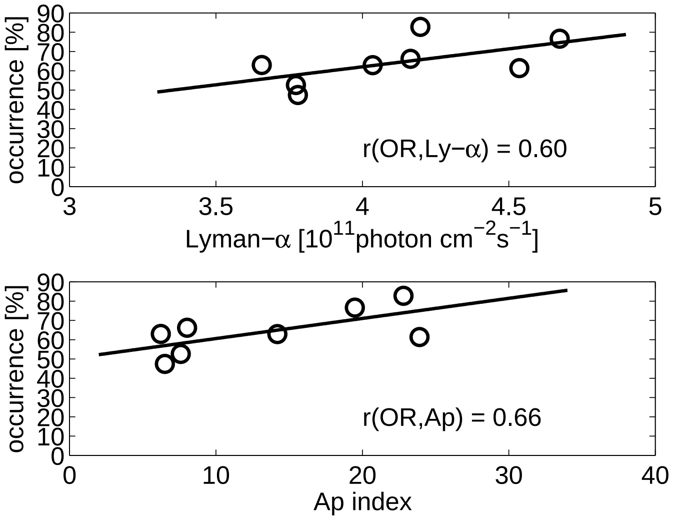

Figure 5.13: Correlation of PMSE occurrence rate with the solar Ly-α radiation (upper panel) and geomagnetic Ap index (lower panel). The correlation coefficients are indicated in the insert.

occurs and vice versa [e.g., *Lübken*, 1999; *Lübken et al.*, 2004]. In Figure 5.14, we present the numbers of the observations (white histograms) and PMSE events (black histograms) counted in 1 minute intervals (same in the remainder of this manuscript) in the upper panel, then the derived total occurrence rate for each day in red crosses (upper panel, see the right ordinate) and the seasonal variation of PMSE occurrence as a function of the altitude and the day of year in the lower panel. As mentioned before, the EISCAT radars were not run continuously. Even with 5 years of observations, there are still big gaps during the entire PMSE seasons. The seasonal variation of PMSE occurrence, however, is still very clear with larger occurrence rates during June and July and smaller ones in May and August. The occurrence rate can be even up to 100% during the main PMSE months and at selected altitudes. The seasonal variation was also considered for volume reflectivities (the resulting histogram and the normalized distribution at different months are shown in Figure 5.15). The maximum values of reflectivity in June and July are much larger than in May and August. Characteristic η values in different months between May and August are listed in Table 5.2.

Table 5.2: η values (m^{-1}) derived at different months

Month	May	June	July	August
max	1.42e-014	1.89e-013	1.05e-013	2.24e-014
mean	1.13e-016	3.14e-016	1.96e-016	8.43e-017
median	1.31e-017	1.84e-017	2.25e-017	1.54e-017
min	1.11e-018	1.01e-018	1.00e-018	1.07e-018

Let us focus again on the close correlation between PMSE and NLC. The existence of ice particles depends critically on the degree of saturation $S = p_{H_2O}/p_{sat}$, where p_{H_2O} is the partial pressure of water vapor and p_{sat} is the saturation pressure of water vapor over ice as given by *Murphy and Koop* [2005]:

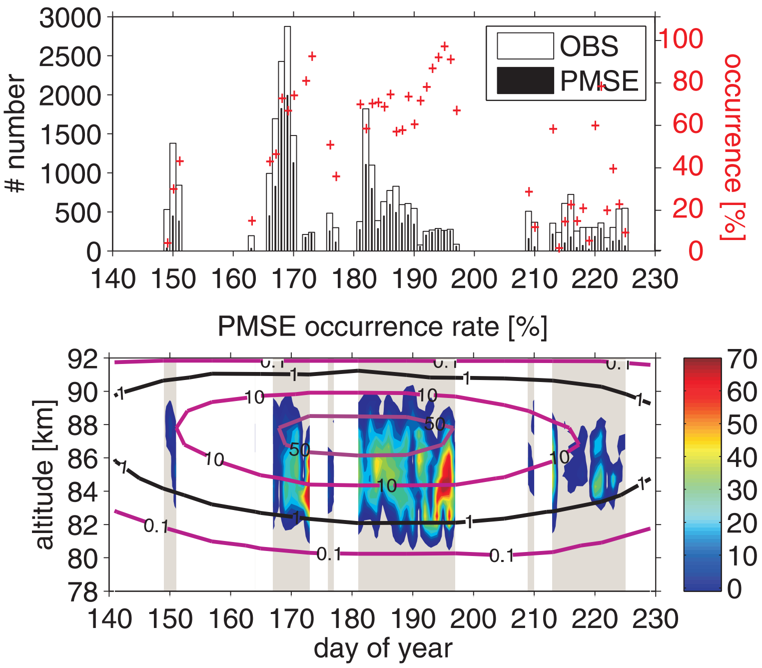

Figure 5.14: Upper panel: Seasonal variations of the PMSE occurrence rate observed with the EISCAT VHF radar from 2003 to 2007, the histograms of the observations (in white, 1-min interval) and PMSE events (in black) and hence the total occurrence rates for each day (see the right abcissa) are presented; Lower panel: PMSE occurrence as a function of the altitude and day of year as well as the degree of saturation S (contour lines with values) are presented. Note, in the lower panel blanks indicate there are no observations the grey shadings indicate the occurrence rates smaller than 1%.

$$p_{sat} = \exp\left(9.550426 - 5723.265/T + 3.53068\ln(T) - 0.00728332T\right) \tag{5.1}$$

where p_{sat} is in Pa (=N/m^2) and T is in Kelvin. The frost point temperature is defined as the temperature where $S = 1$. I.e., if $S > 1$ ice particles can exist and grow and if $S < 1$ they will evaporate.

In order to obtain S, we use data from the climatology of falling sphere (FS) temperatures and mass densities from *Lübken* [1999] (see his Tables 7 and 8), which were derived from a total of 89 falling sphere measurements performed in the summer seasons between 1987 and 1997. In addition, a seasonal mean and height-independent water vapor mixing ratio of 3 ppmv was used in our calculation for simplicity. The resulting S values are presented by the contour lines in the lower panel of Figure 5.14. The $S = 1$ line almost covers all the times and altitudes when PMSE were observed by the EISCAT VHF radar. Remaining differences can likely be attributed to our simplistic assumption of a fixed water vapor mixing ratio of 3 ppmv and the use of climatological temperatures and densities. That is, the FS temperatures and mass densities represent a mean atmospheric state (only 4 values for one month) and certainly do not contain potential contributions from gravity waves. The lower edge of the PMSE patches, which occasionally extend beyond $S = 1$, can most likely be attributed to the influence of gravity waves as well as tidal waves [e.g., *Hoffmann et al.*, 2005, 2008].

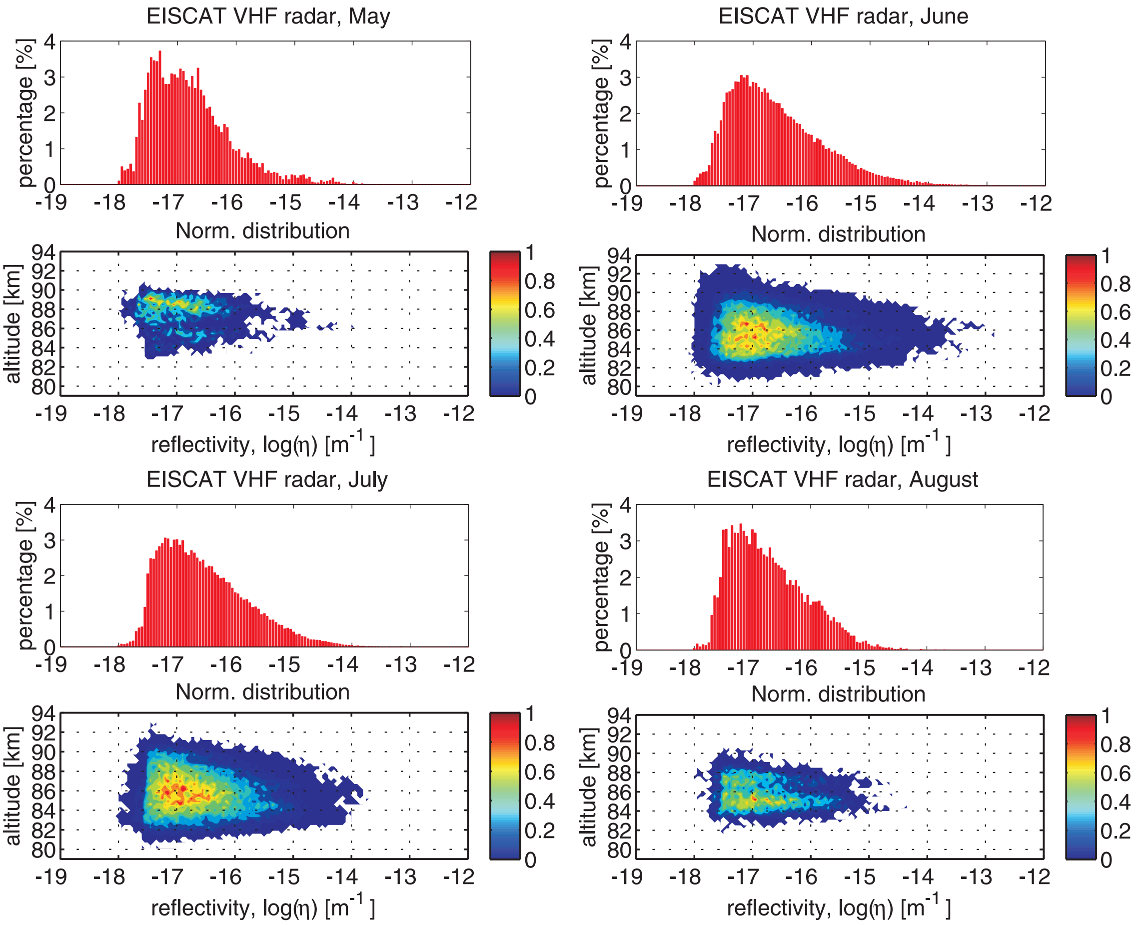

Figure 5.15: Occurrence of reflectivity obtained with EISCAT VHF radar at different months from 2003 to 2007 (upper panels) and normalized distribution of the reflectivity along the altitudes (lower panels).

5.3.3 Diurnal variation

As mentioned above, the 'arc-dlayer' experiments were normally carried out for several hours on one individual day. There are only several days when the measurements were run continuously for 24 hours (e.g., in 15–17 June 2004). The sum of all the observations, however, covers the complete 24 hours of an entire day, i.e., from 00:00–24:00. We thus are allowed to obtain the average diurnal variation of PMSE at 224 MHz.

Figure 5.16 shows the diurnal variation of both the total as well as altitude-resolved PMSE occurrence rates at 224 MHz with the number of the observations and the PMSE events. During the 5 years of observations, the PMSE measurements with the EISCAT VHF radar have been carried out mainly from 07:00–12:00 UT, i.e., around the local noon, and secondly mainly around local midnight. From Figure 5.16, we see that PMSE have been observed mainly within the height range of 83–88 km with a clear maximum during 10:00–12:00 UT around 85 km and a minimum during 19:00–22:00 UT. This is consistent with the PMSE observations by other nearby VHF radars [e.g., *Bremer et al.*, 1996a; *Hoffmann et al.*, 1999; *Klostermeyer*, 1999]. A second maximum was observed around 86 km during 00:00–01:00 UT. This second maximum normally appears near midnight or early morning, but it is not stable in time [*Hoffmann et al.*, 1997]. In addition, there is also a second minimum just at 04:00 UT, between the two patches of the maximum occurrence rates. Figure 5.17 presents the corresponding diurnal variations of maximum (upper panel) and median reflectivities (lower panel). These are in reasonable accord with the diurnal variations of the PMSE occurrence.

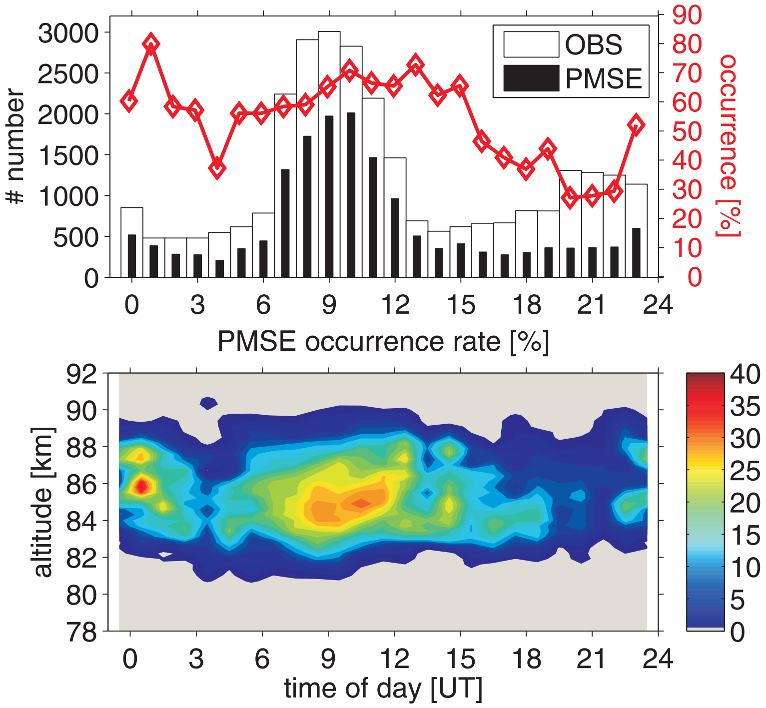

Figure 5.16: The diurnal pattern of the PMSE occurrence rate observed with the EISCAT VHF radar in the years between 2003 and 2007.

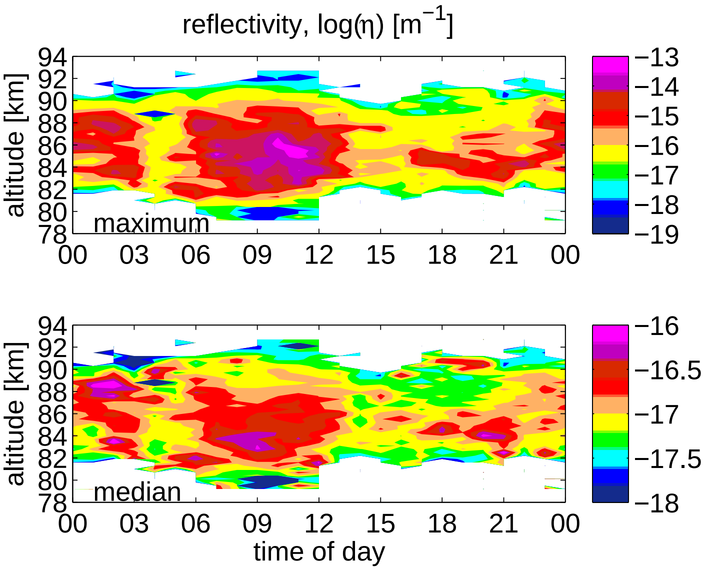

Figure 5.17: Diurnal variation of the maximum (upper panel) and median (lower panel) of volume reflectivities obtained with the EISCAT VHF radar in the years between 2003 and 2007.

We note that the here presented diurnal variations at 224 MHz are in full agreement with previous similar analysis at 53.5 MHz [e.g., *Hoffmann et al.*, 1999] for which it was shown that the diurnal pattern is caused by a superposition of temperature-variations owing to the semidiurnal tide as well as the diurnal variation of ionization caused by both solar Ly-α radiation as well as particle precipitation [*Klostermeyer*, 1999].

Chapter 6

Results: factors leading to UHF PMSE

6.1 Introduction

It has been mentioned above that most measurements of PMSE to date have been carried out at the 'standard' frequency of about 50 MHz. As for the case of measurements involving the radars operating at UHF range, one has to note that the reason for the poor statistics is indeed of geophysical origin since PMSE at such very large frequencies and small Bragg wavelengths are very weak. Hence only a handful of observations has been reported in the literature so far [e.g., *Turunen et al.*, 1988; *Collis et al.*, 1988; *Röttger et al.*, 1990; *Cho et al.*, 1992; *La Hoz et al.*, 2006; *Belova et al.*, 2007; *Rapp et al.*, 2008; *Nicolls et al.*, 2009]. From the comparison of the statistical properties of PMSE at different frequencies based on the simultaneous and common-volume observations, the occurrence of PMSE in the UHF range (e.g., 500 and 930 MHz) is much rarer compared to PMSE in the VHF range (e.g., 53.5 and 224 MHz). One obvious question is hence which factors lead to the occurrence of UHF PMSE. The theory with the largest acceptance in the community assumes that PMSE originate from turbulence-induced scatter in combination with a large Schmidt number caused by the presence of charged ice particles, which is termed the TWLS-theory of PMSE in this study (reader refers to *Rapp and Lübken* [2004]; *Rapp et al.* [2008]). According to this theory, the volume reflectivity of PMSE depends on the turbulence strength, the electron density, and the properties of the ice particles involved. Unfortunately, the information on the ice particles during our measurements was not available from independent observations. Hence in this section, a comparison between the factors affecting PMSE occurrence in the VHF and UHF range will be discussed based on the turbulence parameters and electron densities.

6.2 Turbulence parameters

It has been discussed in detail previously, for example, by *Hocking* [1983, 1985] that Doppler spectral width yields information regarding the velocity variance of the detected scatterers in the observing volume which is determined by turbulence, background wind, and atmospheric waves. The estimate of turbulent energy dissipation rate can hence be made from the spectral width of the Doppler spectrum observed in PMSE after correcting the influence of beam-, shear-, and wave-broadening [*Hocking*, 1985; *Nastrom and Eaton*, 1997]. Spectral width, here defined as the half power half width of the corresponding Doppler spectra assuming a Gaussian spectral shape, is proportional to the turbulent energy dissipation rate and, therefore, indicates turbulence strength [*Hocking*, 1985]. In this section, spectral width, an equivalent turbulence parameter, as well as turbulent energy dissipation rate, are derived from the Doppler spectrum in PMSE observations and comparisons between turbulence derived from PMSE observations at different frequencies are carried out.

6.2.1 Comparisons between the ESR and SSR

Before we proceed with the estimate of turbulence parameters, the spectral shape of the observed Doppler spectrum should be considered. It is common belief that coherent scatter due to the ordered structure generally caused by turbulence should reveal a Gaussian shape [e.g., *Woodman and Guillen*, 1974; *Röttger*, 1984; *Hocking*, 1985; *Strelnikova and Rapp*, 2010] whereas pure incoherent scatter due to the random motion of electron density has been well established to reveal a Lorentzian shape [e.g., *Dougherty and Farley*, 1963; *Tanenbaum*, 1968; *Beynon and Willianms*, 1978; *Rapp et al.*, 2007; *Strelnikova and Rapp*, 2010]. In order to quantitatively verify whether the spectra of PMSE signals are described by a Gaussian spectral shape, we can fit the magnitude of the corresponding auto-correlation functions (ACF, which according to the Wiener-Khinchine theorem are just the Fourier transforms of the power spectra) using the following empirical function introduced by *Jackel* [2000] and *Moorcroft* [2004]:

$$ACF(t) = ACF_{\tau=0} \cdot \exp\left(-(t/\tau)\right)^n \tag{6.1}$$

where t is the lag time at which the ACF is evaluated, τ is the decay time (which is inversely related to the spectral width), and n is an exponent describing the shape of the spectrum [e.g., *Rapp et al.*, 2007; *Strelnikova and Rapp*, 2010]. $n = 1$ corresponds to a Lorentzian spectrum as expected for pure incoherent scatter from the ionospheric D-region and $n = 2$ corresponds to a Gaussian spectrum.

In order to demonstrate the excellent quality of the Doppler spectra obtained from the ESR measurements we show a sequence of 4 min of such spectra at four consecutive range gates in Figure 6.1. Quite evidently, the spectra are reasonably well described by a Gaussian spectral shape. This was also verified quantitatively by fitting the magnitude of the corresponding ACF according to Equation 6.1 yielding an average n of 1.9, i.e., close to $n = 2$. This, in turn, implies that the measured signal originates from coherent structures and it is appropriate to make use of Gaussian function to characterize the spectra for this case. However, we also note that occasionally, some spectra appear to show multiple peaks that could actually be indicative of inhomogeneities within the radar beam which has been reported by previous studies [e.g., *Röttger and LaHoz*, 1990].

In Figure 6.2 we compare mean profiles (along with corresponding standard deviations) of spectral widths from observations with the SSR (black line with grey shading and red lines) and the ESR (blue line with error bars). First of all, we note that there is one common feature of all profiles, namely that the mean spectral widths increase with increasing altitude which is in agreement with many previous PMSE observations [e.g., *Czechowsky et al.*, 1988].

Besides this general agreement, however, we stress two additional points: when comparing SSR- and ESR-observations at times when both radars observed PMSE (blue and red lines), it is striking that the resulting profiles show on average larger values for the SSR below about 85 km while the values agree nicely above that altitude when the profiles show mean values of up to ∼3 m/s.

When comparing spectral widths from different radars with very different beam widths (see Table 4.3), one has to consider the fact that the observed spectral width σ_{obs} is actually the sum of different terms, i.e.,

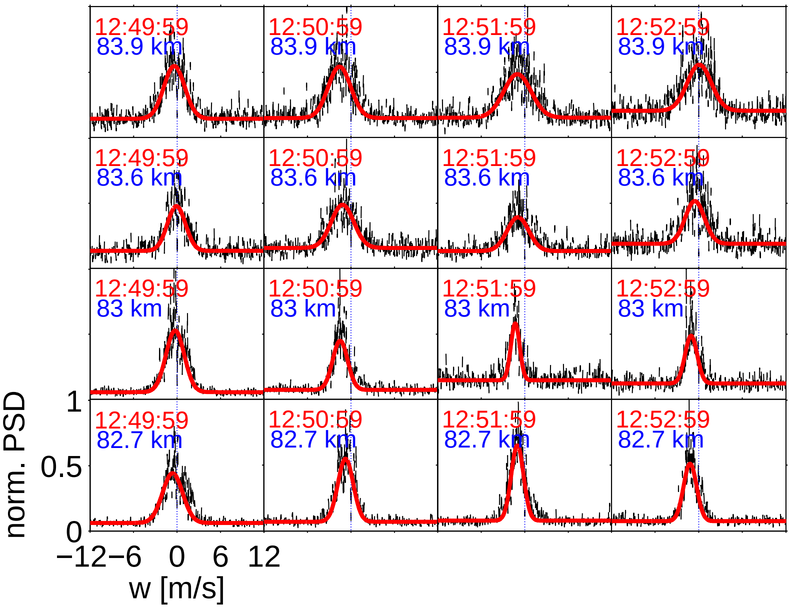

Figure 6.1: Normalized Doppler power spectra (PSD) from the ESR observations on 26 June 2006, for four different range gates and four consecutive minutes, all shown for a range of Doppler velocities (w) between -12 and 12 m/s.

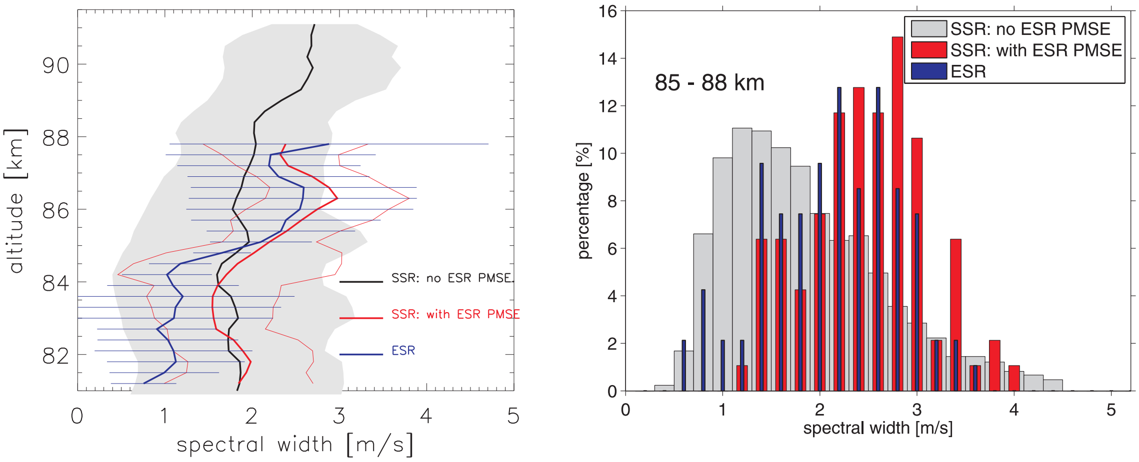

Figure 6.2: Left panel: Altitude profiles of the spectral widths (means and standard deviations) derived from SSR-observations at the times that the ESR was operated but did not detect PMSE (black line with grey shading), from SSR-observations at times when the ESR observed PMSE (thick and thin red lines), and from the ESR-observations (blue line with error bars). Right panel: Corresponding histograms of spectral widths from PMSE observations at 85–88 km altitude during times of ESR-operation (same color code as in Left panel).

$$\sigma_{obs}^2 = \sigma_{turb}^2 + \sigma_{beam}^2 + \sigma_{shear}^2 + \sigma_{wave}^2 \tag{6.2}$$

where σ_{turb} is the contribution from turbulent velocity fluctuations in the medium, σ_{beam}

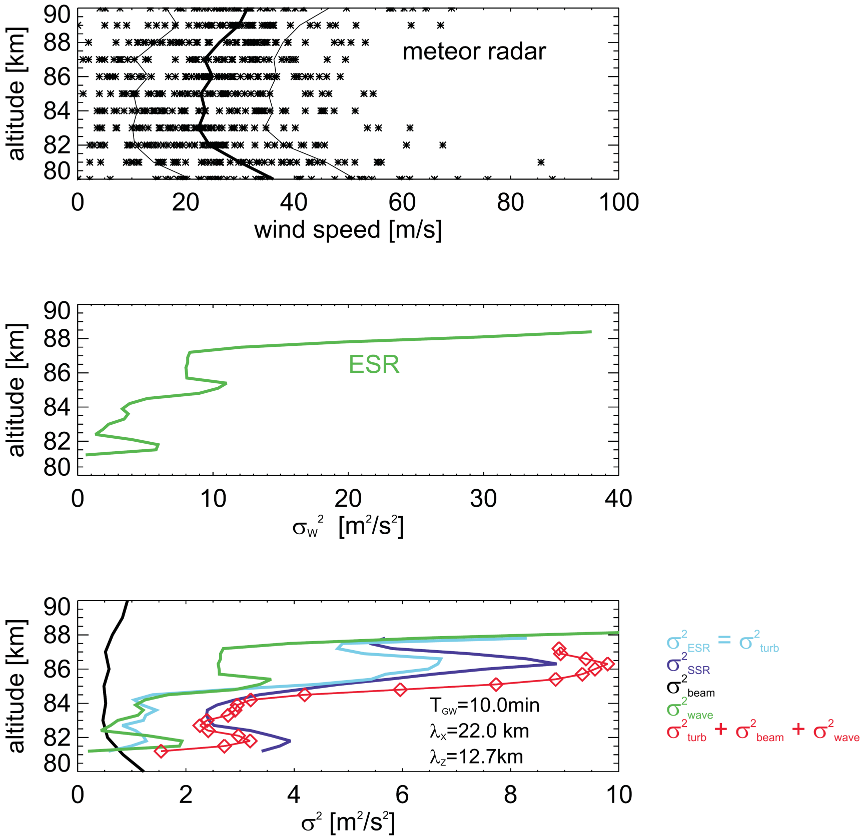

Figure 6.3: Upper panel: Wind speeds measured with the Nippon/Norway Svalbard Meteor Radar at the times of PMSE-observations with the ESR. Stars indicate individual data points whereas thick and thin black lines show corresponding profiles of mean wind speeds and corresponding standard deviations. Middle panel: Altitude profile of the variance of vertical winds derived from ESR-observations. Lower Panel: Altitude profiles of beam (black line) and wave broadening (green line) contributions to the spectral width recorded with the SSR. The light and dark blue lines show altitude profiles of σ^2_{ESR} and σ^2_{SSR}, respectively, and the red line shows the sum of $\sigma^2_{ESR} \approx \sigma^2_{turb}$, σ^2_{beam}, and σ^2_{wave}.

is the contribution from beam broadening, σ_{shear} is the contribution from shear broadening, and finally σ_{wave} is the contribution from high frequency gravity waves [*Hocking*, 1985; *Murphy et al.*, 1994; *Nastrom and Eaton*, 1997]. According to *Hocking* [1985], beam broadening may be quantified as $\sigma_{beam} = \frac{1}{2\sqrt{2}} \cdot \vartheta \cdot V$ where ϑ is the 3 dB full beam width of the transmitted radar beam (in radian) and V is the horizontal wind speed. Expressions for shear broadening may be found for example in *Nastrom and Eaton* [1997]. However, the latter is almost two orders of magnitude smaller than beam broadening for the vertical measurements considered here. Hence, shear broadening will not be considered any further. Finally, the broadening contribution owing to high frequency gravity waves was derived by *Nastrom and Eaton* [1997] and may be written as $\sigma^2_{wave} = \sigma^2_w \cdot f(Z, D, T, \omega_G, k, m)$. Here, σ^2_w is the observed variance of the vertical wind, Z and D are the depth and width of the observing volume at given height (i.e., 300 m and 7400 m at 85 km in the case of the SSR), T is the sampling time (i.e., 10 sec for the SSR), ω_G is the circular frequency of the high frequency gravity wave, and k and m are its horizontal and vertical wave numbers (see equations

A12–A15 in *Nastrom and Eaton* [1997] for more details).

In order to quantify σ_{beam}, we considered actual wind measurements with the collocated Nippon/Norway Svalbard Meteor 31-MHz Radar (NSMR). Details regarding this meteor radar system as well as corresponding scientific results can be found for example in *Hall et al.* [2002] and *Hall et al.* [2003]. The wind data are provided as half-hourly mean values only such that we did not attempt to correct individual spectral width observations with the ESR and SSR. Instead, we derived a mean profile of horizontal wind velocities during the times when the ESR observed PMSE. The latter is shown in the upper panel of Figure 6.3.

Further on, we considered whether or not high frequency gravity waves were present at the times of our PMSE observations and could have contributed to broadening the spectra. Indeed, it turns out that the times at which the ESR registered PMSE are characterized by the prevalent occurrence of gravity waves with typical periods of about 10 min. One typical example is presented in Figure 6.4 showing the vertical wind variation on 18 June 2006, as derived from PMSE observations with the ESR and SSR. From all such ESR observations we derived the variance of the vertical wind over the period of the PMSE observations. The latter is shown in the mid panel of Figure 6.3. In order to proceed further and estimate the broadening contribution owing to these high frequency waves, we further need information on the horizontal and vertical wavelengths. While these two parameters are not directly available from our observations, we may constrain reasonable estimates based on published climatologies of high frequency gravity waves as derived from airglow observations. *Nielsen et al.* [2009] have recently published a corresponding climatology for 76^o S and found prevalent periods of about 10 min as in our own observations with corresponding horizontal wavelengths of about 20 km. Importantly, these values are in reasonable agreement with several independent observations at other locations (see the overview of previous observations as summarized in Table 1 in *Hecht* [2004]). While this certainly does not prove that the waves present during our PMSE observations had exactly the same properties, we may still use a horizontal wavelength of about 20 km in order to estimate the order of magnitude effect of wave broadening on our own spectral observations. Finally, we used the dispersion relation for high frequency gravity waves (e.g., equation 30 in *Fritts and Alexander* [2003]) to derive a corresponding vertical wavelength.

The overall result of this exercise is presented in the lower panel of Figure 6.3. Here, we show the altitudes profiles of all relevant terms in Equation 6.2. Note that altitude profiles of σ^2_{beam} and σ^2_{wave} are only shown for the case of the SSR, since corresponding values for the ESR are minute and only make a negligible contribution to σ^2_{ESR}. Hence, we use the latter as our best estimate of σ^2_{turb}. Figure 6.3 reveals that the broadening contribution from wave broadening to the spectrum recorded with the SSR exceeds that one from beam broadening at basically all altitudes. Even more important, we see that the sum of $\sigma^2_{ESR} \approx \sigma^2_{turb}$, σ^2_{wave}, and σ^2_{beam} closely reproduces the altitude profile of σ^2_{SSR}. Hence, we tentatively conclude that the observed difference in ESR and SSR spectral widths below 85 km is likely caused by the combined effect of wave and beam broadening (with some remaining uncertainty caused by the need to estimate part of the wave parameters based on climatologies and not direct observations).

The other striking feature that we would like to stress here is the fact that spectral widths observed with the SSR in the presence of PMSE in the ESR are significantly larger at altitudes above 85 km as compared to the cases when PMSE was only observed by the SSR. This can be clearly seen in the right panel of Figure 6.2 in which histograms of spectral widths from altitudes of 85–88 km are compared for cases where PMSE was observed by the SSR only (in grey) and simultaneously by the SSR and ESR (red and blue). Since the histograms of the simultaneous ESR and SSR-measurements agree nicely indicating that the increased spectral

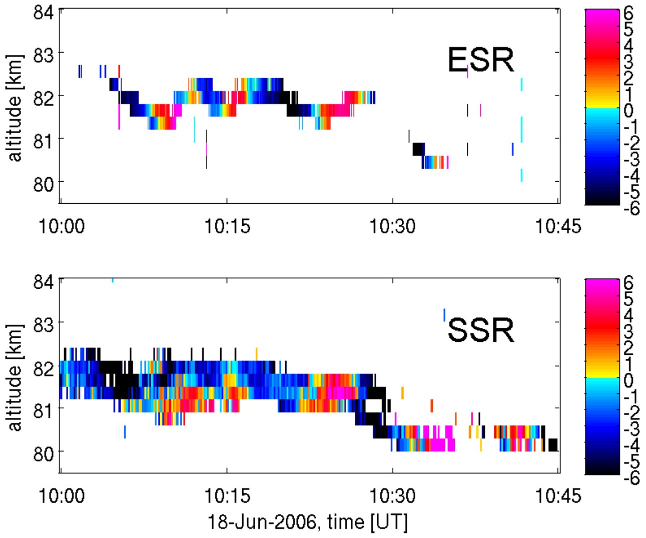

Figure 6.4: Upper panel: Height-time cross section of the vertical wind derived from Doppler spectra recorded in PMSE observed with the ESR on 18 June 2006. Lower panel: Same as upper panel but for the SSR.

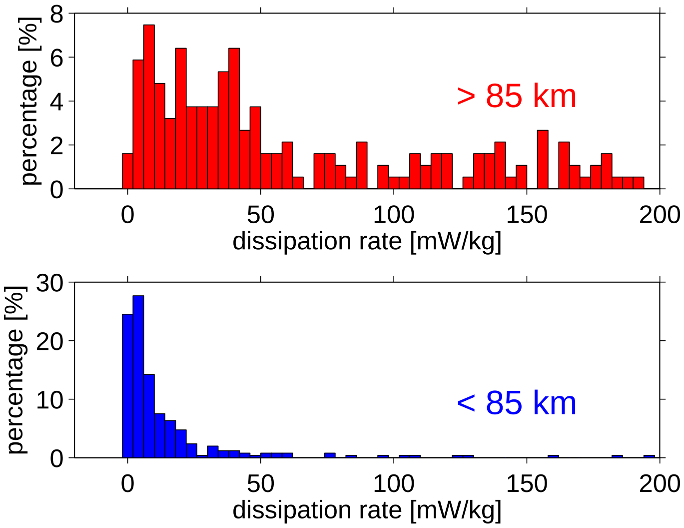

Figure 6.5: The distribution of turbulent energy dissipation rate at the PMSE altitude derived from the ESR observations during June 2006: (1) PMSE above 85 km in the upper panel; (2) PMSE below 85 km in the lower panel. These energy dissipation rates were derived from spectra with 1 min resolution, see text for details.

widths are due to an increased level of turbulent velocity fluctuations (and not increased broadening effects owing to large horizontal winds and/or high frequency gravity waves), this implies that the upper PMSE-layer observed with the ESR occurs in the presence of enhanced mesospheric turbulence.

Finally, we convert the observed spectral widths from the ESR - which are only marginally contaminated by artificial broadening effects (see above) - to turbulent energy dissipation rates following *Hocking* [1985] and *Röttger et al.* [1990]:

$$\epsilon = \frac{0.4\sigma^2 N}{2\ln 2} \tag{6.3}$$

where ϵ is the turbulent energy dissipation rate, λ is the wavelength of the radar (e.g., 0.6 m for the ESR), σ is the half power half width of the Doppler spectrum (in m/s) and N is the buoyancy frequency which we take from the MSIS-climatology [*Picone et al.*, 2002]. Note that we have chosen MSIS rather than a climatology based on actual observations on Svalbard since corresponding data sets either do not cover the relevant time of the year or the relevant height range [*Lübken and Müllemann*, 2003b; *Höffner and Lübken*, 2007]. Histograms of ϵ for altitudes below and above 85 km are presented in Figure 6.5. Importantly, the spectral resolution of the ESR-measurements (i.e., 0.167 Hz or 0.05 m/s) and the contribution to the spectral width by beam and wave broadening (i.e., 0.26 m/s on average) cause corresponding minimum detectable energy dissipation rates of significantly less than 1 mW/kg and hence do not significantly influence the here presented values. Figure 6.5 clearly shows that energy dissipation rates follow a very asymmetric distribution with a long tail towards large values as expected for intermittent processes like turbulence. Above 85 km most values fall into a range from 5–200 mW/kg whereas values are significantly smaller (5–50 mW/kg) below that altitude. We note that these values are in general agreement with the few independent estimates of turbulent energy dissipation rates based on direct rocket soundings during polar summer [*Lübken et al.*, 2002; *Strelnikov et al.*, 2006].

6.2.2 Comparisons between the EISCAT VHF and UHF radar

As mentioned above, the parameter n in Equation 6.1 describes the shape of the corresponding ACF. I.e., $n = 1$ and $n = 2$ correspond to Lorentzian and Gaussian shapes, respectively. Furthermore, if incoherent scatter in the D-region is modified by the presence of charged dust particles $n < 1$ is expected corresponding to a special shape assumed as a superposition of two Lorentzians, one depending on the diffusivity of ions and the other on charged heavy dust particles, hence indicating the presence of charged dust particles [*Rapp et al.*, 2007; *Strelnikova et al.*, 2007]. Under this theoretical frame, *Strelnikova and Rapp* [2010] carried out a statistical study from a total of 86 h of PMSE observations with the EISCAT VHF and UHF radar during the time period from 2003 to 2007. For the case of the VHF observations, the distribution of the derived parameter n peaks at 2 inside of PMSE layers whereas at 1 outside of PMSE layers (see Figure 6.6). Most importantly, when the UHF PMSE significantly exceeded the incoherent scatter signals the spectra revealed a clear Gaussian shape indicative of a coherent scattering process with identical spectral widths as VHF PMSE. This finding gives a strong support that PMSE at both frequencies originate from the same coherent scattering process (likely related to turbulence, see below).

We now proceed with the comparison of the spectral widths derived from the Gaussian-shape spectra of signals observed with both radars. Note that the experiment configurations and data acquisition systems of the EISCAT VHF and UHF radar are very similar and additionally the EISCAT VHF and UHF radar have very similar (and small) beam widths (see Table 4.1). Back to Equation 6.2, the contributions of beam broadening effects to the spectral widths are hence expected to be reduced (For the discussion on the broadening effects in detail, see *Strelnikova and Rapp* [2011]). In Figure 6.7 we show the distribution of the derived spectral widths from the simultaneous PMSE observations divided into a subset for the altitudes below 84 km and the altitudes above 84 km. First of all, the spectral widths derived at the two different frequencies compare well at all altitudes. In addition,

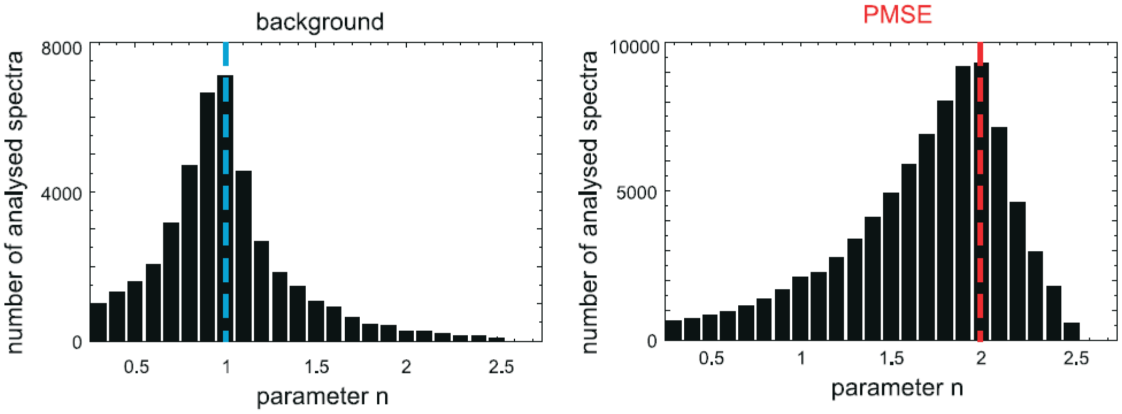

Figure 6.6: The statistics of parameter n derived from 86 hours of EISCAT VHF observations. Left panel: the distribution of n peaking at 1 outside of PMSE layers; Right panel: the distribution of n peaking at 2 inside of PMSE layers. This figure is reproduced from *Strelnikova and Rapp* [2010].

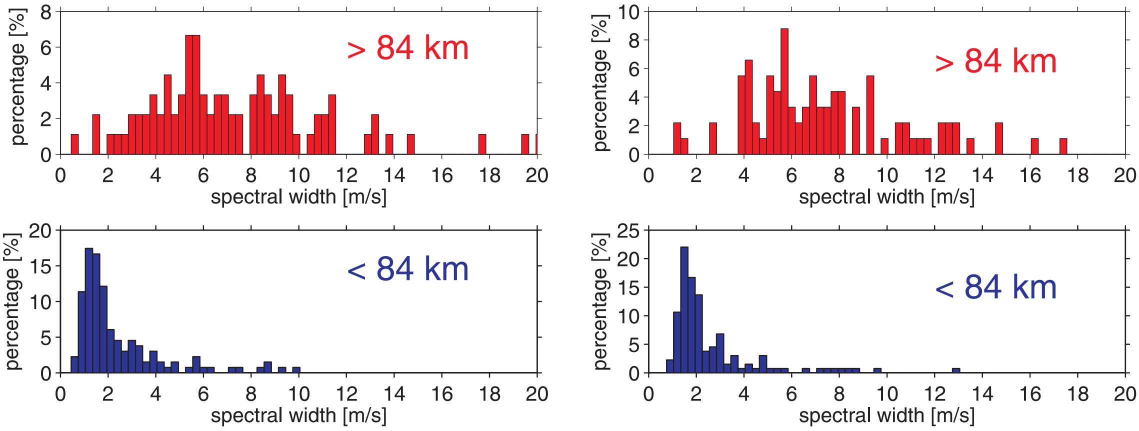

Figure 6.7: The distribution of spectral widths at the PMSE altitude derived from the PMSE observations with the EISCAT VHF (right panels) and UHF (left panels) radars in July 2004 and 2005: (1) PMSE above 84 km in the upper panels; (2) PMSE below 84 km in the lower panels. These spectral widths are in 1 min resolution, see text for details.

there are much larger values above 84 km than below 84 km for both radars. Most values fall into a range from ∼4 to 12 m/s above 84 km whereas from ∼0.5 to 6 m/s below 84 km which is comparable with the results by the ESR. In addition, Figure 6.8 shows the mean profiles (along with standard deviations) versus altitudes from the VHF observations during cases with and without UHF PMSE (red line with error bars and black line with grey circles) and from the UHF observations (blue lines), respectively. Roughly speaking the mean spectral widths increase with increasing altitude which is in agreement with many previous PMSE observations [e.g., *Czechowsky et al.*, 1988]. Besides that, we can see that the resulting profiles show almost the same values for both radars when they simultaneously observed PMSE. We note that this is in contrast to earlier findings by *Belova et al.* [2007] who presented a case study involving a few minutes of simultaneous PMSE observations with the EISCAT VHF and UHF radar and found that spectra recorded with the VHF radar were systematically larger than those recorded with the UHF radar. Our analysis - which is based on a significantly larger data set (more than 10 hours) - clearly does not reproduce this finding. We note that this finding has recently been corroborated by a more in-depth study by *Strelnikova and Rapp* [2011].

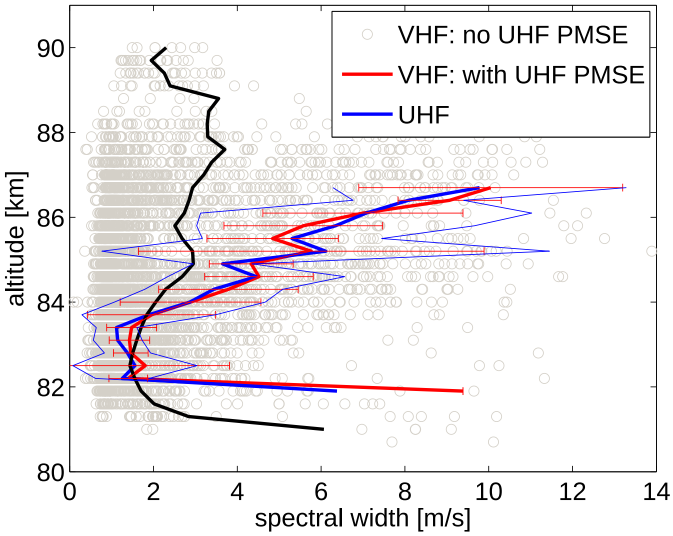

Figure 6.8: Altitude profiles of the spectral width (mean and standard deviations) deduced from the VHF observations at the times that the UHF radar was operated but did not detect PMSE (black line with grey circles), from the VHF observations at times when the UHF radar observed PMSE (red line with erro bars), and from the UHF observations (thick and thin blue lines).

Focusing again on the upper part of our data (say above ∼84 km), we see that the spectral widths are significantly smaller at times when only the EISCAT VHF radar observed PMSE compared with those when both radars observed PMSE. This implies that UHF PMSE require enhanced levels of atmospheric turbulence at these altitudes which is in full agreement with our similar analysis conducted for PMSE observations with the ESR (500 MHz) and the SSR (53.5 MHz) (see above).

6.3 Electron densities

As mentioned above, the EISCAT radars are incoherent scatter (IS) radars. The measurements are routinely analyzed in terms of electron number densities (or ‘apparent’ electron densities for the case of PMSE) by comparing measured power values to the measurements of a calibration source of known brightness temperature and by using IS theory. With observations by the EISCAT radars, we are hence able to compare the distribution of electron densities when VHF PMSE and UHF PMSE occurred. We note that there were unfortunately no electron densities available for the case of the ESR during our experiments. This issue is hence discussed only for the case of the EISCAT VHF and UHF radar.

For this exercise, we first present a case study. Figure 6.9 shows simultaneous observations with the EISCAT VHF and UHF radar on 5 July 2005. Again, the heating parts of the observations (20 sec for heater on and 160 sec for heater off, see Section 5 for details) were excluded from the dataset and the remaining observations were integrated over 1-min interval. Both radars observed pronounced echoes at altitudes between 83 and 84 km during a short time interval of 12:20–12:26 UT whereas the VHF-echoes extend over a larger altitude range and reveal more variations in the morphology.

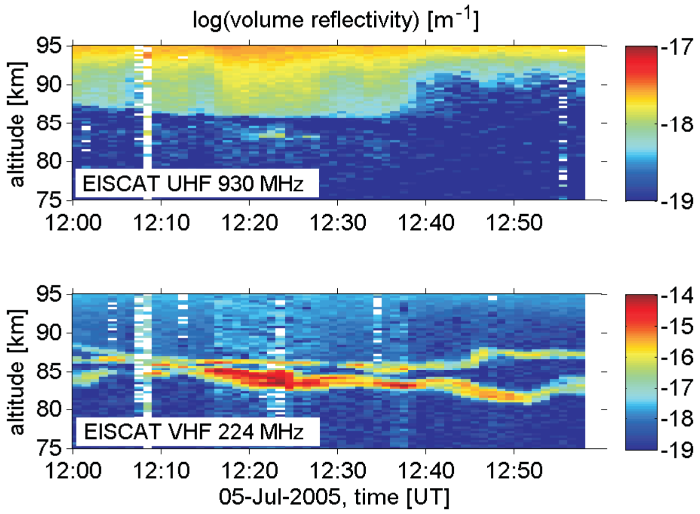

Figure 6.9: Height-time-intensity of radar echoes observed with the EISCAT VHF (bottom) and UHF (top) radars on 5 July 2005.

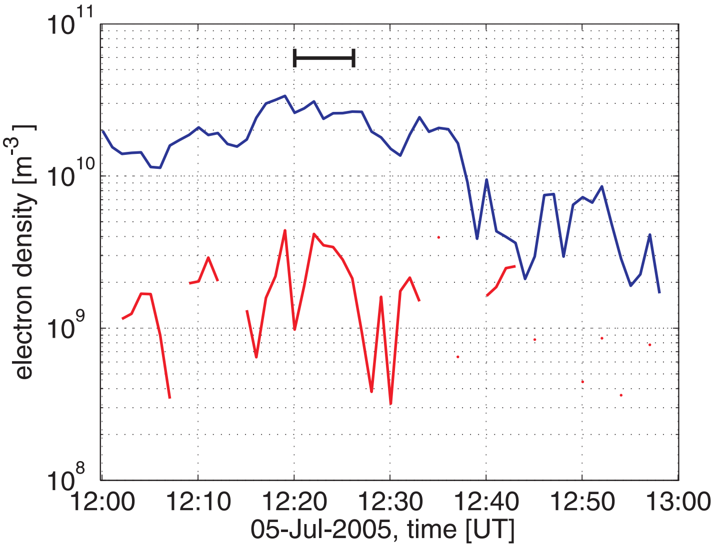

Figure 6.10: Electron densities from the UHF observations at 90 km (blue) and 80 km (red). Black bar indicates the time when both radars observed PMSE.

Since the observations with the EISCAT radars are a superposition of coherent scatter from PMSE and incoherent scatter from the ambient plasma at mesospheric altitudes, it is hence very difficult to isolate 'real' electron densities at the altitudes with PMSE. We hence derived the electron densities at altitudes of 80 and 90 km from the UHF observations (where no UHF PMSE occurred) as a reference. The results are presented in Figure 6.10. Roughly speaking the electron densities are relatively higher when both radars observed PMSE, i.e., during the time 12:20–12:26 indicated by black bar in comparison to the observation time of PMSE observed only with the EISCAT VHF radar.

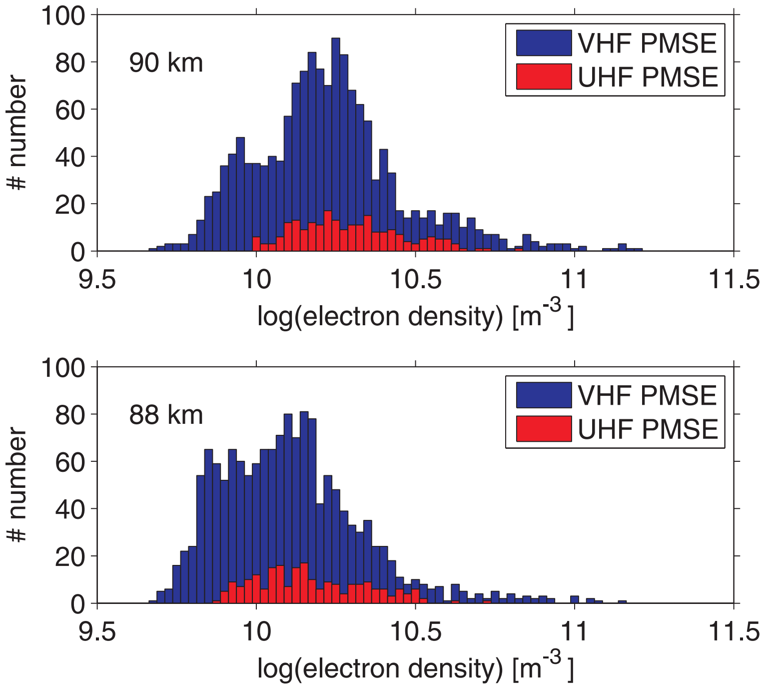

Figure 6.11: Distribution of electron densities at 90 km (upper panel) and at 88 km (lower panel) when VHF PMSE occurred (blue) and when UHF PMSE occurred (red).

We now turn to a statistical investigation based on the simultaneous observations with both radars in July 2004 and 2005. UHF PMSE were only observed in the altitude range between 81 and 87 such that the echoes with the EISCAT UHF radar above 87 km are only due to the incoherent scatter from the ambient plasma. Figure 6.11 shows the electron densities at 90 km (upper panel) and at 88 km (lower panel) when VHF PMSE (in blue) and UHF PMSE (in red) occurred, respectively. Both ensembles show a much bigger occurrence of VHF PMSE. Let us focus on the electron densities at 90 km. VHF PMSE occurred with the electron densities at 90 km as low as $5{\times}10^9$ m^{-3} whereas UHF PMSE only occurred when the electron densities at 90 km were larger than $1{\times}10^{10}$ m^{-3}. Importantly, a similar pattern (UHF PMSE only occur for larger electron densities) is also observed at 88 km, i.e., even closer to the PMSE layer. This provides a rough indication that the occurrence of UHF PMSE requires higher electron densities than VHF PMSE.

Chapter 7

Results: microphysical parameters derived from radar observations

It is common belief that PMSE are closely correlated with the existence of ice particles with nanometer size which form and grow at altitudes between ∼80 and 90 km due to the extra-ordinary thermal structure with mean minimum temperatures of ∼130 K attained at the mesopause above the summer polar regions [e.g., *Lübken*, 1999]. As of today, it was well confirmed that PMSE are closely related to the presence of ice particles. Proof for this close relation comes from a multitude of independent observations: i.e., temperature measurements within PMSE consistently show that the echoes occur in just the altitude range where the air is indeed supersaturated [*Lübken et al.*, 2002, 2004]. Furthermore, simultaneous and common volume observations of PMSE with radars and NLC by lidar have shown that PMSE exist in the entire altitude range between ∼80 and 92 km with NLC occurring at their lower edge [*Nussbaumer et al.*, 1996; *von Zahn and Bremer*, 1999; *Lübken et al.*, 2004; *Hervig et al.*, 2011]. Note that NLC have long been known to be direct evidence for ice particles with radii larger than 20 nm whereas particles can be as small as ∼2 nm to create PMSE [*Rapp and Lübken*, 2003]. In recent years, these high atmospheric ice clouds are of considerable scientific interest since it was suspected that the mesopause environment should change due to anthropogenic activity and solar forcing which in turn should give rise to changes in the properties of mesospheric ice clouds [e.g., *Roble and Dickinson*, 1989; *Thomas et al.*, 1989; *Garcia*, 1989]. One of the topics for the study of these ice clouds is to estimate the size of those ice particles existing near the mesopause region. Previous studies to estimate the ice particle radii have been carried out with lidar measurements at ALOMAR (Arctic Lidar Observatory for Middle Atmosphere Research) as well as satellite measurements, more sensitive, with SOFIE (Solar Occultation for Ice Experiment) onboard the AIM-satellite. The results with optical measurements are consistent with the model study with LIMA, i.e., LIMA/ice, by *Lübken et al.* [2009a] who gave the particle radii ranging 15-75 nm. However, an excellent way for a continuous monitoring of the mesopause region, including mesospheric ice clouds, involves radar measurements which are not hampered by tropospheric weather conditions (such as ground-based optical measurements) and which can give information with excellent time and altitude resolution. In the frame of the TWLS-theory of PMSE, we are now in the position to derive the radii of ice particles from the simultaneous observations of PMSE at two well separated frequencies. In this chapter, we first test the TWLS-theory of PMSE with simultaneous observations at different frequencies and apply this theory to the observations to derive the radii of ice particles involved (the corresponding results are presented).

7.1 Test of the TWLS-theory

The TWLS-theory of PMSE with the largest acceptance in the community assumes that PMSE originate from turbulence-induced scatter in combination with a large Schmidt number caused by the presence of the charged ice particles (see Chapter 3 for details). Following *Rapp et al.* [2008], the theoretical expression of the radar volume reflectivities in the viscous convective subrange of turbulence are given by:

$$
\begin{aligned}
\eta &= 8\pi^3 \cdot \frac{f_\alpha \cdot q \cdot Ri}{Pr^t} \cdot \frac{\sqrt{\epsilon\nu}}{N^2} \cdot \widetilde{M_e}^2 \cdot r_e^2 \cdot \frac{1}{k^3} \cdot \exp\left(-\frac{2\eta_K^2}{Sc} \cdot k^2\right) \\
&= C(\epsilon, n_e, N, H_n) \times \frac{1}{k^3} \cdot \exp\left(-\frac{2\eta_K^2}{Sc} \cdot k^2\right) \qquad (7.1)
\end{aligned}
$$

For all of the parameters in the above equation, reader refers to Chapter 3 or *Rapp et al.* [2008]. It is mentioned in Chapter 3 that the first experimental test of this theory was given by the same authors [*Rapp et al.*, 2008]. In this study, we further test this theory based on such large number of simultaneous observations derived with two collocated radars (i.e., the ESR/SSR and the EISCAT VHF/UHF radar) that reliable statement on the statistical behavior of this phenomenon can be made.

In any case, an excellent experimental possibility to test a potential theory is to perform PMSE observations at different frequencies and hence different spatial scales in the D-region plasma, i.e., the radar Bragg wavelengths (=half the radar wavelengths for monostatic radars). Before the exercise, we would like to mention that the absolute scattering cross section of PMSE (more typically expressed as the radar volume reflectivity which is the scattering cross section per unit volume) is independent of the radar system and configuration, different from other relative parameters, e.g., signal to noise ratio. Early studies were only carried out with one radar and derived volume reflectivities of PMSE at several data points, if not measuring PMSE with signal to noise ratio [e.g., *Röttger et al.*, 1990; *Hocking and Röttger*, 1997] whereas statistical studies of PMSE with calibrated radars derived the distribution of PMSE volume reflectivities with large dynamical ranges [*Latteck et al.*, 2008]. When surveying the literature, we note that the available experimental record impressively demonstrates that the absolute volume reflectivities of PMSE reveal an enormous frequency dependence such that simultaneous and common volume observations at more than one frequency should also be an ideal tool for studying the validity of theoretical expectations.

We now turn to a detailed comparison of volume reflectivities η observed at the two radar frequencies (and Bragg wavelengths). In an initial attempt we have tested whether there is any direct and obvious correlation between η at the two Bragg wavelengths of 2.8 and 30 cm. For this direct comparison, the measurements were put on an identical time-grid of 1 min. Subsequently, times and altitudes were identified during which PMSE occurred simultaneously in both radar observations. A scatter plot of corresponding reflectivities is presented in Figure 7.1. At first glance, there is no obvious correlation between the data.

The question, however, is what we may expect to find based on the above-mentioned PMSE theory according to which PMSE is caused by a combination of neutral air turbulence and an enhanced Schmidt number (reduced diffusivity) of electron density fluctuations (= fluctuations of the radio refractive index). For looking into this, we may go back to Equation 7.1.

In Figure 7.2 we have plotted various theoretical curves $\eta(k)$ for different combinations of the electron density and electron density gradient and the Schmidt number Sc. In addition, the two vertical bars indicate the Bragg wavenumbers of the SSR (k=2.24 m^{-1}) and the ESR (k=20.93 m^{-1}), respectively. Figure 7.2 shows two interesting things: if the Schmidt

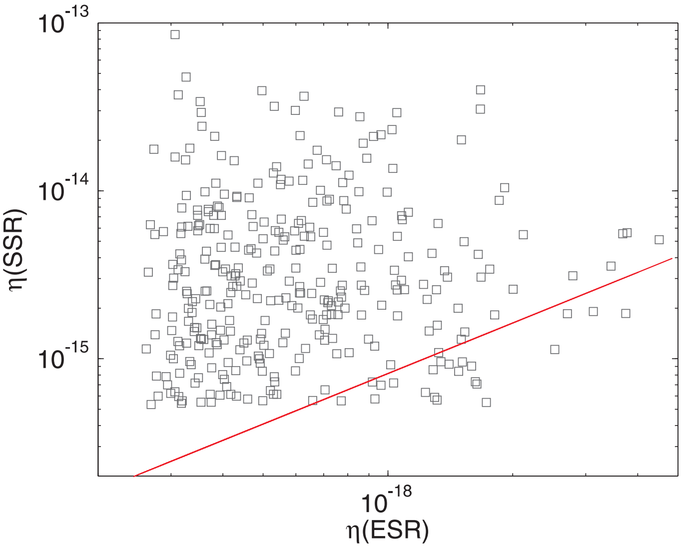

Figure 7.1: Scatter plot of the reflectivities of ESR and SSR for all simultaneous observations during June 2006. The red solid line indicates a reflectivity ratio of 816, i.e., all points where $\eta(\mathrm{SSR}) = (k_{ESR}/k_{SSR})^3 \cdot \eta(\mathrm{ESR})$.

number is large, then the ratio between η(SSR) and η(ESR) should be a constant value, i.e., the curves of $log(\eta(k))$ are parallel to each other. Going back to Equation 7.1 we see that in this case $\eta(k) \propto k^{-3}$, i.e., for large Sc both η-values fall into the viscous-convective subrange such that the ratio η(SSR)/η(ESR) is given by $(k_{ESR}/k_{SSR})^3$=(500 MHz/53.5 MHz)^3 = 816. If, however, the Schmidt number is not very large, then η(SSR) would fall into a part of $\eta(k)$ where the latter is dominated by the k^{-3}-dependence whereas η(ESR) would already fall into the part where $\eta(k)$ is dominated by the exponential term. In consequence, the ratio η(SSR)/η(ESR) should be larger than the minimum value of $(k_{ESR}/k_{SSR})^3$=(500 MHz/53.5 MHz)^3 = 816 in those cases (indicated by the red line in Figure 7.1).

In order to investigate this further, we next show histograms of the ratio η(SSR)/η(ESR) in Figure 7.3. This figure demonstrates that the ratios vary between ∼400 and 100000. Importantly, however, more than 94% are larger than a value of 816 (indicated with the red vertical bars), i.e., the ratio of the radar frequencies to the third power (see above). This means that the large majority of our data is consistent with the expectations based on the here considered theory. The remaining 6% which lie to the left of 816 can likely be explained by the uncertainty of the calibrations (see above) as well as by the fact that the radar volume of the ESR is significantly smaller (beam width 1.2°, see Table 4.3) than the radar volume of the SSR (beam width 5°, see Table 4.3). This means that an incomplete filling of the latter by scatterers will result in an underestimate of the 'real' volume reflectivity. Importantly, we can find independent support for this explanation by means of a similar analysis of PMSE-observations with the EISCAT VHF and UHF-radars in Tromsø (see Figure 7.4). From measurements conducted in the years 2004, 2005 and 2006 we could identify a total of 296 1-min samples of simultaneous PMSE-observations with these two radars operating at 224 MHz and 930 MHz (Bragg wavelengths of 67 cm and 16 cm, respectively). Importantly, unlike in the case of the SSR and ESR, the beam widths and hence observing volumes of these two radars are near identical such that one would expect to find an even larger percentage in agreement with theory - provided that the latter is correct. Indeed, this analysis yielded the result that 99% of derived volume reflectivity-ratios were larger than the corresponding

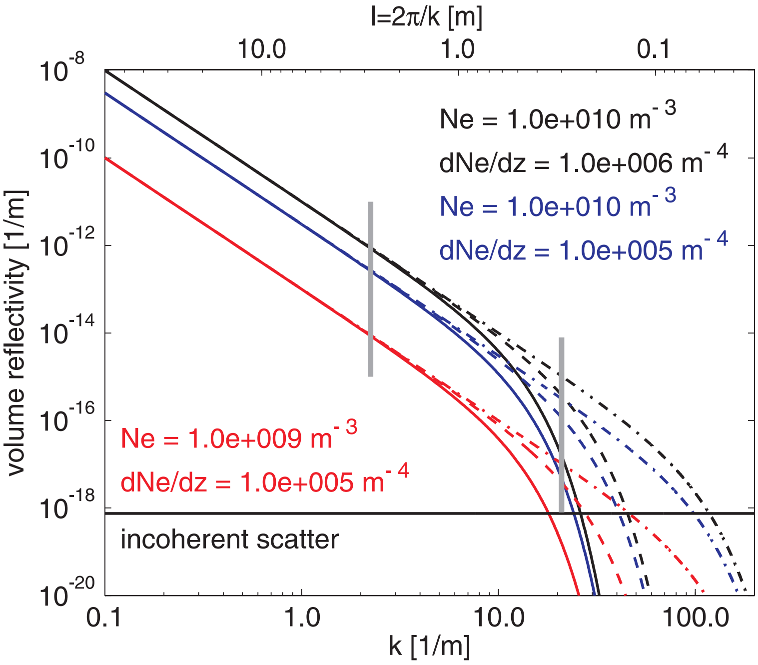

Figure 7.2: Calculated volume reflectivities for turbulent backscatter for a turbulent energy dissipation rate of 0.1 W/kg and electron number density ne and its gradient dne/dz indicated in the insert. The solid, dashed and dashed-dotted lines were calculated for Schmidt-numbers $Sc = 650$, 2600 and 41600, respectively (corresponding to radii $r_A = 10$, 20 and 80 nm, respectively). The two vertical bars indicate the Bragg wavelengths of the SSR (left) and the ESR (right). The black horizontal line indicates the volume reflectivity due to incoherent scatter for an electron density of 1×10^{10} m^{-3} for comparison.

ratio of the radar frequencies to the third power. We note, however, that we can certainly not exclude that some other, yet unidentified physical process, is responsible for the above described discrepancy for 6% of the presented data.

We note that the here demonstrated consistency between theoretical expectations and observations allows us to disregard any theory which predicts a wave number dependence which is less steep than k^{-3}. However, it certainly does not allow us to disregard other potential theories with functional dependencies steeper than k^{-3}. In order to distinguish such different possible functional dependencies, observations at more than two frequencies would be required. Hence, our analysis can certainly not prove that the assumed turbulence theory is correct. Nevertheless, we consider the consistency demonstrated above as sufficient motivation to proceed further and derive microphysical parameters from our data which may then be compared to independent observations in order to further corroborate or falsify our assumptions.

7.2 Microphysical parameters derived from radar measurements

In this section, we apply the TWLS-theory of PMSE to the simultaneous observations with two radars labeled 1 and 2 (here 1 represents for the SSR or the EISCAT VHF radar and 2 for the ESR or the EISCAT UHF radar) to derive the microphysical parameters in PMSE. From Equation 7.1 we see that the ratio of volume reflectivities observed with two radars

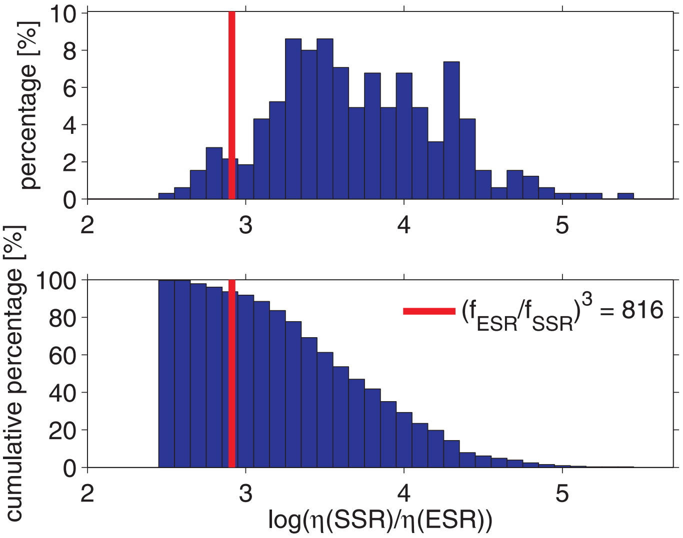

Figure 7.3: (top) Distribution of the ratio of the volume reflectivities observed with the SSR and ESR based on a total of ∼300 simultaneous and common volume observations with a integration of one minute each; (bottom) The same data shown as the cumulative percentage of the ratio, i.e., indicating which part of the observations showed a reflectivity ratio larger than the value indicated on the x-axis.

η_1/η_2 can be written as

$$\frac{\eta_1}{\eta_2} = \left(\frac{k_2}{k_1}\right)^3 \times \exp\left(-\frac{2\eta_k^2}{Sc} \cdot (k_1^2 - k_2^2)\right). \tag{7.2}$$

Note that this equation only contains two remaining unknowns, i.e., the Schmidt number Sc and the Kolmogorow-microscale $\eta_K = (\nu^3/\epsilon)^{1/4}$, while all other factors, partly largely uncertain, contributing to the expression for the volume reflectivity in Equation 7.1 have canceled. η_K can be easily calculated using the energy dissipation rates ϵ estimated from the spectral widths (from the observations with the ESR and the EISCAT VHF radar, respectively, see below) and an estimate of the kinematic viscosity ν using Sutherland's formula and densities and temperatures from the MSIS-climatology [*Picone et al.*, 2002]. As a result, we may solve Equation 7.2 for the Schmidt number Sc and obtain

$$Sc = \frac{2\eta_K^2(k_2^2 - k_1^2)}{\ln(\frac{\eta_1}{\eta_2} \cdot \frac{k_1^3}{k_2^3})}. \tag{7.3}$$

Taking further into account that the Schmidt number can be expressed in terms of the properties of the charged ice particles, corresponding ice particle radii can be derived from the following relation:

$$r_A = \sqrt{\frac{Sc}{6.5}} \tag{7.4}$$

where the radius r_A is in nm [*Cho et al.*, 1992; *Lübken et al.*, 1998; *Rapp and Lübken*, 2003]. Note that Equation 7.4 assumes that collisions between the ice particles and the neutral gas, and hence the corresponding diffusion, can be modeled as hard sphere collisions. The latter was shown to be a reasonable assumption for particle radii larger than ∼0.5 nm by *Cho et al.* [1992].

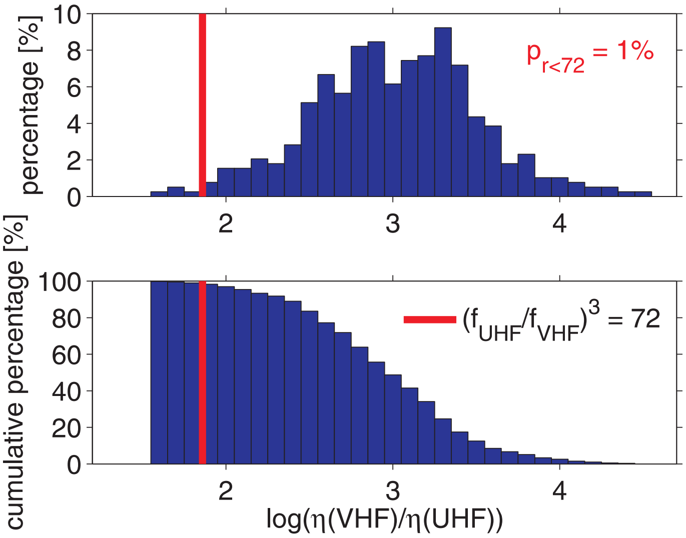

Figure 7.4: Same as Figure 7.3, but for the case of the EISCAT VHF and UHF radar based on 296 1-min samples of simultaneous PMSE observations.

7.2.1 Measurements with the ESR and SSR

We now proceed with all of the simultaneous measurements with the ESR and SSR for the derivation of Sc and r_A. In Equation 7.1 and 7.3, the radar 1 represents for the SSR and 2 for the ESR. This exercise results finally in histograms of the Schmidt number and ice particle radii shown in Figure 7.5. This figure shows that Schmidt numbers vary between a few hundred and ~32000 with corresponding radii between 10 and 70 nm. Interestingly, we note that the Schmidt-number distribution appears to show two distinct peaks. We will show below, that these two peaks correspond to different particle populations below and above ~85 km altitude.

Note that similarly large Schmidt numbers with maximum values of 4000 have recently been independently reported based on direct in situ observations of the spectral content of small scale fluctuations in the neutral gas and in charged particles under PMSE-conditions [*Strelnikov et al.*, 2009]. Importantly, independent observations on the same sounding rocket proved the presence of large ice particles [*Megner et al.*, 2009] and allowed to determine corresponding particle radii in the range of 20–30 nm [*Rapp et al.*, 2009], i.e., in good agreement with Equation 7.4.

In order to further assess the accuracy of the derived ice particle radii we have plotted contour lines of particle radii as a function of turbulent energy dissipation rates ϵ and ratios $\eta(\mathrm{SSR})/\eta(\mathrm{ESR})$ according to Equations 7.4 and 7.3 in Figure 7.6. In the same plot we have marked combinations of these two quantities derived from our simultaneous SSR and ESR PMSE observations. This comparison confirms that our measurements correspond to particle radii between ~10 and 70 nm. Furthermore, it also shows that this method to derive particle radii becomes more and more inaccurate as it approaches the theoretical lower limit of $\eta(\mathrm{SSR})/\eta(\mathrm{ESR})$ corresponding to the largest particle radii. The reason for this behavior can be easily understood by going back to Figure 7.2: As the ratio $\eta(\mathrm{SSR})/\eta(\mathrm{ESR})$ approaches its smallest possible theoretical value of 816, a further increase of the particle radius and hence the Schmidt number will hardly lead to any further change in $\eta(\mathrm{SSR})/\eta(\mathrm{ESR})$ because for large Schmidt number it is asymptotically given by ratio of the Bragg wave numbers to the

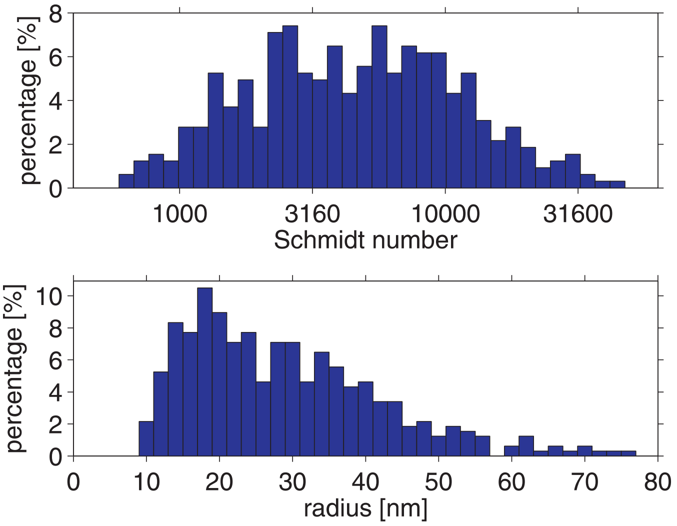

Figure 7.5: Schmidt numbers (upper panel) and radii of the charged particles (lower panel) derived from the ratios of the volume reflectivities between the SSR and ESR PMSE which occurred simultaneously for the observations in June 2006.

third power. As a next step, the lower panel of Figure 7.6 shows relative errors of the radii assuming relative errors in ϵ and $\eta(\mathrm{SSR})/\eta(\mathrm{ESR})$ of 10% and 50%, respectively. We note that the 10% error estimate for the accuracy of ϵ only reflects the uncertainty of deriving the spectral width from measured Doppler spectra and does not take into account possible systematic problems with Equation 6.5 as suggested on the basis of the direct numerical simulations presented by *Gibson-Wilde et al.* [2000]. These authors showed that for the case of a simulated Kelvin-Helmholtz instability ϵ derived on the basis of Equation 6.5 and using a constant background buoyancy frequency resulted in an underestimate of the real energy dissipation rate by a factor of five which would lead to a corresponding systematic shift of derived particle radii to smaller values. Whether or not this factor does apply to our observations is difficult to judge since no information is available to us about the type of instability which led to the observed turbulence events. Furthermore, we note that the only so far available direct comparison of ϵ-measurements based on the spectral width method with a well established in situ technique showed overall very good quantitative agreement [*Engler et al.*, 2005] such that our choice to only consider random errors and ignore potential systematic errors appears to be justified.

Note further that also other potential systematic effects like an incomplete filling of the radar beam in the case of the SSR, or a systematic overestimate or underestimate of the SSR antenna gain can not be excluded and would bias the results shown above to one direction. However, since we are so far incapable of quantifying these effects, they will not be considered any further.

In any case, using the above stated assumptions, the lower panel of Figure 7.6 reveals that derived particle radii have typical uncertainties of 30% and less except for those cases where $\eta(\mathrm{SSR})/\eta(\mathrm{ESR})$ is close to its theoretical lower limit as already mentioned above. We also note that smaller radii (< 20 nm) have even much smaller uncertainties of less than 15%.

Furthermore, we present full altitude profiles of ice particle radii for one given event together with the mean of all observations in Figure 7.7. These results demonstrate that both in a given event as well as in the statistical average, the radii show an increase with de-

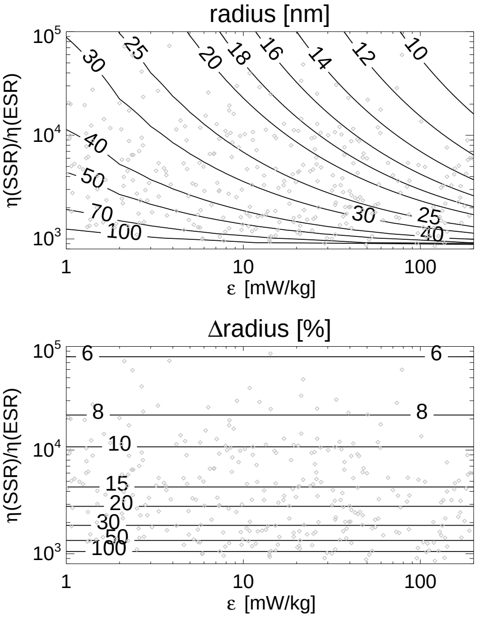

Figure 7.6: Upper Panel: Contour lines of particle radii (in nm) as a function of turbulent energy dissipation rates ϵ and ratios $\eta(\mathrm{SSR})/\eta(\mathrm{ESR})$ according to Equations 7.4 and 7.3. The grey symbols indicate combinations of these two quantities derived from the simultaneous SSR and ESR PMSE observations. Lower Panel: relative error (in percent) of the derived particle radius as a function of ϵ and $\eta(\mathrm{SSR})/\eta(\mathrm{ESR})$ assuming relative errors of 10% in ϵ and 50% in $\eta(\mathrm{SSR})/\eta(\mathrm{ESR})$. Again, grey symbols indicate combinations of ϵ and $\eta(\mathrm{SSR})/\eta(\mathrm{ESR})$ derived from the simultaneous SSR and ESR PMSE observations.

creasing altitude as suggested by independent observations [e.g., *von Savigny et al.*, 2005; *Hervig et al.*, 2009; *Rapp et al.*, 2009] and our current microphysical understanding [e.g., *Rapp and Thomas*, 2006].

7.2.2 Measurements with the EISCAT VHF and UHF radar

For the analysis of the simultaneous measurements with the EISCAT VHF and UHF radar, the radar 1 represents for the EISCAT VHF radar and 2 for the EISCAT UHF radar. Please note that the spectral widths involved for the estimate of energy dissipation rates and hence calculation of η_K can be derived from the VHF observations as well as the UHF observations. However, the VHF-widths and the UHF-widths given in m/s should be equal according to theory as well as to observational facts (see Figure 6.7) which has recently studied by *Strelnikova and Rapp* [2011]. We hence make use of the spectral widths from the VHF observations in the calculation of η_K.

We have analyzed a total of 76-hour simultaneous observations with the EISCAT VHF and UHF radar in July 2004 and 2005. The derived Schmidt number and corresponding ice particle radii are shown in histogram in Figure 7.8. Figure 7.8 shows that Schmidt numbers vary between ∼1000 and 20000 and the corresponding ice particle radii between ∼12 and 55 nm with only a few values larger than 55 nm. These results are consistent with the independent measurements with sounding rockets [*Strelnikov et al.*, 2009; *Rapp et al.*, 2009] as well as with optical instruments [*Baumgarten et al.*, 2008; *Hervig et al.*, 2009]. Furthermore, the comparison between Figure 7.5 and Figure 7.8 shows that the ice particle radii from the Tromsø radars fall within a narrower range in comparison to the Svalbard radars, i.e., radii

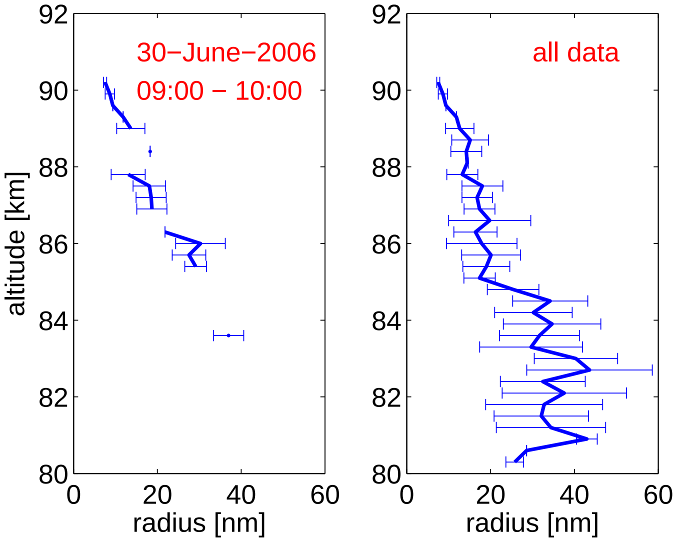

Figure 7.7: (left) Individual altitude profile of particle radii derived from PMSE observations on 30 June 2006 between 0900 and 1000 UT. (right) Average altitude profile of particle radii from the entire data set. In both plots, horizontal bars indicate the standard deviation of the radius values.

within 12–55 nm and 10–70 nm, respectively. This comparison hence presents two questions: (1) why the minimum value of radii from the Tromsø radars is larger; (2) why the maximum value of radii from the Tromsø radars is smaller. Note that when the UHF radar observed PMSE the VHF radar normally also observed PMSE according to theory and hence the time of the simultaneous PMSE depends on the UHF PMSE. It is the same scenario for the ESR and SSR. For Question (1), the difference can likely be explained by the different frequency of the ESR (500 MHz) from the EISCAT UHF radar (930 MHz), i.e., the Bragg scale of the latter is only half as small as the former. We may go back to Equation 7.1 and the simulation in Figure 7.2 and find that the occurrence of PMSE at 930 MHz is more difficult and requires larger Schmidt number and hence ice particles. Question (2), however, can be likely explained by the different latitude of Tromsø (69°N) from Svalbard (78°N). It is well confirmed that one of the general properties of PMSE is latitudinal variation: the PMSE occurrence rate drops from almost 100% at 78°N [*Lübken et al.*, 2004; *Zecha and Röttger*, 2009], $\sim$ 90% at 69^{o}N [*Bremer et al.*, 2003], to only $\sim$10–20% at 54°N [*Zecha et al.*, 2003]. This is consistent with 3D-model results of the thermal and dynamical structure of the mesosphere which suggests lower temperatures closer to the pole and hence a more favorable environment for the formation of ice particles [*von Zahn and Berger*, 2003; *Rapp and Lübken*, 2004]. Furthermore, the latitudinal variation of NLC particle sizes shows that ice particle radii tend to increase toward the pole [*Karlsson and Rapp*, 2006].

In Figure 7.9, we present full altitude profiles of ice particle radii for two given events. The simultaneous PMSE on 12 July 2004 occurred at a lower altitude range between $\sim$81.5 and 84.5 km in comparison to that on 13 July 2004 within a altitude range between $\sim$83.5 and 86.5 km. Importantly, these results demonstrate that the radii show an increase with decreasing altitude for both individual events as well as the combination of them. This is consistent with the results derived from the ESR and SSR and provides further supports to our understanding on the growth and sedimentation scenario of ice particles near the mesopause region.

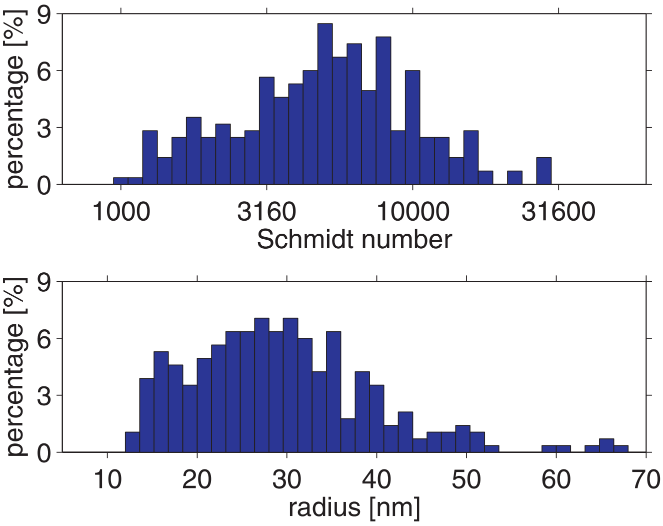

Figure 7.8: Schmidt numbers (upper panel) and radii of the charged particles (lower panel) derived from the ratio of the volume reflectivities of PMSE simultaneously observed by the EISCAT VHF and UHF radar, respectively, in July 2004 and 2005.

7.2.3 Comparison to SOFIE results

In order to further judge whether these distributions are geophysically reasonable or not we have finally compared our results to independent observations of ice particle radii in mesospheric ice clouds. A survey of available measurements quickly shows that there is currrently only one instrument which has sufficient sensitivity to detect ice particles with radii down to as small values as 10 nm. This is the Solar Occultation For Ice Experiment (SOFIE) onboard the Aeronomy of Ice in the Mesosphere (AIM) spacecraft [*Gordley et al.*, 2009]. SOFIE measures vertical profiles of limb path atmospheric transmission within 16 spectral bands between 0.29 and 5.32 μm wavelength. SOFIE observes about 15 sunsets in the Southern Hemisphere and 15 sunrises in the Northern Hemisphere each day. Measurement latitude coverage ranges from about 65° to 80° north or south. SOFIE measurements are used to retrieve extinctions of mesospheric ice clouds at eleven wavelengths from 0.33 to 5.01 μm. In addition to temperature and the abundance of gaseous species, mesospheric ice clouds are measured by monitoring the attenuation of solar radiation using broadband radiometers. The SOFIE field of view (FOV) is about 1.5 km vertical and about 4.3 km horizontal. Detectors are sampled at 20 Hz which corresponds to ~145 m vertical spacing. The sample volume length, as defined by the line-of-sight entrance and exit of a spherical shell with vertical thickness of the FOV, is ~290 km. Details of the method to derive microphysical parameters including effective radii (which are independent of the assumption of a specific particle size distribution) from SOFIE-observations have recently been presented in *Hervig et al.* [2009]. Here, we compare estimates of effective radii obtained during the entire northern summer season 2007 (data version V1.022) to our own results.

We also compare the radar results to observations with the ALOMAR Rayleigh/Mie/Raman (RMR) lidar located at 69°N from June 2006. The ALOMAR RMR lidar measures relative density profiles and particle (aerosol) properties in the stratosphere and mesosphere and has been described in detail by *von Zahn et al.* [2000]. A recent review of corresponding results including a detailed description of the method to derive ice particle parameters from observa-

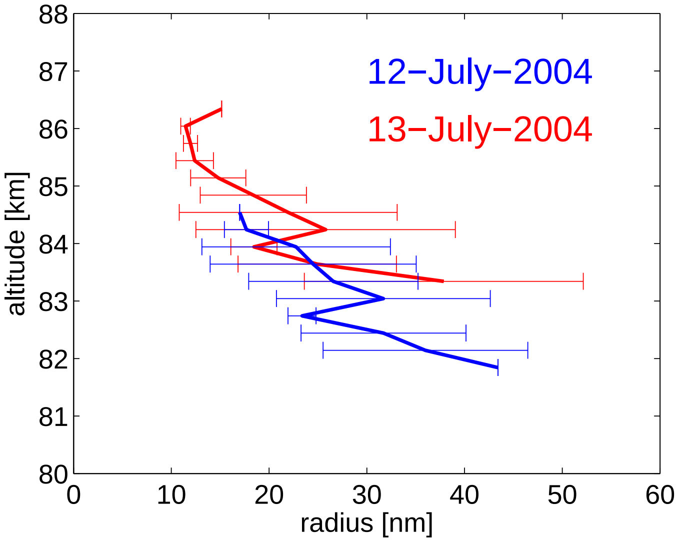

Figure 7.9: Altitude profiles of particle radii derived from PMSE observations on 12 July (blue) and 13 July (red) 2004 between 0700 and 1000 UT. Horizontal bars indicate the standard deviation of the radius values.

tions at three wavelengths is presented in *Baumgarten et al.* [2008]. For the current purpose, suitable 3-wavelength lidar data were integrated for 14 min and then analyzed for particle number densities, mean radii and widths of a Gaussian particle size distribution. For comparison to SOFIE and radar data, these parameters were then converted to effective radii as described in *Hervig et al.* [2009].

Before going into the details, a few caveats should be mentioned: first we note that we compare measurements from different years and also from different latitudes: while our radar measurements were done with the Svalbard radars in June 2006 as well as with the Tromsø radars in July 2004 and 2005, the AIM satellite was only launched on 25 April 2007 so that the 2007 summer season is the first available data set. Concerning latitudinal coverage, we note that the bulk of the SOFIE observations is from 68°N and the lidar observations are from 69°N which are very close to the Tromsø radars but not from 78°N as in the case of the Svalbard radars. Furthermore, SOFIE observations were taken between 22 and 23 LST and lidar data were gathered between 23 and 03 LST, whereas the radar observations were taken between 10–14 LST on Svalbard as well as between 09–13 LST in Tromsø such that potential tidal differences in particle properties might occur. Based on the multi-year lidar statistics of *Fiedler et al.* [2005] this effect is, however, expected to be small since both local time intervals correspond to comparable values in the observed semidiurnal variation of brightness values (see their Figure 3). Then one must realize that SOFIE observations are proportional to the cube of particle radius (i.e., absorption in the Rayleigh-regime) whereas the Schmidt number depends quadratically on the particle radius because a hard sphere collision model is here assumed. Finally, one must also note that there are certainly many occasions where PMSE (and hence mesospheric ice particles) were only observed with the SSR and not with the ESR. Hence, our data set of combined SSR/ESR-observations represents in itself a biased data set, i.e., it is not representative of an average state of the atmosphere but rather of a situation which allows PMSE to occur at the rather large frequency of 500 MHz. The conditions are compatible with the measurements with the EISCAT VHF and UHF radar. As described in detail above, these favorable conditions depend on the turbulence activity, the background ionization, and the size of the ice particles involved.

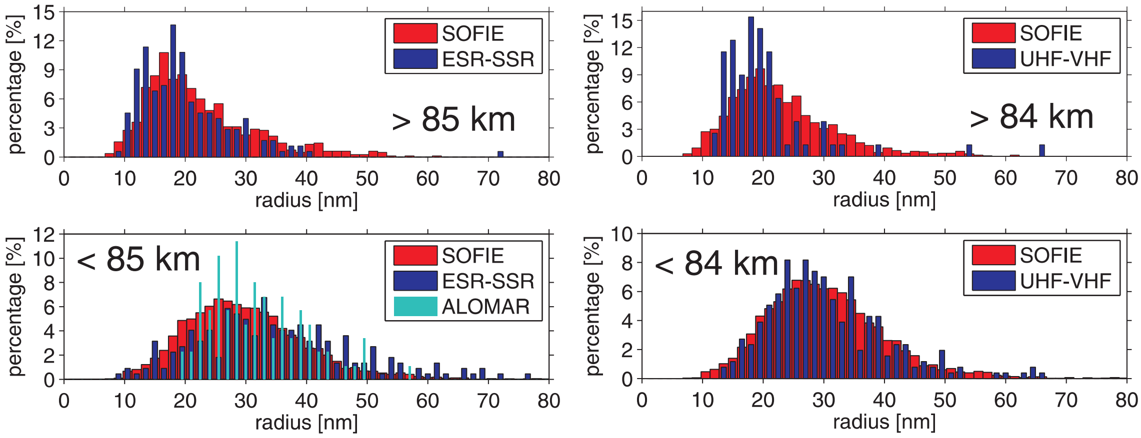

Figure 7.10: Distribution of ice particle radii derived from radar (dark blue) and optical observations from the SOFIE instrument on the AIM satellite (red) and from the ALOMAR RMR lidar (light blue) for altitudes (bottom) below and (top) above 85 km: (left) the results from the ESR and SSR; (right) the results from the EISCAT VHF and UHF radar. Please note the very different statistics of the different data sets: (left) below 85 km, histograms are based on 174 values for the radar, 88 for the lidar, and 6945 for SOFIE; above 85 km, there are 155 radar values, no lidar values, and 834 values from the SOFIE instrument; (right) there are 257 values for the radar and 5785 for SOFIE below 84 km whereas 78 radar values and 1397 SOFIE values above 84 km.

Having all these caveats in mind, we now compare radii derived from our radar observations to radii derived from the SOFIE occultations and ALOMAR RMR lidar observations at three wavelengths in Figure 7.10. For this comparison for the case of the ESR/SSR, we have divided the data again into a subset for altitudes from 81–85 km and from 85–88 km. Focusing first on the radar results, we see that radii above 85 km are on average significantly smaller (median value of ~20 nm) than below 85 km (median value of ~35 nm) which is in line with our current microphysical understanding of these ice clouds which assumes that the particles nucleate at the mesopause and then grow and sediment to lower altitudes [e.g., *Rapp and Thomas*, 2006]. Coming now to the comparison to the SOFIE-data, we note that the overall agreement between radar and optical measurements is actually very good: Above 85 km, the agreement is actually remarkably good with both data sets peaking at around 15 nm and showing a tail down to values of about 40 nm. Below 85 km, both satellite, radar, and lidar data show a rather broad distribution with median values of 28 nm in the case of the SOFIE measurements, 30 nm in the case of the lidar data, and 35 nm in the case of the radar observations, respectively. Taking into account the very different statistics of the three data sets (see caption of Figure 7.10) as well as the known fact that ice particle radii tend to increase towards the pole [*Karlsson and Rapp*, 2006] this difference can likely be explained by different latitudes at which radar (78°N) and satellite observations (68°N) were taken. Let us focus on the results with the EISCAT VHF and UHF radar. They are consistent with the results with the ESR and SSR, i.e., larger particles in the lower altitudes with a rather broad distribution. Furthermore, the results with the Tromsø radars actually show an even better agreement with the SOFIE values especially for the altitudes below 84 km (see Figure 7.10 (right)). This can likely be explained by the closer latitudes between SOFIE observations and Tromsø. However, the minimum value of radii with the Tromsø radars is somewhat larger than that of SOFIE results as well as of the ESR/SSR results (~10 nm). This has been explained above by the fact that the EISCAT UHF radar is operating at a very high frequency of 930 MHz and hence requires larger ice particle for PMSE to be observed. In summary, taking all the caveats mentioned above into account, we consider this an excellent agreement and very strong support that the radii retrieved from the radar observations are meaningful.

Finally, we present the mean profiles of resulting ice particle radii (along with the standard deviations) versus altitudes in Figure 7.11. Taking into account again the different statistics of the data sets and the different latitudes, we note the agreement between the altitude profiles of ice particle radii inferred from the radar observations and optical observations is actually very good. These results provide a general distribution of ice particle radii in the mesospheric clouds and certainly support our current microphysical understanding of the ice particles near the mesopause region [e.g., *Rapp and Thomas*, 2006].

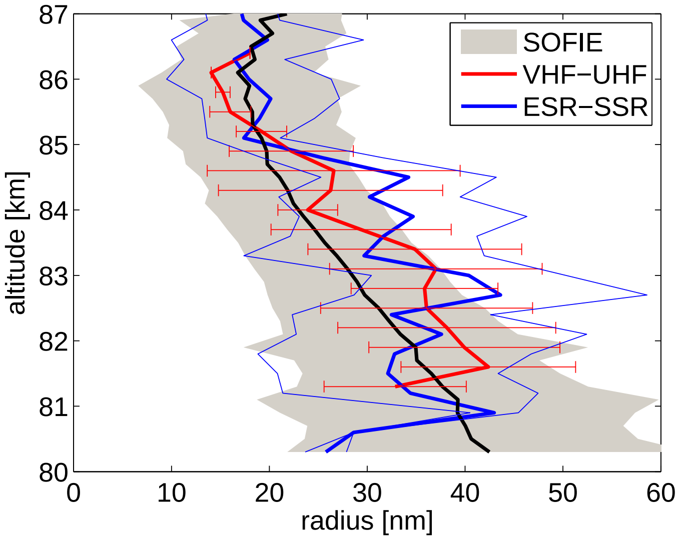

Figure 7.11: Altitude profiles of ice particle radii (mean and standard deviations) deduced from the radar observations with the EISCAT radars in Tromsø (red line with error bars) and Svalbard (blue lines) in comparison to independent optical observations with SOFIE onboard the AIM satellite (black line with grey shading). Both profiles inferred from radar observations as well as optical observations demonstrate that the radii of ice particles increase with decreasing altitudes.

7.3 Summary

In the frame of the TWLS-theory of PMSE the ratio of volume reflectivities at two Bragg wavelengths only depends on two unknown parameters, i.e., the turbulent energy dissipation rate and the Schmidt number which is itself a unique function of the radius of the charged ice particle leading to the required electron diffusivity reduction. Since turbulent energy dissipation rates can be derived from the spectral information of the ESR-measurements as well as the EISCAT VHF measurements, this ratio can be used to infer particle radii. Applying this method to our data sets we derive ice particle radii between 10–70 nm with typical uncertainties of less than 30% (up to 50% for the largest radii) for the results on Svalbard and 12–55 nm for the results in Tromsø. The comparison of our results to the independent measurements from the Solar Occultation For Ice Experiment (SOFIE) onboard the Aeronomy of Ice in the Mesosphere (AIM) spacecraft and the ALOMAR RMR lidar reveals an excellent agreement. The distributions of the ice particle radii at upper parts and lower parts of PMSE as well as the average altitude profiles of ice particle radii demonstrate that ice particle radii show an increase with decreasing altitudes. This is in full accord with expectations from microphysical models which predict particle nucleation close to the mesopause around 90 km and subsequent growth and sedimentation to lower altitudes.

Chapter 8

Results: electron densities in the presence of PMSE

8.1 Introduction

Strong depletion of electron densities (biteout) is one of the common properties of the PMSE environment at altitudes between ~80 and 90 km which is characterized by the fact that electron density is depleted as much as, typically, one order of magnitude below the undisturbed background. Such electron density depletion have long been observed from the measurements of electron densities by a Faraday rotation experiment with a sounding rocket which was launched during an auroral absorption event at 26 June 1966 in Andøya, Norway [*Pedersen et al.*, 1969]. After the discovery of PMSE, simultaneous and common-volume measurements of electron density with sounding rockets and PMSE with radars have been sporadically conducted (for the information of such campaigns, see Table 8.1). Electron density depletion was observed in almost all rocket borne electron density measurements in the vicinity of PMSE and also could be detected with the EISCAT UHF radar (incoherent scatter radar) [*Röttger and LaHoz*, 1990]. A typical example of electron density depletion from the STATE campaign in 1983 is reproduced in Figure 8.1 and shows that the electron densities were depleted by as much as a factor of ten to a value $\sim 5 \times 10^8$ m^{-3} in the altitude region where strong PMSE were observed with the Poker Flat VHF radar [*Ulwick et al.*, 1988].

It is common belief that mesospheric ice particles in the nanometer-scale range play a key role in the creation of PMSE. With the size exceeding ~20 nm, these ice particles are optically observed as NLC. At the PMSE altitude, they are already immersed in the plasma of ionospheric D-region and hence become charged due to electron attachment. This process results in the electron density depletion. Theoretical assumption by *Cho et al.* [1992] who applied the multipolar diffusion theory of *Hill* [1978] to a diffusion system consisting of electrons, positive ions and charged ice particles suggested that the ratio Λ between the charge number density of ice particle $N_A|Z_A|$ and the free electron density n_e should be larger than ~1 (1.2 for negatively charged particles and 0.6 for positively charged particles) for PMSE to occur. However, this assumption was later doubted by *Havnes et al.* [2001] who found that PMSE occurred in altitude regions where Λ was as small as 0.05 from simultaneous radar and rocket measurements of a PMSE event as well as by other authors [e.g., *Rapp et al.*, 2002]. Motivated by these previous findings, *Blix et al.* [2003] carried out a statistical study on the correlation between Λ and PMSE profiles based on 4 sounding rocket flights and derived Λ in the presence of PMSE. The results show only in 15% of all altitude bins with $\Lambda > 1$ whereas in ~75% of all altitude bins even with $\Lambda < 0.5$ (see Table 8.2 for details). *Rapp et al.* [2003b]

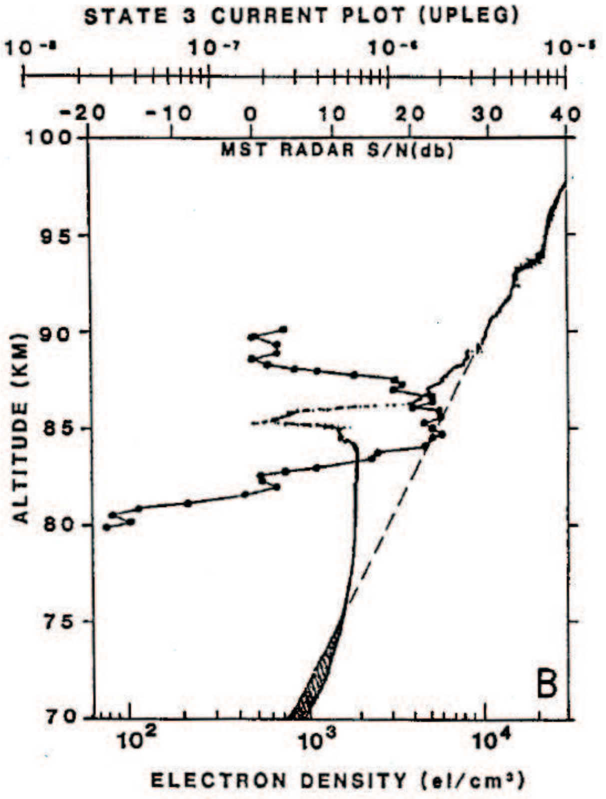

Figure 8.1: Height profiles of rocket borne direct current (DC) probe measurements of the electron density (solid line) and VHF radar echoes (solid line with dots) for the STATE-3 rocket flight conducted on 17 June 1983 from Poker Flat, Alaska. The dashed line illustrates a more typical D-region electron density. This figure is reproduced from *Ulwick et al.* [1988].

Table 8.1: Sounding rocket campaigns dedicated to the charge balance in the vicinity of PMSE

Campaign	Location	Date	Reference
STATE	Poker Flat, Alaska	Jun 1983	*Ulwick et al.* [1988]
MAC/SINE	Andøya, Norway	Jul 1987	*Inhester et al.* [1990]
NLC91	Kiruna, Sweden	Jul/Aug 1991	*Goldberg et al.* [1993]
SCALE/NLC93	Andøya, Norway	Jul/Aug 1993	*Blix* [1999]
ECHO	Andøya, Norway	Jul/Aug 1994	*Havnes et al.* [1996]
DROPPS/MIDAS	Andøya, Norway	Jul 1999	*Gordberg et al.* [2001]
			Rapp and Lübken [2003]
SOLSTICE	Andøya, Norway	Jun 2001	*Smiley et al.* [2003]
MIDAS/MaCWAVE	Andøya, Norway	Jul 2002	*Blix et al.* [2003]
			Croskey et al. [2004]
ROMA/Svalrak	Ny Alesund, Svalbard	Jul 2003	*Strelnikov et al.* [2006]
ECOMA/MASS	Andøya, Norway	Aug 2007	*Rapp et al.* [2009]
			Robertson et al. [2009]
ECOMA2008	Andøya, Norway	Jul 2008	*Friedrich et al.* [2009]

further showed that PMSE can exist in regions where only a minor fraction of free electrons are bound on aerosols, i.e., with no electron density depletion or $N_A|Z_A|/n_e \ll 1$, this condition compensated by large aerosol radius and hence proposed that the product $N_A|Z_A|r_A^2$ can be used as a microphysical proxy for PMSE yielding a good description of several relevant features of PMSE [*Hoffmann et al.*, 2005; *Raizada et al.*, 2007; *Lübken and Berger*, 2007]. The question how deep the electron density depletion is in general, however, is still open. In this chapter, it is our aim to derive Λ from the measurements of electron densities with the EISCAT UHF radar in the presence of PMSE simultaneously observed with the EISCAT VHF radar and compare Λ and the volume reflectivities of VHF PMSE.

Table 8.2: Λ values derived from the 4 rocket flights. This table is taken from *Blix et al.* [2003]

Campaign / Λ	0–0.5	0.5–1.0	1.0
SCT-06	70 %	5 %	25 %
ECT-02	80 %	5 %	15 %
ECT-12	100 %	0 %	0 %
SO-MI-05	55 %	25 %	20 %

8.2 Method to derive Λ from the radar observations

Electron density depletions in the vicinity of PMSE to date has been observed with the rocket-borne sensors [e.g., *Ulwick et al.*, 1988; *Inhester et al.*, 1990; *Blix et al.*, 2003; *Friedrich et al.*, 2009] (see Table 8.1) as well as with incoherent scatter radars in the UHF range [*Röttger et al.*, 1990]. The measurements analyzed here were simultaneously carried out in summer seasons from 2003 to 2007 with the EISCAT VHF and UHF radar (see Chapter 4 for details of these radars). All corresponding observations were conducted using the so-called 'arcdlayer'-experiment or its special version 'acdlayer_ht'-experiment (see *Li and Rapp* [2011] for detailed description of the experiments and data set). It is more specific that Table A.5 provides dates and times of the observations used for the present purpose.

Figure 8.2 sketches a typical altitude profile of electron densities (undisturbed electron density in dashed line and observed electron density in solid line) in a 'biteout' situation. From charge neutrality, we get $n_e = N_{e0} - N_A|Z_A|$, where N_{e0} is the undisturbed electron density in the absence of particles. The ratio between charge number density of ice particles and electron number density can then be determined by:

$$\Lambda = |Z_A|N_A/n_e = (N_{e0} - n_e)/n_e \tag{8.1}$$

Figure 8.3 presents three typical cases out of all the observations. The grey lines in each panel show 15 1-min electron density profiles deduced from the UHF observations with their mean profile as blue lines (i.e., n_e). In order to derive the undisturbed electron density, we fitted the mean profiles excluding the altitude range of the UHF PMSE signals and the electron density depletion by an 8th order polynomial. The fitting lines are shown as black dashed lines (i.e., N_{e0}). Based on equation 8.1, Λ-values were calculated and shown in the red lines with asterisk. The profiles of volume reflectivities of the simultaneous VHF PMSE were also overplotted as green lines. The comparisons between Λ and VHF PMSE reflectivities were used to infer the statistical distribution of Λ in the presence of VHF PMSE.

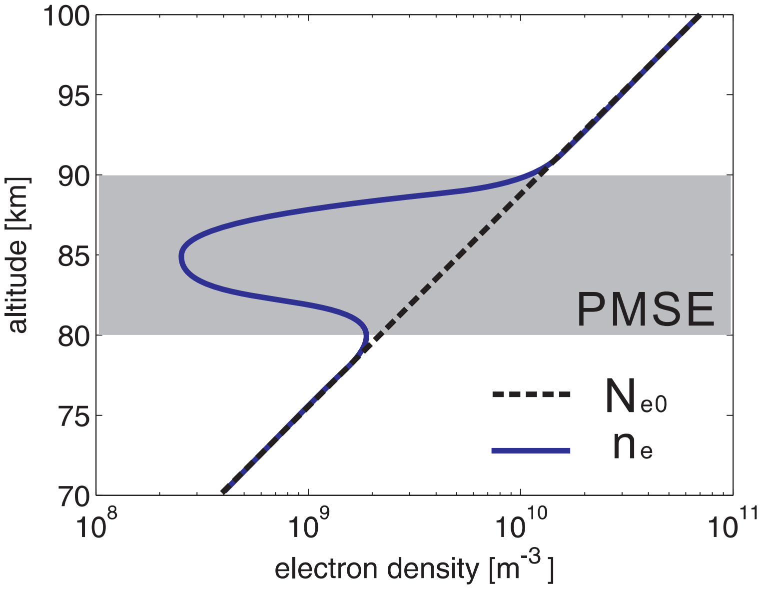

Figure 8.2: Schematic picture of typical altitude profiles of undisturbed electron density N_{e0} (in dotted line) and observed electron density n_e (in solid line) in a ‘biteout’ situation. The shaded area indicates the altitudes where PMSE occur.

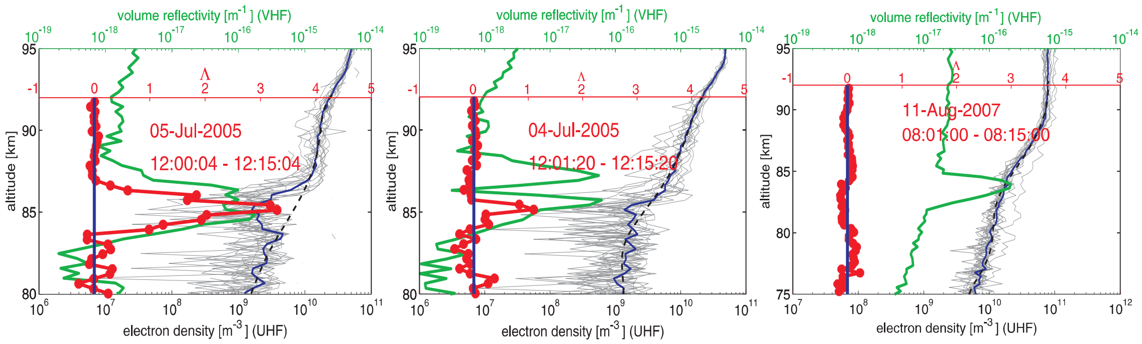

Figure 8.3: Samples of electron density depletion: strong depletion, weak depletion, no depletion in the left, middle and right panel, respectively. See text for the detailed description.

Before doing this exercise, we note that the EISCAT VHF and UHF radar are both incoherent scatter (IS) radars. The observations are hence a superposition of coherent scatter from PMSE and incoherent scatter from the ambient plasma at mesospheric altitudes. During our measurements, the EISCAT VHF radar observed very strong and long-duration PMSE whereas the UHF radar observed real electron densities in spite of scarce UHF PMSE. This is consistent with the expectation from the TWLS-theory of PMSE. With the simultaneous observations with both radars, we are hence able to derive electron densities from the UHF observations in the presence of the VHF PMSE. Due to the low ionization level, however, the electron densities are considerably low at the PMSE altitudes and could even be lower than the detection limit of the EISCAT radars resulting in biased observations. We hence scrupulously choose the data set with the electron density at the PMSE altitudes higher than $\sim 1\times 10^{-9}$m^{-3} which is normally considered as the detection limit of the EISCAT radars [e.g., *Strelnikova et al.*, 2009] (see Table A.5 for the list of observations here analyzed). In Figure 8.4, we show histograms of the measured electron densities derived from the UHF observations in a time resolution of 15 min (i.e., the profiles shown in Figure 8.3 in blue) in the presence of the VHF PMSE in the upper panel as well as the estimated electron densities by fitting the mean of the profiles excluding the altitudes range of the UHF PMSE and the electron density depletion by an 8th order polynomial (i.e., the profiles in Figure 8.3 in black) in the lower panel. Quite evidently, the large majority of electron densities are higher than $\sim 1\times10^{-9}\mathrm{m}^{-3}$, meaning that the observations could be considered as signal other than noise due to detection limit of the EISCAT radars.

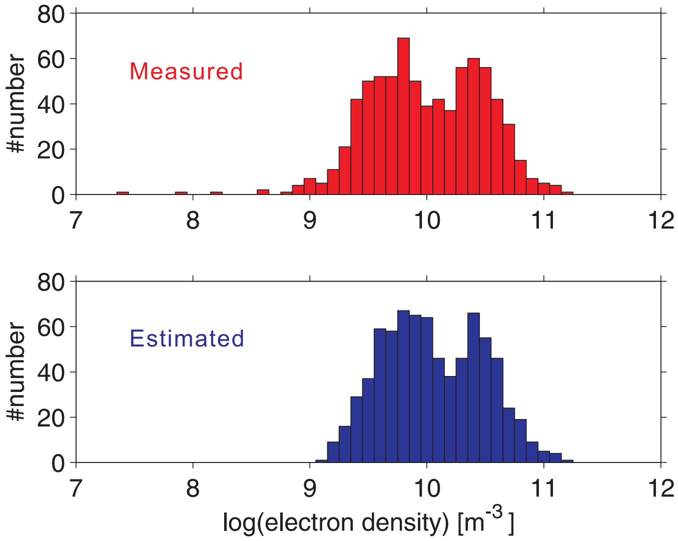

Figure 8.4: Histograms of measured electron densities derived from the UHF observations in the presence of the VHF PMSE (upper) as well as the estimated electron densities (lower). See text for details.

8.3 Statistical results of electron densities in the presence of PMSE

From 26-hour simultaneous observations, we derive 757 Λ values from the UHF observations in the presence of VHF PMSE (in 15-min interval). Figure 8.5 presents the distribution of the derived Λ (Λ against corresponding reflectivities of VHF PMSE in the upper panel as well as the histogram of Λ in the lower panel). For the large majority of cases (699 cases), the Λ values are within the range from -0.3 to 0.3 which can be considered close to 0 and hence no electron density depletion occurred. From 757 cases, there are only 33 cases with $\Lambda > 0.5$ indicated with red plus in the upper panel (21 cases with $\Lambda > 1$), i.e. only 4.4% of all the observations with $\Lambda > 0.5$. Different from in situ measurements, our remote sensing measurements with the incoherent scatter radars could be contaminated by meteors, cosmos rays etc. It is hence impossible to determine the very small Λ. Statistical distributions of Λ derived from the radar observations, however, are comparable with the rocket results given by *Blix et al.* [2003]. From the upper panel of Figure 8.5, the distribution of Λ against the volume reflectivities of VHF PMSE shows no correlation between these two parameters.

Depletions of electron density are one of the common properties of the PMSE environment. The occurrence of the electron density depletion is considered as a support for the existence of ice particles that become negatively charged due to electron attachment and slow down the

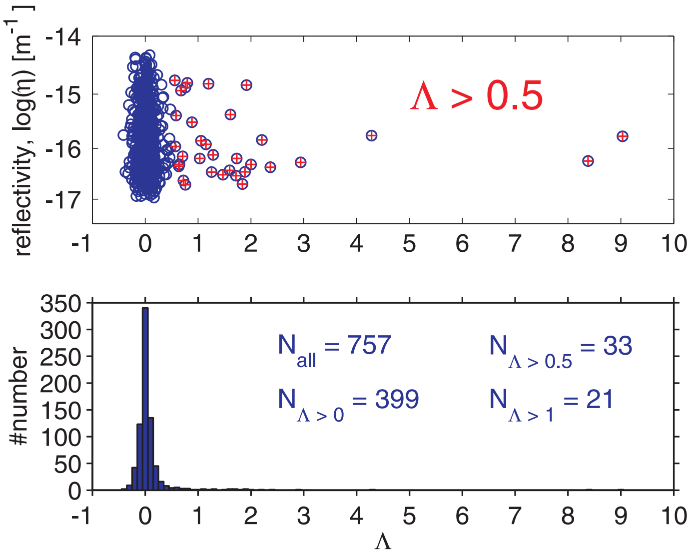

Figure 8.5: Upper panel: scatter plot of λ against corresponding reflectivities of VHF PMSE with $\lambda > 0.5$ indicated with red plus, showing no correlation between λ and reflectivities; Lower panel: histogram of λ.

diffusion of the remaining free electrons, which consequently results in small-scale electron structures observed as PMSE. From in situ observations and radar measurements, however, the charge number density of ice particles can be much smaller than electron number density in the presence of PMSE [*Cho et al.*, 1992; *Rapp and Lübken*, 2003]. The observations of the strong depletions of electron density could be due to the influence of instruments on measurements as well as the large difference in the observing volumes of radar and sounding rocket.

Chapter 9

Conclusions and outlook

In the current study, we have reported simultaneous and common-volume measurements of PMSE with the EISCAT Svalbard radar and the SOUSY Svalbard radar (78°N, 16°E) in June 2006 as well as with the EISCAT VHF and UHF radars (69°N, 19°E) during years between 2003 and 2007, respectively. The corresponding results have been presented in the previous chapters (Chapters 5–8). This chapter summarizes the results of this work and draws some conclusions followed by an outlook containing some ideas and suggestions for future research.

9.1 Conclusions

Chapter 5 presents the statistical properties of PMSE at different frequencies in term of occurrence rate and volume reflectivity derived from the observations with the ESR and SSR as well as the EISCAT VHF and UHF radars. PMSE reveal a pronounced frequency dependence with much smaller occurrence rate and volume reflectivity in the UHF range (at frequencies of 500 and 930 MHz corresponding to Bragg wavelengths of 30 and 16 cm, respectively) than in the VHF range (at frequencies of 53.5 and 224 MHz corresponding to Bragg wavelengths of 2.8 m and 67 cm, respectively). In addition, PMSE in the VHF range occurred within the entire altitude range between 80 and 92 km for the case of the SSR and between 80 and 91 km for the case of the EISCAT VHF radar which is significantly larger compared to the altitude range where UHF PMSE occurred. The absolute volume reflectivities of PMSE at each frequency reveal a very large dynamical range covering up to 5 orders of magnitude (in the case of the SSR and the EISCA VHF radar). Comparison of volume reflectivities from different times and locations are hence not suited for a comparison to theory. On the other hand, any theory explaining these echoes should consider this striking property of PMSE. With 5 summer seasons of PMSE observations with the EISCAT VHF radar we further presented the temporal variability of PMSE at 224 MHz. In Section 5.3 we compared the year-to-year variation patterns of PMSE at 224 MHz and at 53.5 MHz, respectively, to NLC as well as to the ionization level caused in the polar mesosphere by the solar radiation and the high-energy particle precipitation. We showed that the correlation of PMSE at 224 MHz with NLC is higher than that of PMSE at 53.5 MHz with NLC. This may tentatively be interpreted as meaning that the properties (sizes) of ice particles play a more important role for PMSE at higher frequencies. The seasonal variation of PMSE occurrence rates shows that PMSE were observed from end of May (in year 2003) until middle of August (in year 2007). The derived volume reflectivities show larger values in June and July (core summer) than in May and August. The diurnal variation of PMSE 224 MHz is dominated by a remarkable semidiurnal component which is in line with PMSE at 53.5 MHz. This behavior has previously be explained as the results of semidiurnal tide and the diurnal variations of D-region ionization caused by both solar radiation and high-energy particle precipitation.

In Chapter 6 we derived the factors leading to UHF PMSE in the frame of the TWLS-theory. In Section 6.2 spectral widths indicative of turbulent energy dissipation rates are calculated by fitting the Doppler spectra of the PMSE observations with a Gaussian function. The altitude profiles derived from the PMSE observations at different frequencies reveal a common feature that spectral widths increase with increasing altitudes. When comparing the derived altitude profiles when the ESR and SSR both observed PMSE, however, we note that the altitude profiles show on average larger values for the SSR at altitudes below about 85 km whereas agree nicely above that altitude. The behavior is hence explained by considering the different beam widths between the ESR (1.2°) and SSR (5°). This explanation is further supported by the corresponding results derived from independent observations with the EISCAT VHF and UHF radars that have close beam widths (1.2° × 1.7° and 0.5°, respectively). In addition, spectral widths above 85 km are significantly larger in the cases when the ESR and SSR both observed PMSE as compared to cases when PMSE were only observed at 53.5 MHz. The same behavior is also found for the case of the EISCAT VHF and UHF radars. This implies that enhanced turbulence plays an important role for the occurrence of PMSE in the UHF range (e.g., 500 and 930 MHz) at the upper part of PMSE. The electron densities are derived from the observations with the EISCAT VHF and UHF radars by comparing measured power values to the measurements of a calibration source of known brightness temperature and by using IS theory. In a statistical sense, the derived electron densities at 88 and 90 km show larger values at times when the EISCAT UHF radar observed PMSE as compared to when only the EISCAT VHF radar observed PMSE. This indicates only that the occurrence of UHF PMSE requires higher electron densities than VHF PMSE.

In Chapter 7 a test of the theoretical validity of the TWLS-theory was carried out with calibrated observations of PMSE simultaneously conducted with the ESR and SSR as well as with the EISCAT VHF and UHF radar. The corresponding results show an overall consistency between theoretical expectations and observations. Motivated by this finding, we introduced a new algorithm to calculate Schmidt numbers and hence radii of charged ice particles from the volume reflectivity ratios of PMSE simultaneously observed at two radar frequencies. Applying this algorithm to observations, we derived particle radii ranging from ∼10 to 70 nm (corresponding to Schmidt number from a few hundred and 32000) in the case of the ESR and SSR as well as the particle radii from ∼12 to 55 nm (corresponding to Schmidt number from 1000 to 20000) in the case of the EISCAT VHF and UHF radar. In addition, altitude profiles of ice particle radii reveal an increase with decreasing altitude which is in line with the current microphysical understanding of these ice particles which assumes that the particles nucleate at the mesopause and then grow and sediment to lower altitudes. We further compared our data set to the independent measurements from the Solar Occultation For Ice Experiment (SOFIE) on board the Aeronomy of Ice in the Mesosphere (AIM) spacecraft and the ALOMAR RMR Lidar, which results in overall excellent agreement. We note that this is the first time that radar observations give microphysical parameters of these mesospheric clouds in PMSE. Hence, this study opens a new window for the study of these clouds thereby yielding ice particle radii which are very difficult to measure otherwise. Looking at it from another side, this confirms that calibrated radar measurements of PMSE at two well separated frequencies (hence Bragg wavelengths) are a well suited tool for studying the microphysics of mesospheric ice clouds and related questions such as solar induced variations as well as long term trends.

Finally, in Section 8.3 we derived a total of 757 Λ values, i.e., the ratio between the charge number density of ice particles and electron number density, from 26 hours of observations with the EISCAT UHF radar in the presence of PMSE observed with the EISCAT VHF radar. The statistical distribution of Λ demonstrates only 4.4% of cases with $\Lambda > 0.5$, i.e., the large majority of cases with $\Lambda \ll 1$. Our results derived from the radar observations are comparable with the rocket results given by *Blix et al.* [2003]. From their previous in situ observations and our radar measurements, we conclude that the majority of PMSE occur under conditions where the charge number density of ice particles is much smaller than electron number density.

Taking all these results, we summarize the main findings of this work in the following list.

- From simultaneous and common-volume measurements of PMSE with the ESR and SSR as well as with the EISCAT VHF and UHF radars, statistical properties of PMSE at more frequencies of 224, 500, and 930 MHz are derived.
- PMSE reveal a pronounced frequency dependence that occurrence rate and volume reflectivity of PMSE in the UHF range are much smaller than in the VHF range.
- PMSE at 224 MHz shows a higher correlation with NLC than PMSE at 53.5 MHz whereas the correlation of PMSE at 224 MHz to the ionization levels is less significant compared to PMSE at 53.5 MHz. It roughly implies that the properties (sizes) of ice particles play a more important role for PMSE at higher frequencies.
- The seasonal variation of the PMSE occurrence rate and volume reflectivity are mainly determined by the seasonal variation of temperature and water content and consequently by the condition of supersaturation with respect to ice.
- PMSE in the UHF range (very small Bragg wavelengths) are very weak resulting in the poor statistics of them. The analysis of the conditions for UHF PMSE shows that their occurrence requires stronger turbulence in the upper part (above 84/85 km) and higher electron densities than VHF PMSE.
- The TWLS-theory of PMSE reveals that the ratio of volume reflectivities at two different frequencies should be equal to or larger than the ratio of the radar frequencies to the third power. Based on this relation, we tested the theory with calibrated observations of PMSE resulting in an overall agreement between theoretical expectations and observations.
- For the first time, radars give microphysical parameters of (charged) ice particles in PMSE and such small ice particles can be characterized at all. The comparison between our data and independent measurements with optical instruments shows an overall excellent agreement.
- Statistics of electron density depletions in the PMSE layers derived from radar observations show that the occurrence of PMSE take place in the condition with $\Lambda << 1$ which is consistent with previous rocket results.

9.2 Outlook

The EISCAT radars including the ESR and the main land instruments are very powerful tools for the study of PMSE and their environments. Together with the routine operation of these radars (with common program), measurements based on campaigns for special purposes are also carried out. For future investigations regarding PMSE, we propose to concentrate on the following promising issues:

1. **Extend data bases for better statistics**

   The ESR has been operating for several years with the special program 'jurg3' as well as its further developed modulation 'jurg4' since the campaign in 2006. The achieved datasets allow for the derivation of the statistical properties of PMSE at 500 MHz at such high latitude. In section 5.4 we presented the temporal variability of PMSE at 224 MHz derived from the observations during the years from 2003 to 2007. It is certainly necessary to extend the datasets to derive a more general picture of this topic.

2. **Compare turbulence estimates to alternative methods**

   Spectral information to derive turbulent energy dissipation rate and aspect sensitivity indicative of turbulence should be calculated from PMSE observations in order to gather insights into the mesospheric environments in the vicinity of PMSE. The results allow for a comparison to the observations with a narrow beam MF radars as well as with sounding rockets.

3. **Directly relate radar measurements optical measurements of ice particle radii**

   On the one hand, in Chapter 6 we discussed the conditions for the occurrence of UHF-PMSE by considering turbulence and electron density. The observations of ice particle radii with a multiwavelength lidar should be conducted in the presence of PMSE observed in the VHF and UHF ranges to further study the dependence of UHF-PMSE on the radii of ice particles. On the other hand, measurements of PMSE at two well separated frequencies (such as with the EISCAT VHF and UHF radars or with the EISCAT VHF radar and the ALWIN (MAARSY)) should be carried out together with multiwavelength lidar observations (with the ALOMAR RMR lidar) at the same location in order to allow a direct consistency check regarding inferred particle sizes.

4. **Extend multifrequency studies to different frequencies**

   It was discussed in *Rapp et al.* [2008] that a Schmidt number of 500 (corresponding to a particle radius < 10) is sufficient to explain the observations at frequencies of 53.5 and 224 MHz. The simultaneous observations of PMSE with the EISCAT VHF radar and the ALWIN (or MAARSY, 69°N, 16°E) as well as with EISCAT VHF radar and the MORRO (69°N, 19°E) allow for the derivation of the statistical distribution of the involved ice particles smaller than $\sim$10 nm that are invisible for optical instruments.

5. **Compare radar estimates of ice radii to heating experiments**

   The active heating experiments to modify PMSE allow insights into the charging characteristics of the ice particles. It is shown by *Havnes et al.* [2004] that the overshoot characteristic curves (OCC) are determined by ice particle densities and ice particle radii. This provides another possibility to derive the microphysical parameters of these particles (radii and number densities).

6. **Test whether ice number densities can be derived from radar measurements**

   A new theoretical expression of radar volume reflectivities deduced by *Varney et al.* [2011] predicts that the reflectivity depends on the ice particle density when the electron density is much larger than the ice particle density. This might be exploited to derive the ice particle density from radar observations.

Last but not least, with a solid physical understanding of PMSE at hand, observations of these layers can be used to monitor the dynamics and thermal structure of the mesopause regions on a continuous basis.

Appendix A

Tables

Table A.1: MST radars and IS radars worldwide used for the studies of PMSE (see Chapter 2)

Radar	Location	Frequency (MHz)	Reference
NERC MST radar	52°N, 4°E	46.5	*Thomas et al.* [1992]
CUPRI		46.9	*Providakes et al.* [1983]
Poker Flat MST radar	65°N,147°W	50	*Ecklund and Balsley* [1981]
AFRL VHF radar	62°N,145°W	50	*Ramos et al.* [2009]
ECAMP	62°S, 58°W	50	*Balsley et al.* [1995]
Resolute Bay radar	75°N,95°E	51.5	*Hocking et al.* [2001]
ESRAD	68°N, 21°E	52	*Chilson et al.* [1999]
Harz SOUSY	52°N, 10°E	53.5	*Czechowsky et al.* [1979]
ALOMAR SOUSY	69°N,16°E	53.5	*Singer et al.* [1995]
SSR	78°N,16°E	53.5	*Czechowsky et al.* [1998]
ALWIN	69°N,16°E	53.5	*Latteck et al.* [1999a]
OSWIN	54°N,12°E	53.5	*Latteck et al.* [1999b]
MAARSY	69°N,16°E	53.5	*Latteck et al.* [2010]
MARA		54.5	*Kirkwood et al.* [2007b]
Davis MST radar	69°S,78°E	55	*Morris et al.* [2006]
MORRO	69°N,19°E	56	*La Hoz and Havnes* [2008]
EISCAT VHF radar	69°N,19°E	224	*Hoppe et al.* [1988]
PFISR	65°N,147°W	450	*Nicolls et al.* [2007]
ESR	78°N,16°E	500	*Hall and Röttger* [2001]
EISCAT UHF radar	69°N,16°E	930	*Röttger et al.* [1990]
Sondrestrom radar	67°N,31°E	1290	*Cho and Kelley* [1992]

Table A.2: PMSE studied with calibrated radars at different frequencies. This table is updated from *Rapp and Lübken* [2004]. (see Chapter 2)

Frequency (Bragg scale) MHz (m)	Location	Reference	Reflectivity m^{-1}
49.6 (3.0)	Tromsø, (69°N)	*Röttger et al.* [1990]	$2.0 \cdot 10^{-12}$
50.0 (3.0)	Poker Flat, (65°N)	*Kelley and Ulwick* [1988]	$9.0 \cdot 10^{-15}$
51.5 (2.9)	Resolute Bay, (75°N)	*Latteck et al.* [2008]	$5.8 \cdot 10^{-12} - 4.2 \cdot 10^{-16}$
53.5 (2.8)	Andøya, (69°N)	*Inhester et al.* [1990]	$4.0 \cdot 10^{-12}$
		Belova et al. [2007]	$4.0 \cdot 10^{-13}$
		Latteck et al. [2008]	$1.9 \cdot 10^{-09} - 2.2 \cdot 10^{-16}$
53.5 (2.8)	Svalbard, (78°N)	*Röttger* [2001]	$2.2 \cdot 10^{-14}$ & $1.8 \cdot 10^{-15}$
55 (2.7)	Davis, (69°S)	*Latteck et al.* [2008]	$3.7 \cdot 10^{-11} - 1.5 \cdot 10^{-17}$
224 (0.67)	Tromsø, (69°N)	*Hoppe et al.* [1988]	$1.5 \cdot 10^{-16}$
		Röttger and LaHoz [1990]	$2.3 \cdot 10^{-17}$
		Hocking and Röttger [1997]	$1.3 \cdot 10^{-17} - 1.3 \cdot 10^{-15}$
		Belova et al. [2007]	$1.5 \cdot 10^{-14}$
		Rapp et al. [2008]	$5.0 \cdot 10^{-14}$
450 (0.33)	Poker Flat, (65°N)	*Nicolls et al.* [2007]	$2 - 3 \cdot 10^{-17}$
500 (0.3)	Svalbard, (78°N)	*Röttger* [2001]	$5.3 \cdot 10^{-19}$&$3.3 \cdot 10^{-20}$
930 (0.16)	Tromsø, (69°N)	*Röttger et al.* [1990]	$1.2 \cdot 10^{-18}$
		Belova et al. [2007]	$1.5 \cdot 10^{-18}$
		Rapp et al. [2008]	$3.0 \cdot 10^{-18}$
1290 (0.12)	Sondrestrom, (67°N)	*Cho and Kelley* [1992]	$2.5 \cdot 10^{-18}$

Table A.3: Observing times with the ESR during the PMSE-campaign 2006. All times are given in UT. Local solar time (LST) and UT are related by LST = UT + 68 min. At this time of the year, solar noon is at 10:52 UT. (see Chapter 4)

Year	Month	day	time [UT]	PMSE-time [UT]
2006	06	06	10:00–12:00	–
		07	10:00–12:00	–
		08	11:00–13:00	12:00–13:00
		09	11:00–13:00	11:00–13:00
		12	09:00–13:00	–
		14	09:00–13:00	09:00–11:00 & 12:00–13:00
		15	09:00–13:00	11:00–13:00
		18	09:00–13:00	09:00–11:00
		19	09:00–10:00 & 12:00–13:00	–
		20	09:00–13:00	09:00–10:00
		21	09:00–13:00	09:00–10:00 & 12:00–13:00
		22	09:00–13:00	–
		23	09:00–13:00	11:00–13:00
		24	09:00–13:00	–
		25	09:00–12:00	11:00–12:00
		26	09:00–13:00	10:00–11:00 & 12:00–13:00
		30	09:00–10:00	09:00–10:00
	07	01	09:00–13:00	–

Table A.4: Observing times with the EISCAT VHF and UHF radars during the campaign of 'arcdlayer-ht' in July 2004 and 2005. (see Chapter 4)

Year	Month	Day	VHF [UT]	UHF [UT]	UHF PMSE [UT]
2004	07	05	07:00–11:00	07:00–11:00	–
		06	07:00–11:00	08:20–11:00	–
		07	07:00–11:00	07:00–11:00	08:00–10:00
		08	07:00–10:00	07:00–08:40	–
		10	07:00–11:00	–	–
		11	07:00–11:30	07:00–11:30	–
		12	06:40–11:30	06:40–11:30	08:00–11:30
		13	06:50–11:20	06:50–11:10	07:00–10:00
		14	06:50–11:40	06:50–11:40	09:00–10:00
		15	06:50–12:00	06:50–12:00	–
2005	07	04	07:00–13:00	07:20–13:00	–
		05	07:00–13:00	07:00–13:00	12:00–13:00
		06	07:00–12:30	07:00–12:30	–
		07	07:00–13:00	07:40–13:00	–
		08	07:00–13:00	07:00–13:00	–
		09	07:30–13:30	07:30–13:30	08:00–10:00
		10	07:00–08:40	07:00–13:00	–

Table A.5: Observations with the EISCAT VHF and UHF radars used to derive Λ. (see Chapter 8)

Date	time [UT]	Experiment	UHF PMSE
2003-06-30	08:00–10:00	arcdlayer	Yes
2003-07-01	08:00–11:00	arcdlayer	No
2003-07-02	07:00–10:00	arcdlayer	No
2004-07-07	07:00–08:00	arcdlayer_ht	No
2004-07-14	07:00–10:00	arcdlayer_ht	Yes
2005-07-04	08:00–13:00	arcdlayer_ht	Yes
2005-07-05	11:00–13:00	arcdlayer_ht	Yes
2005-07-10	07:00–08:00	arcdlayer_ht	No
2007-08-11	08:00–10:00	arcdlayer	No
2007-08-12	10:00–13:00	arcdlayer	No

Appendix B

List of abbreviations

AIM	Aeronomy of Ice in the Mesosphere Spacecraft
ALOMAR	Arctic Lidar Observatory for Middle Atmosphere Research
ALWIN	ALOMAR Wind Radar
CARMA	Community Aerosol and Radiation Model for Atmospheres
CAWSES	Climate and Weather of the Sun-Earth System
CEDAR	Coupling, Energetics, and Dynamics of Atmospheric Regions
CIRA86	COSPAR International Reference Atmosphere 1986
COSPAR	Committee on Space Research
CUPRI	Cornell University Portable Radar Interferometer
ECOMA	Existence and Charge State of Meteor Smoke Particles in the Middle Atmosphere
ESR	EISCAT Svalbard Radar
ESRAD	Esrange MST Radar
EISCAT	European Incoherent Scatter Scientific Association
FS	Falling Sphere
IRI	International Reference Ionosphere
ISR	Incoherent Scatter Radar.
LIMA	Leibniz-Institute Middle Atmosphere Model
MAARSY	Middle Atmosphere ALOMAR Radar System
MASS	Mesospheric Aerosol Sampling Spectrometer
MLT	Mesosphere and Lower Thermosphere region
MORRO	Mobile Rocket and Radar Observatory
MST	Mesosphere-Stratosphere-Troposphere
NLC	Noctilucent clouds
NSMR	Nippon/Norway Svalbard Meteor Radar
OSWIN	Ostsee wind radar
PMC	Polar Mesospheric Clouds
PMSE	Polar Mesosphere Summer Echoes
PMWE	Polar Mesosphere Winter Echoes
RMR	Rayleigh/Mie/Raman
SNR	Signal-to-Noise Ratio
SOFIE	Solar Occultation For Ice Experiment
SOUSY	Sounding System for atmospheric structure and dynamics
SPEAR	Space Plasma Exploration by Active Radar
SSR	SOUSY Svalbard Radar
UHF	Ultra High Frequency
VHF	Very High Frequency

Bibliography

Appleton, E. V., Regularities and irregularities in the ionosphere - i, *Proc. R. Soc., London, A 162*, 451, 1937.

Appleton, E. V., and W. R. Piggott, Ionospheric absorption measurements during a sunspot cycle, *J. Atmos. Terr. Phys.*, *5*, 141, 1954.

Balsley, B. B., and K. S. Gage, The MST radar technique: Potential for middle atmospheric studies, *J. Appl. Geophys.*, *118*, 452–493, 1980.

Balsley, B. B., and M. Huaman, On the relationship between seasonal occurrence of northern hemispheric polar mesosphere summer echoes and mean mesopause temperatures, *J. Geophys. Res.*, *102*, 2021–2024, 1997.

Balsley, B. B., W. L. Ecklund, and D. C. Fritts, VHF echoes from the high-latitude mesosphere and lower thermosphere: Observations and interpretations, *J. Atmos. Sci.*, *40*, 2451–2466, 1983.

Balsley, B. B., R. F. Woodman, M. Sarango, R. Rodriguez, J. Urbina, E. Ragaini, J. Carey, M. Huaman, and A. Giraldez, On the lack of southern-hemisphere PMSE, *J. Geophys. Res.*, *100*, 11685–11693, 1995.

Baron, M., EISCAT progress 1983–1985, *J. Atmos. Terr. Phys.*, *48*, 767–772, 1986.

Batchelor, G. K., Small-scale variation of convected quantities like temperature in a turbulent fluid, *J. Fluid Mech.*, *5*, 113–133, 1959.

Baumgarten, G., J. Fiedler, F.-J. Lübken, and G. von Cossart, Particle properties and water content of noctilucent clouds and their interannual variation, *J. Geophys. Res., 113, D06203*, doi:10.1029/2007JD008884, 2008.

Becker, E., and G. Schmitz, Climatological effects of orography and land-sea heating contrasts on the gravity wave driven circulation of the mesosphere, *J. Atmos. Sci.*, *60*, 103–118, 2003.

Bellan, P. M., Ice iron/sodium film as cause for high noctilucent cloud radar reflectivity, *J. Geophys. Res.*, *113*, 2008.

Belova, E., P. Dalin, and S. Kirkwood, Polar mesosphere summer echoes: A comparison of simultaneous observations at three wavelengths, *Ann. Geophys.*, *25*, 2487–2496, 2007.

Berger, U., and U. von Zahn, The two-level structure of the mesopause: A model study, *J. Geophys. Res.*, *104*, 22,083–22,093, 1999.

Beynon, W. J. G., and P. J. S. Willianms, Incoherent scatter of radio waves from the ionosphere, *Rep. Prog. Phys.*, *41*, 909–956, 1978.

Bilitza, D., International reference ionosphere 2000, *Radio Sci.*, *36(2)*, 261–275, 2001.

Blix, T. A., Small scale plasma and charged aerosol variations and their importance for polar mesosphere summer echoes, *Adv. Space Res.*, *24*, 537–546, 1999.

Blix, T. A., M. Rapp, and F.-J. Lübken, Relations between small scale electron number density fluctuations, radar backscatter and charged aerosol particles, *J. Geophys. Res.*, *108(D8), 8450, doi:10.1029/2002JD002430*, 2003.

Bowles, K. L., Observations of vertical-incidence scatter from the ionosphere at 41 Mc/sec, *Phys. Rev. Letters*, *1*, 454–455, 1958.

Bremer, J., P. Hoffmann, and T. L. Hansen, Geomagnetic control of polar mesosphere summer echoes, *Ann. Geophys.*, *18*, 202–208, 1996a.

Bremer, J., P. Hoffmann, W. Singer, C. E. Meek, and R. Rüster, Simultaneous PMSE observations with ALOMAR-SOUSY and EISCAT-VHF radar during the ECHO-94 campaign, *Geophys. Res. Lett.*, *23*, 1075–1078, 1996b.

Bremer, J., T. L. Hansen, P. Hoffmann, and R. Latteck, Dependence of polar mesosphere summer echoes on solar and geomagnetic activity, *Adv. Space Res.*, *28*, 1071–1076, 2001.

Bremer, J., P. Hoffmann, R. Latteck, and W. Singer, Seasonal and long term variation of PMSE from VHF radar observations at Andenes, Norway, *J. Geophys. Res.*, *108(D8), 8438, doi:10.1029/2002JD002369*, 2003.

Bremer, J., P. Hoffmann, J. Höffner, R. Latteck, W. Singer, M. Zecha, and O. Zeller, Long-term changes of mesospheric summer echoes at polar and middle latitudes, *J. Atmos. Sol. Terr. Phys.*, *68(17)*, 1940–1951, 2006.

Bremer, J., P. Hoffmann, R. Latteck, W. Singer, and M. Zecha, Long-term changes of (polar) mesosphere summer echoes, *J. Atmos. Sol. Terr. Phys.*, *71*, 1571–1576, 2009.

Chilson, P., S. Kirkwood, and A. Nilsson, The Esrange MST radar: A brief introduction and procedure for range validation using balloon, *Radio Sci.*, *34(2)*, 427–436, 1999.

Chilson, P. B., E. Belova, M. Rietveld, S. Kirkwood, and U.-P. Hoppe, First artificially induced modulation of PMSE using the EISCAT heating facility, *Geophys. Res. Lett.*, *27*, 3801–3804, 2000.

Cho, J. Y., C. M. Alcala, M. C. Kelley, and W. E. Swartz, Further effects of charged aerosols on summer mesospheric radar scatter, *J. Atmos. Terr. Phys.*, *58*, 661–672, 1996.

Cho, J. Y. N., and M. C. Kelley, Enhancement of Thomson scatter by charged aerosols in the polar mesosphere: Measurements with a 1.29-GHz radar, *Geophys. Res. Lett.*, *19*, 1097–1100, 1992.

Cho, J. Y. N., and J. Röttger, An updated review of polar mesosphere summer echoes: Observation, theory, and their relationship to noctilucent clouds and subvisible aerosols, *J. Geophys. Res.*, *102*, 2001–2020, 1997.

Cho, J. Y. N., T. M. Hall, and M. C. Kelley, On the role of charged aerosols in polar mesosphere summer echoes, *J. Geophys. Res.*, *97*, 875–886, 1992.

Collis, P. N., T. Turunen, and E. Turunen, Evidence of heavy positive ions at the summer arctic mesopause from the EISCAT UHF-incoherent scatter radar, *Geophys. Res. Lett.*, *15*, 148, 1988.

Croskey, C., J. Mitchell, M. Friedrich, K. Torkar, U.-P. Hoppe, and R. Goldberg, Electrical structure of PMSE and NLC regions during the DROPPS program, *Geophys. Res. Lett.*, *28*, 1427–1430, 2001.

Croskey, C. L., J. D. Mitchell, R. A. Goldberg, T. A. Blix, M. Rapp, R. Latteck, M. Friedrich, and B. Smiley, Coordinated investigation of plasma and neutral density fluctuations and particles during the MaCWAVE/MIDAS summer 2002 program, *Geophys. Res. Lett.*, *31*, 2004.

Czechowsky, P., R. Rüster, and G. Schmidt, Variations of mesospheric structures in different seasons, *Geophys. Res. Lett.*, *6*, 459–462, 1979.

Czechowsky, P., G. Schmidt, and R. Rüster, The mobile SOUSY Doppler radar: Technical design and first results, *Radio Sci.*, *19*, 875–886, 1984.

Czechowsky, P., I. M. Reid, and R. Rüster, VHF radar measurements of the aspect sensitivity of the summer polar mesospaus echoes over Andenes (69°N,16°E), Norway, *Geophys. Res. Lett.*, *15*, 1259–1262, 1988.

Czechowsky, P., J. Klostermeyer, J. Röttger, R. Rüster, and G. Schmidt, The SOUSY-Svalbard-Radar for middle and lower atmosphere research in the polar region, *Proceedings of the 8th workshop on Technical and Scientific Aspects of MST Radar, SCOSTEP, Boulder, Colorado, USA*, pp. 318–321, 1998.

D'Angelo, N., Ia/da waves and polar mesospheric summer echoes, *Phys. Lett. A*, *336*, 204–209, 2005.

Dougherty, J. P., and J. D. T. Farley, A theory of incoherent scattering of radio waves by a plasma, 3 scattering in a partly ionized gas, *J. Geophys. Res.*, *68*, 5473–5486, 1963.

Ecklund, W. L., and B. B. Balsley, Long-term observations of the Arctic mesosphere with the MST radar at Poker Flat, Alaska, *J. Geophys. Res.*, *86*, 7775–7780, 1981.

Engler, N., R. Latteck, B. Strelnikov, W. Singer, and M. Rapp, Turbulent energy dissipation rates observed by Doppler MST radar and by rocket-borne instruments during the MIDAS/MaCWAVE campaign 2002, *Ann. Geophys.*, *23*, 1147–1156, 2005.

Fiedler, J., G. Baumgarten, and G. von Cossart, Mean diurnal variations of noctilucent clouds during 7 years of lidar observations at ALOMAR, *Ann. Geophys.*, *23*, 1175–1181, 2005.

Fiedler, J., G. Baumgarten, and F.-J. Lübken, NLC observations during one solar cycle above ALOMAR, *J. Atmos. Sol. Terr. Phys.*, *71*, 424–433, 2009.

Fleming, E. L., S. Chandra, M. R. Schoeberl, and J. J. Barnett, Monthly mean global climatology of temperature, wind, geopotential height and pressure for 0–120 km, *National Aeronautics and Space Administration*, *Technical Memorandum 100697, Washington, D.C.*, 1988.

Folkestad, K. T., T. Hagfors, and S. Westerlund, EISCAT: An updated description of technical characteristics and operational capabilities, *Radio Sci.*, *18*, 867–879, 1983.

Franke, S. J., J. Röttger, C. LaHoz, and C. H. Liu, Frequency domain interferometry of polar mesosphere summer echoes with the EISCAT VHF radar: A case study, *Radio Sci.*, *27*, 417–428, 1992.

Friedrich, M., and S. Kirkwood, The D-region background at high latitudes, *Adv. Space Res.*, *25(1)*, 15–23, 2000.

Friedrich, M., K. M. Torkar, W. Singer, I. Strelnikova, M. Rapp, and S. Robertson, Signatures of mesospheric particles in ionospheric data, *Ann. Geophys.*, *27*, 823–829, 2009.

Fritts, D. C., and M. J. Alexander, Gravity wave dynamics and effects in the middle atmosphere, *Rev. Geophys.*, *41(1), 1003*, doi:10.1029/2001RG000106, 2003.

Garcia, R. R., Dynamics, radiation, and photochemistry in the mesosphere: Implications for the formation of noctilucent clouds, *J. Geophys. Res.*, *94*, 14,605–14,616, 1989.

Gibson-Wilde, D., J. Werne, D. Fritts, and R. Hill, Direct numerical simulation of VHF radar measurements of turbulence in the mesosphere, *Radio Sci.*, *35*, 783–798, 2000.

Goldberg, R., et al., DROPPS: A study of the polar summer mesosphere with rocket, radar and lidar, *Geophys. Res. Lett.*, *28*, 1407–1410, 2001.

Goldberg, R., E. Kopp, G. Witt, and W. Swartz, An overview of NLC-91: A rocket/radar study of the polar summer mesosphere, *Geophys. Res. Lett.*, *20*, 2443–2446, 1993.

Gordberg, R., et al., Dropps: A study of the polar summer mesosphere with rocket, radar and lidar, *Geophys. Res. Lett.*, *28*, 1407–1410, 2001.

Gordley, L. L., et al., The solar occultation for ice experiment (SOFIE), *J. Atmos. Sol. Terr. Phys.*, *71*, 300–315, 2009.

Gordon, W. E., Incoherent scattering of radio waves by free electrons with applications to space exploration by radar, *Proc. IRE*, *46*, 1824–1829, 1958.

Hall, C., and J. Röttger, Initial observations of polar mesospheric summer echoes using the EISCAT Svalbard Radar, *Geophys. Res. Lett.*, *28*, 131–134, 2001.

Hall, C. M., T. Aso, and M. Tsutsumi, An examination of high latitude upper mesosphere dynamic stability using the Nippon/Norway Svalbard Meteor Radar, *Geophys. Res. Lett.*, *29(8), 1280*, doi:10.1029/2001GL014229, 2002.

Hall, C. M., T. Aso, A. H. Manson, C. E. Meek, S. Nozawa, and M. Tsutsumi, High-latitude mesospheric mean winds: A comparison between Tromsø (69°N) and Svalbard (78°N), *J. Geophys. Res.*, *108(D19),4598*, doi:10.1029/2003JD003509, 2003.

Havnes, O., U. de Angelis, R. Bingham, C. K. Goertz, G. E. Morfill, and V. Tsytovich, On the role of dust in the summer mesopause, *J. Atmos. Terr. Phys.*, *52*, 637–643, 1990.

Havnes, O., J. Trøim, T. Blix, W. Mortensen, L. I. Næsheim, E. Thrane, and T. Tønnesen, First detection of charged dust particles in the Earth's mesosphere, *J. Geophys. Res.*, *101*, 10839–10847, 1996.

Havnes, O., A. Brattli, T. Aslaksen, W. Singer, R. Latteck, T. Blix, E. Thrane, and J. Trøim, First common volume observations of layered plasma structures and polar mesospheric summer echoes by rocket and radar, *Geophys. Res. Lett.*, *28*, 1419–1422, 2001.

Havnes, O., C. La Hoz, A. Biebricher, M. Kassa, T. Meseret, L. I. Naesheim, and T. Zivkovic, Investigation of the mesospheric PMSE conditions by use of the new overshoot effect, *Physica Scripta.*, pp. 70–78, 2004.

Hecht, J. H., Instability layers and airglow imaging, *Rev. Geophys.*, *42*, 2004.

Heisenberg, W., Zur statistischen Theorie der Turbulenz, *Z. Physik*, *124*, 628–657, 1948.

Hervig, M., R. Thompson, M. McHugh, L. Gordley, J. R. III, and M. Summers, First confirmation that water ice is the primary component of polar mesospheric clouds, *Geophys. Res. Lett.*, *28*, 971–974, 2001.

Hervig, M., M. Rapp, R. Latteck, and L. Gordley, Observations of mesospheric ice particles from the ALWIN radar and SOFIE, *J. Atmos. Sol. Terr. Phys.*, *73*, 2176–2183, 2011.

Hervig, M. E., L. L. Gordley, M. H. Stevens, J. M. R. III, S. M. Bailey, and G. Baumgarten, Interpretation of SOFIE PMC measurements: Cloud identification and derivation of mass density, particle shape, and particle size, *J. Atmos. Sol. Terr. Phys.*, *71*, 316–330, 2009.

Hill, R. J., Nonneutral and quasi-neutral diffusion of weakly ionized multiconstituent plasma, *J. Geophys. Res.*, *83*, 989–998, 1978.

Hocking, W., Middle atmosphere program, vol. 30, chap. target parameter estimation, *Handbook for MAP*, pp. 228–268, 1989.

Hocking, W. K., On the extraction of atmospheric turbulence parameters from radar backscatter Doppler spectra: 1. theory, *J. Atmos. Terr. Phys.*, *45*(2/3), 89–102, 1983.

Hocking, W. K., Measurement of turbulent energy dissipation rates in the middle atmosphere by radar techniques: A review, *Radio Sci.*, *20*, 1403–1422, 1985.

Hocking, W. K., and J. Röttger, Pulse-length dependence of radar signal strengths for Fresnel backscatter, *Radio Sci.*, *18*, 1312–1324, 1983.

Hocking, W. K., and J. Röttger, Studies of polar mesosphere summer echoes over EISCAT using calibrated signal strengths and statistical parameters, *Radio Sci.*, *32*, 1425–1444, 1997.

Hocking, W. K., M. Kelley, R. Rogers, W. O. J. Brown, D. Moorcroft, and J.-P. S. Maurice, Resolute Bay VHF radar: A multipurpose tool for studies of tropospheric motions, middle atmosphere dynamics, meteor physics, and ionospheric physics, *Radio Sci.*, *36*, 1839–1857, 2001.

Hoffmann, P., W. Singer, D. Keuer, J. Bremer, and R. Rüster, Mean diurnal variation of PMSE as measured with the ALOMAR SOUSY radar during summer 1996, *ESA*, *SP-397*, 471–475, 1997.

Hoffmann, P., W. Singer, and J. Bremer, Mean seasonal and diurnal variation of PMSE and winds from 4 years of radar observations at ALOMAR, *Geophys. Res. Lett.*, *26*, 1525–1528, 1999.

Hoffmann, P., M. Rapp, A. Serafimovich, and R. Latteck, On the occurrence and formation of multiple layers of polar mesosphere summer echoes, *Geophys. Res. Lett.*, *32*, L05812, 2005.

Hoffmann, P., M. Rapp, J. Fiedler, and R. Latteck, Influence of tides and gravity waves on layering processes in the polar summer mesopause region, *Ann. Geophys.*, *26*(12), 4013–4022, 2008.

Höffner, J., and F.-J. Lübken, Potassium lidar temperatures and densities in the mesopause region at Spitsbergen (78°N), *J. Geophys. Res.*, *112, D20114*, doi:10.1029/2007JD008612, 2007.

Hoppe, U.-P., and D. Fritts, On the downward bias in vertical velocity measurements by VHF radars, *Geophys. Res. Lett.*, *22*, 619–622, 1994.

Hoppe, U.-P., and D. C. Fritts, High-resolution measurements of vertical velocity with the European incoherent scatter VHF radar 1. Motion field characteristics and measurement biases, *J. Geophys. Res.*, *100(D8)*, 16,813–16,825, 1995.

Hoppe, U.-P., C. Hall, and J. Röttger, First observations of summer polar mesospheric backscatter with a 224 MHz radar, *Geophys. Res. Lett.*, *15*, 28–31, 1988.

Huaman, M. M., M. C. Kelley, W. K. Hocking, and R. F. Woodman, Polar mesosphere summer echo studies at 51.5 MHz at Resolute Bay, Canada: Comparison with Poker Flat results, *Radio Sci.*, *36*, 1823–1837, 2001.

Inhester, B., J. Ulwick, J. Cho, M. Kelley, and G. Schmidt, Consistency of rocket and radar electron density observations: implications about the anisotropy of turbulence, *J. Atmos. Terr. Phys.*, *52*, 855–873, 1990.

Inhester, B., J. Klostermeyer, F.-J. Lübken, and U. von Zahn, Evidence for ice clouds causing polar mesosphere summer echoes, *J. Geophys. Res.*, *99*, 20,937–20,954, 1994.

Jackel, B. J., Characterization of auroral radar power spectra and autocorrelation functions, *Radio Sci.*, *35*, 10009–10024, 2000.

Karashtin, A. N., Y. V. S. abd V. I. Abramov, I. F. Belov, V. V. Bychkov, E. B. Eryshev, and G. P. Komrakov, First HF radar measurements of summer mesopause echoes at SURA, *Ann. Geophys.*, *15*, 935–941, 1997.

Karlsson, B., and M. Rapp, Latitudinal dependence of noctilucent cloud growth, *Geophys. Res. Lett.*, *33*, L11812, 2006.

Kelley, M. C., and J. C. Ulwick, Large- and small-scale organization of electrons in the high-latitude mesosphere: implications of the STATE data, *J. Geophys. Res.*, *93*, 7001–7008, 1988.

Kelley, M. C., D. T. Farley, and J. Röttger, The effect of cluster ions on anomalous VHF backscatter from the summer polar mesosphere, *Geophys. Res. Lett.*, *14*, 1031–1034, 1987.

Kelley, M. C., M. Huaman, C. Y. Chen, C. Ramos, F. Djuth, and E. Kennedy, Polar mesosphere summer observations at HF frequencies using the HAARP Gakona Ionospheric Observatory, *Geophys. Res. Lett.*, *doi: 10.1029/2001GL013411*, 2002.

Kirkwood, S., and K. Stebel, Influence of planetary waves on noctilucent cloud occurrence over NW Europe, *J. Geophys. Res.*, *108 (D8), 8440, doi:10.1029/2002JD002356*, 2003.

Kirkwood, S., P. N. Collis, and W. Schmidt, Calibration of electron densities for the EISCAT UHF radar, *J. Atmos. Terr. Phys.*, *48*, 773–775, 1986.

Kirkwood, S., V. Barabash, P. Chilson, A. Rechou, K. Stebel, P. Espy, G. Witt, and J. Stegman, The 1997 PMSE season - its relation to wind, temperature and water vapour, *Geophys. Res. Lett.*, *25*, 1867–1870, 1998.

Kirkwood, S., H. Nilsson, R. J. Morris, A. R. Klekociuk, D. A. Holdsworth, and N. J. Mitchell, A new height for the summer mesopause: Antarctica, December 2007, *Geophys. Res. Lett.*, *35*, L23810, 2007a.

Kirkwood, S., I. Wolf, H. Nilsson, P. Dalin, D. Mikhaylova, and E. Belova, Polar mesosphere summer echoes at Wasa, Antarctica (73°s): First observations and comparison with 68°S, *Geophys. Res. Lett.*, *34*, L15803, 2007b.

Klekociuk, A. R., R. J. Morris, and J. L. Innis, First southern hemisphere common volume measurements of PMC and PMSE, *Geophys. Res. Lett.*, *35*, L24804, 2008.

Klostermeyer, J., On the diurnal variation of polar mesosphere summer echoes, *Geophys. Res. Lett.*, *26*, 3301–3304, 1999.

Kolmogorov, A. N., The local structure of turbulence in incompressible viscous fluids for very high Reynolds numbers, *Dokl. Akad. Nauk SSSR*, *30*, 301–305, 1941.

La Hoz, C., and O. Havnes, Artificial modification of polar mesospheric winter echoes with an RF heater: Do charged dust particles play an active role?, *J. Geophys. Res.*, *113*, D19205, 2008.

La Hoz, C., O. Havnes, L. I. Naesheim, and D. L. Hysell, Observations and theories of polar mesospheric summer echoes at a Bragg wavelength of 16 cm, *J. Geophys. Res.*, *111, D04203, doi:10.1029/2005JD006044*, 2006.

Latteck, R., W. Singer, and H. Bardey, The ALWIN MST radar: Technical design and performance, *Proceedings of the 14th ESA Symposium on European Rocket and Balloon Programmes and Related Research, Potsdam, Germany (ESA SP–437)*, pp. 179–184, 1999a.

Latteck, R., W. Singer, and J. Höffner, Mesosphere summer echoes as observed by VHF radar at Kühlungsborn, *Geophys. Res. Lett.*, *26*, 1533–1536, 1999b.

Latteck, R., W. Singer, R. J. Morris, D. A. Holdsworth, and D. J. Murphy, Observation of polar mesosphere summer echoes with calibrated VHF radars at 69° in the Northern and Southern hemispheres, *Geophys. Res. Lett.*, *34, L14805, doi: 10.1029/2007GL030032*, 2007.

Latteck, R., W. Singer, R. J. Morris, W. K. Hocking, D. J. Murphy, D. A. Holdsworth, and N. Swarnalingam, Similarities and differences in polar mesosphere summer echoes observed in the Arctic and Antarctica, *Ann. Geophys.*, *26*, 2795–2806, 2008.

Latteck, R., W. Singer, M. Rapp, and T. Renkwitz, Maarsy - the new MST radar on Andøya/Norway, *Adv. Radio Sci.*, *8*, 219–224, 2010.

Lehtinen, M. S., and A. Huuskonen, General incoherent scatter analysis and GUISDAP, *J. Atmos. Terr. Phys.*, *58*, 435–452, 1996.

Li, Q., et al., Microphysical parameters of mesospheric ice clouds derived from calibrated observations of polar mesosphere summer echoes at Bragg wavelengths of 2.8 m and 30 cm, *J. Geophys. Res.*, *115, D00I13*, doi:10.1029/2009JD012271, 2010.

Li, Q., and M. Rapp, PMSE-observations with the EISCAT VHF and UHF-Radars: Statistical properties, *J. Atmos. Sol. Terr. Phys.*, *73(9)*, 944–956, 2011.

Lie-Svendsen, O., T. A. Blix, U.-P. Hoppe, and E. V. Thrane, Modeling the plasma response to small-scale aerosol particle pertubations in the mesopause region, *J. Geophys. Res.*, *108*, 8442, 2003.

Lindzen, R. S., Turbulence and stress owing to gravity wave and tidal breakdown, *J. Geophys. Res.*, *86(C10)*, 9707–9714, 1981.

Liu, J. Y., C. J. Pan, and C. C. Lee, VHF radar and MF/HF dynasonde observations during polar mesosphere summer echoes conditions at EISCAT, *Earth Planet Space*, *54*, 691–698, 2002.

Lübken, F.-J., Seasonal variation of turbulent energy dissipation rates at high latitudes as determined by in situ measurements of neutral density fluctuations, *J. Geophys. Res.*, *104*, 13,441–13,456, 1997.

Lübken, F.-J., Thermal structure of the Arctic summer mesosphere, *J. Geophys. Res.*, *104*, 9135–9149, 1999.

Lübken, F.-J., and U. Berger, Interhemispheric comparison of mesospheric ice layers from the LIMA model, *J. Atmos. Sol. Terr. Phys.*, *69*, 2292–2308, 2007.

Lübken, F.-J., and A. Müllemann, Temperatures, densities, and winds in the high latitudes (78°N) mesosphere, *Adv. Space Res.*, *32*, 731–740, 2003a.

Lübken, F.-J., and A. Müllemann, First in situ temperature measurements in the summer mesosphere at very high latitudes (78°N), *J. Geophys. Res.*, *108(D8), 8448*, doi:10.1029/2002JD002753, 2003b.

Lübken, F.-J., G. Lehmacher, T. Blix, U.-P. Hoppe, E. Thrane, J. Cho, and W. Swartz, First in-situ observations of neutral and plasma density fluctuations within a PMSE layer, *Geophys. Res. Lett.*, *20*, 2311–2314, 1993.

Lübken, F.-J., J. Giebeler, T. Blix, E. Thrane, W. Singer, and J. Bremer, In-situ measurement of the Schmidt number within a PMSE layer, *Geophys. Res. Lett.*, *21*, 1651–1654, 1994.

Lübken, F.-J., M. Rapp, T. Blix, and E. Thrane, Microphysical and turbulent measurements of the Schmidt number in the vicinity of polar mesosphere summer echoes, *Geophys. Res. Lett.*, *25*, 893–896, 1998.

Lübken, F.-J., M. Rapp, and P. Hoffmann, Neutral air turbulence and temperatures in the vicinity of polar mesosphere summer echoes, *J. Geophys. Res.*, *107(D15), doi:10.1029/2001JD000915*, 2002.

Lübken, F.-J., M. Zecha, J. Höffner, and J. Röttger, Temperatures, polar mesosphere summer echoes, and noctilucent clouds over Spitsbergen (78° N), *J. Geophys. Res.*, *109*(D11), 2004.

Lübken, F.-J., U. Berger, and G. Baumgarten, Stratospheric and solar cycle effects on long-term variability of mesospheric ice clouds, *J. Geophys. Res.*, *114*, D00I06, 2009a.

Lübken, F.-J., J. Lautenbach, J. Höffner, M. Rapp, and M. Zecha, First continuous temperature measurements within polar mesosphere summer echoes, *J. Atmos. Sol. Terr. Phys.*, *71*, 453–463, 2009b.

Megner, L., M. Khaplanov, G. Baumgarten, J. Gumbel, J. Stegman, B. Strelnikov, and S. Robertson, Large mesospheric ice particles at exceptionally high altitudes, *Ann. Geophys.*, *27*, 943–951, 2009.

Merkel, A. W., R. R. Garcia, S. M. Bailey, and J. M. R. III, Observational studies of planetary waves in PMCs and mesospheric temperature measured by SNOE and SABER, *J. Geophys. Res.*, *113*, D14202, 2008.

Mitchell, J., C. Croskey, and R. Goldberg, Evidence for charged aerosol particles and associated meter-scale structure in identified PMSE/NLC regions, *Geophys. Res. Lett.*, *28*, 1423–1426, 2001.

Mitchell, J. D., C. L. Croskey, R. A. Goldberg, and M. Friedrich, Charged particles in the polar mesopause region: Probe measurements from the MaCWAVE and DROPPS programs, *Proceedings of the 16th ESA Symposium on European Rocket and Balloon Programmes and Related Research, St. Gallen, Switzerland (ESA SP–530)*, pp. 351–356, 2003.

Moorcroft, D. R., The shape of auroral backscatter spectra, *Geophys. Res. Lett.*, *31*, 9802–9805, 2004.

Morris, R. J., D. J. Murphy, I. M. Reid, D. A. Holdsworth, and R. A. Vincent, First polar mesosphere summer echoes observed at Davis, Antarctica (68°S), *Geophys. Res. Lett.*, *31,L16111, doi: 10.1029/2004GL020352*, 2004.

Morris, R. J., D. J. Murphy, R. A. Vincent, D. A. Holdsworth, A. R. Klekociuk, and I. M. Reid, Characteristics of the wind, temperature and PMSE field above Davis, Antarctica, *J. Atmos. Sol. Terr. Phys.*, *68*, 418–435, 2006.

Morris, R. J., D. J. Murphy, A. R. Klekociuk, and D. A. Holdsworth, First complete season of PMSE observations above Davis, Antartica, and their relation to winds and temperatures, *Geophys. Res. Lett.*, *34*, L05805, 2007.

Morris, R. J., A. R. Klekociuk, R. Latteck, W. Singer, D. A. Holdsworth, and D. J. Murphy, Inter-hemispheric asymmetry in polar mesosphere summer echoes and temperature at 69° latitude, *J. Atmos. Sol. Terr. Phys.*, *71*, 464–469, 2009.

Murphy, D. J., W. K. Hocking, and D. C. Fritts, An assessment of the effect of gravity waves on the width of radar Doppler spectra, *J. Atmos. Terr. Phys.*, *56*, 17–29, 1994.

Murphy, D. M., and T. Koop, Review of the vapour pressures of ice and supercooled water for atmospheric applications, *Quart. J. R. Met. Soc.*, *131*, 1539–1565, 2005.

Naesheim, L. I., O. Havnes, and C. L. Hoz, A comparison of polar mesosphere summer echo at VHF (224 MHz) and UHF (930 MHz) and the effects of artificial electron heating, *J. Geophys. Res.*, *113*, 2008.

Nastrom, G. D., and F. D. Eaton, Turbulence eddy dissipation rates from radar observations at 5-20 km at white sands missile range, *J. Geophys. Res.*, *102*, 19,495–19,505, 1997.

Nicolls, M. J., C. J. Heinselman, E. A. Hope, S. Ranjan, M. C. Kelley, and J. D. Kelly, Imaging of polar mesosphere summer echoes with the 450 MHz Poker Flat advanced modular incoherent scatter radar, *Geophys. Res. Lett.*, *34*, L20102, 2007.

Nicolls, M. J., M. C. Kelley, and R. H. V. C. J. Heinselman, Spectral observations of polar mesospheric summer echoes at 33 cm (450 MHz) with the Poker Flat incoherent scatter radar, *J. Atmos. Sol. Terr. Phys.*, *71*, 662–674, 2009.

Nielsen, K., M. J. Taylor, R. E. Hibbins, and M. J. Jarvis, Climatology of short-period mesospheric gravity waves over Halley, Antarctica (76°S, 27°N), *J. Atmos. Sol. Terr. Phys.*, *71*, 991–1000, 2009.

Nussbaumer, V., K.-H. Fricke, M. Langer, W. Singer, and U. von Zahn, First simultaneous and common volume observations of noctilucent clouds and polar mesosphere summer echoes by lidar and radar, *J. Geophys. Res.*, *101(D14)*, 19,161–19,167, 1996.

Palmer, J. R., H. Rishbeth, G. O. L. Jones, and P. J. S. Williams, A statistical study of polar mesosphere summer echoes observed by EISCAT, *J. Atmos. Terr. Phys.*, *58*, 307–315, 1996.

Pedersen, A., J. Troim, and J. Kane, Rocket measurement showing removal of electrons above the mesopause in summer at high latitudes, *Plan. Space Sci.*, *18*, 945–947, 1969.

Picone, J. M., A. E. Hedin, D. P. Drob, and A. C. Aikin, NRLMSISE-00 empirical model of the atmosphere: Statistical comparison and scientific issues, *J. Geophys. Res.*, *107(A12, 1468)*, doi:10.1029/2002JA009430, 2002.

Providakes, J. P., W. E. Swartz, D. T. Farley, and B. G. Fejer, First VHF auroral radar interferometer observations, *Geophys. Res. Lett.*, *10*, 401–404, 1983.

Raizada, S., M. Rapp, F.-J. Lübken, J. Höffner, M. Zecha, and J. M. C. Plane, Effect of ice particles on the mesospheric potassium layer at Spitsbergen (78°N), *J. Geophys. Res.*, *112*, D08307, 2007.

Ramos, C., M. C. Kelley, F. T. Djuth, K. M. Groves, Y. Murayama, S. Kawamura, and D. Thorsen, Multifrequency observations of polar mesosphere summer echoes using alaskan radar facilities: Comparison and scattering calculations, *Radio Sci.*, *44*, RS5011, 2009.

Rapp, M., et al., First in situ measurement of the vertical distribution of ice volume in a mesospheric ice cloud during the ECOMA/MASS rocket-campaign, *Ann. Geophys.*, *27*, 755–766, 2009.

Rapp, M., and F.-J. Lübken, Electron temperature control of PMSE, *Geophys. Res. Lett.*, *27*, 3285–3288, 2000.

Rapp, M., and F.-J. Lübken, Modelling of particle charging in the polar summer mesosphere: Part 1 – general results, *J. Atmos. Sol. Terr. Phys.*, *63*, 759–770, 2001.

Rapp, M., and F.-J. Lübken, On the nature of PMSE: Electron diffusion in the vicinity of charged particles revisited, *J. Geophys. Res.*, *108(D8), 8437, doi:10.1029/2002JD002857*, 2003.

Rapp, M., and F.-J. Lübken, Polar mesosphere summer echoes (PMSE): Review of observations and current understanding, *Atmos. Chem. Phys.*, *4*, 2601–2633, 2004.

Rapp, M., and F.-J. Lübken, Comment on "ice iron/sodium film as cause for high noctilucent cloud radar reflectivity" by P. M. Bellan, *J. Geophys. Res.*, *114, D11204*, 2009.

Rapp, M., and G. E. Thomas, Modeling the microphysics of mesospheric ice particles: Assessment of current capabilities and basic sensitivities, *J. Atmos. Sol. Terr. Phys.*, *68*, 715–744, 2006.

Rapp, M., F.-J. Lübken, A. Müllemann, G. E. Thomas, and E. J. Jensen, Small scale temperature variations in the vicinity of NLC: Experimental and model results, *J. Geophys. Res.*, *107(D19), doi:10.1029/2001JD001241*, 2002.

Rapp, M., F.-J. Lübken, and T. A. Blix, The role of charged ice particles for the creation of PMSE: A review of recent developments, *Adv. Space Res.*, *31(9)*, 2033–2043, 2003a.

Rapp, M., F.-J. Lübken, P. Hoffmann, R. Latteck, G. Baumgarten, and T. A. Blix, PMSE dependence on aerosol charge number density and aerosol size, *J. Geophys. Res.*, *108(D8), 8450, doi:10.1029/2002JD002650*, 2003b.

Rapp, M., I. Strelnikova, and J. Gumbel, Meteoric smoke particles: Evidence from rocket and radar techniques, *Adv. Space Res.*, *40*, 809–817, 2007.

Rapp, M., I. Strelnikova, R. Latteck, P. Hoffman, U.-P. Hoppe, I. Häggström, and M. Rietveld, Polar mesospher summer echoes (PMSE) studied at Bragg wavelengths of 2.8 m, 67 cm, and 16 cm, *J. Atmos. Sol. Terr. Phys.*, *doi: 10.1016/j.jastp.2007.11.005*, 2008.

Reid, G. C., Ice particles and electron "bite-outs" at the summer polar mesopause, *J. Geophys. Res.*, *95*, 13,891–13,896, 1990.

Reid, G. C., Vertical wind convergence and the formation of aerosol layers in the upper mesosphere, *Geophys. Res. Lett.*, *24*, 1997.

Reid, I. M., R. Rüster, P. Czechowsky, and G. Schmidt, VHF radar measurements of momentum flux in the summer polar mesosphere over Andenes (69°N, 16°E), Norway, *Geophys. Res. Lett.*, *15*, 1263–1266, 1988.

Robertson, S., et al., Mass analysis of charged aerosol particles in NLC and PMSE during the ECOMA/MASS campaign, *Ann. Geophys.*, *27*, 1213–1232, 2009.

Roble, R. G., and R. E. Dickinson, How will changes in carbon dioxide and methane modify the mean structure of the mesosphere and thermosphere?, *Geophys. Res. Lett.*, *16*, 1441–1444, 1989.

Röttger, J., The MST radar technique, *MAP Handbook*, *13*, 797–808, 1984.

Röttger, J., Observations of the polar D-region and the mesosphere with the EISCAT Svalbard Radar and the SOUSY Svalbard Radar, *Mem. Nat. Inst. Pol. Res.,*, *54*, 9–20, 2001.

Röttger, J., and C. LaHoz, Characteristics of polar mesosphere summer echoes (PMSE) observed with the EISCAT 224 MHz radar and possible explanations of their origin, *J. Atmos. Terr. Phys.*, *52*, 893–906, 1990.

Röttger, J., C. La Hoz, M. C. Kelley, U.-P. Hoppe, and C. Hall, The structure and dynamics of polar mesosphere summer echoes observed with the EISCAT 224 MHz radar, *Geophys. Res. Lett.*, *15(12)*, 1353–1356, 1988.

Röttger, J., M. T. Rietveld, C. LaHoz, C. Hall, M. C. Kelley, and W. Swartz, Polar mesosphere summer echoes observed with the EISCAT 933-MHz radar and the CUPRI 46.9MHz radar, their similarity to 224 MHz radar echoes and their relation to turbulence and electron density profiles, *Radio Sci.*, *25*, 671–687, 1990.

Shimogawa, M., and R. H. Holzworth, Electric field measurements in a NLC/PMSE region during the MASS/ECOMA campaign, *Ann. Geophys.*, *27*, 1423–1430, 2009.

Singer, W., D. Keuer, P. Hoffmann, P. Czechowsky, and G. Schmidt, The ALOMAR-SOUSY-radar: Technical design and further developments, *Proceedings of the 12th ESA Symposium on European Rocket and Balloon Programmes and Related Research, Lillehammer, Norway (ESA SP–370)*, pp. 409–415, 1995.

Smiley, B., S. Robertson, M. Horanyi, T. Blix, M. Rapp, R. Latteck, and J. Gumbel, Measurement of negatively and positively charged particles inside PMSE during MIDAS SOLSTICE 2001, *J. Geophys. Res.*, *108(D8), 8444, doi: 10.1029/2002JD002425*, 2003.

Strelnikov, B., In situ measurements of small scale neutral and plasma dynamics in the mesosphere/lower thermosphere region, *Ph.D thesis*, *Universität Rostock, Rostock, Germany*, 2006.

Strelnikov, B., M. Rapp, T. A. Blix, N. Engler, J. Höffner, J. Lautenbach, F.-J. Lübken, B. Smiley, and M. Friedrich, In situ observations of small scale neutral and plasma dynamics in the mesosphere/lower thermosphere at 79°N, *Adv. Space Res.*, *38*, 2388–2393, 2006.

Strelnikov, B., M. Rapp, I. Strelnikova, N. Engler, and R. Latteck, Small-scale structures in neutrals and charged aerosol particles as observed during the ECOMA/MASS rocket campaign, *Ann. Geophys.*, *27(4)*, 1449–1456, 2009.

Strelnikova, I., et al., Measurements of meteor smoke particles during the ECOMA-2006 campaign: 2. Results, *J. Atmos. Sol. Terr. Phys.*, *71*, 486–496, 2009.

Strelnikova, I., and M. Rapp, Studies of polar mesosphere summer echoes with the EISCAT VHF and UHF radars: Information contained in the spectral shape, *Adv. Space Res.*, *45*, 247–259, 2010.

Strelnikova, I., and M. Rapp, Majority of PMSE spectral widths at UHF and VHF are compatible with a single scattering mechanism, *J. Atmos. Sol. Terr. Phys.*, *73*, 2142–2152, 2011.

Strelnikova, I., M. Rapp, S. Raizada, and M. Sulzer, Meteor smoke particle properties derived from Arecibo incoherent scatter radar observations, *Geophys. Res. Lett.*, *34*, L15815, 2007.

Tanenbaum, B. S., Continuum theory of Thomson scattering, *Phys. Rev.*, *171*, 215–221, 1968.

Tatarskii, V. I., The effects of the turbulence atmosphere on wave propagation, *Isr. Program for Sci. Transl.*, *Jerusalem*, 1971.

Thomas, G. E., Mesopheric clouds and the physics of the mesopause region, *Rev. Geophys*, *29*, 553–575, 1991.

Thomas, G. E., Is the polar mesosphere the miner's canary of global change?, *Adv. Space Res.*, *18(3)*, 149–158, 1996.

Thomas, G. E., J. J. Olivero, E. J. Jensen, W. Schröder, and O. B. Toon, Relation between increasing methane and the presence of ice clouds at the mesopause, *Nature*, *338*, 490–492, 1989.

Thomas, L., I. Astin, and I. T. Prichard, The characteristics of VHF echoes from the summer mesopause region at mid-latitudes, *J. Atmos. Terr. Phys.*, *54*, 969–977, 1992.

Trakhtengerts, V. Y., Generation mechanism of polar mesosphere summer echoes, *J. Geophys. Res.*, *99*, 21,083–21,088, 1994.

Trakhtengerts, V. Y., and A. G. Demekhov, Nonequilibrium electron density fluctuations and wave scattering in the mesosphere, *J. Atmos. Terr. Phys.*, *57*, 1153–1164, 1995.

Turunen, E., P. N. Collis, and T. Turunen, Incoherent scatter spectral measurements of the summertime high-latitude D-region with the EISCAT UHF-incoherent scatter radar, *J. Atmos. Terr. Phys.*, *50*, 289, 1988.

Turunen, T., I. H. A. Westman, and G. Wannber, High resolution general purpose D-layer experiment for EISCAT incoherent scatter radars using selected set of random codes, *Ann. Geophys.*, *20*, 1469–1477, 2002.

Ulwick, J. C., K. D. Baker, M. C. Kelley, B. B. Balsley, and W. L. Ecklund, Comparison of simultaneous MST radar and electron density probe measurements during STATE, *J. Geophys. Res.*, *93*, 6989–7000, 1988.

Varney, R. H., M. J. Nicolls, C. J. Heinselman, and M. C. Kelley, Observations of polar mesospheric summer echoes using PFISR during the summer of 2007, *J. Atmos. Sol. Terr. Phys.*, *71*, 470–476, 2007.

Varney, R. H., M. C. Kelley, M. J. Nicolls, C. J. Heinselman, and R. L. Collins, The electron density dependence of polar mesospheric summer echoes, *J. Atmos. Sol. Terr. Phys.*, *73*, 2153–2165, 2011.

von Savigny, C., S. V. Petelina, E. J. L. B. Karlsson, D. A. Degenstein, N. D. Loyd, and J. P. Burrows, Vertical variation of NLC particle sizes retrieved from Odin/OSIRIS limb scattering observations, *Geophys. Res. Lett.*, *32*, L07806, 2005.

von Savigny, C., C. Robert, H. Bovensmann, J. P. Burrows, and M. Schwartz, Satellite observations of the quasi 5-day wave in noctilucent clouds and mesopause temperatures, *Geophys. Res. Lett.*, *34*, L24808, 2007.

von Zahn, U., and U. Berger, Persistent ice cloud in the midsummer upper mesosphere at high latitudes: Three-dimensional modeling and cloud interactions with ambient water vapor, *J. Geophys. Res.*, *108(D8), 8451, doi:10.1029/2002JD002409*, 2003.

von Zahn, U., and J. Bremer, Simultaneous and common-volume observations of noctilucent clouds and polar mesosphere summer echoes, *Geophys. Res. Lett.*, *26*, 1521–1524, 1999.

von Zahn, U., G. von Cossart, J. Fiedler, K. Fricke, G. Nelke, G. Baumgarten, D. Rees, A. Hauchecorne, and K. Adolfsen, The ALOMAR Rayleigh/Mie/Raman lidar: Objectives, configuration, and performance, *Ann. Geophys.*, *18*, 815–833, 2000.

Wannberg, U. G., I. Wolf, L. G. Vanheinen, K. Koskeniemi, J. Röttger, and et al., The EISCAT Svalbard Radar: A case study in modern incoherent scatter radar design, *Radio Sci.*, *32*, 2283–2307, 1997.

Witt, G., The nature of noctilucent clouds, *Space Res.*, *IX*, 157–169, 1969.

Woodman, R. F., and A. Guillen, Radar observations of winds and turbulence in the stratospahere and mesosphere, *J. Atmos. Sci.*, *31*, 493–505, 1974.

Woods, J. D., V. Högström, P. Misme, H. Ottersten, and O. M. Phillips, Fossil turbulence, *Radio Sci.*, *4*, 1365–1367, 1969.

Zecha, M., and J. Röttger, Occurrence of polar mesosphere summer echoes at very high latitudes, *Ann. Geophys.*, *27*, 1331–1342, 2009.

Zecha, M., J. Bremer, R. Latteck, and W. Singer, Properties of midlatitude mesosphere summer echoes after three seasons of VHF radar observations at 54°N, *J. Geophys. Res.*, *108(D8), 8439, doi:10.1029/2002JD002442*, 2003.

Acknowledgments

First and foremost I would like to thank my supervisor Prof. Dr. Markus Rapp for all his contributions of help, support, and encouragement to my Ph.D. thesis. His joy and enthusiasm in the research always inspired and motivated me. This thesis would not have been possible without his invaluable advices and brilliant ideas. More to that, I grateful appreciate his friendly help and continuous support for my life in Germany. Special gratitude goes to Prof. Franz-Josef Lübken for providing me this excellent opportunity to work at IAP as well as for the suggestions and comments on the work of my thesis. I would also like to spread thanks to Prof. Tom A. Blix (University of Oslo, Norway) and again Prof. Markus Rapp for their willingness to review this thesis and for their insightful comments and suggestions making this thesis better and better.

Prof. Jürgen Röttger (MPS, Germany) and Prof. Jian Wu (CRIRP, China) recommended me to IAP. I also gratefully thank Jürgen Röttger for introducing me to the EISCAT radars and data analysis as well as many suggestions and ideas on the radar calibration.

I thank Manja Placke and Yi Liu for their efforts to correct English grammar and to fix problems in the manuscript of this thesis.

Dr. Mark Hervig (Gats Inc., USA), Dr. Gerd Baumgarten, and Prof. Chris Hall (University of Tromsø, Norway) provided the SOFIE data, AMOMAR RMR Lidar data, and Svalbard wind data, respectively. I greatly thank their contributions to complete the work of this thesis.

I greatly appreciate many valuable discussion on the EISCAT data analysis with Dr. Irina Strelnikova, Dr. Norbert Engler, and Georg Teiser. I also thank Irina for many helps on modeling and programming. Thanks are further spread to all my friends and colleagues of Department Radar sounding and sounding rockets, specially to Dr. Ralph Latteck and Dr. Marius Zecha for valuable discussion on data analysis of the SOUSY Svalbard Radar, to Dr. Peter Hoffmann for providing me Lyman-α data, and to Prof. Markus Rapp, Dr. Irina Strelnikova, Dr. Boris Strelnikov, Rosemarie von Rein, Toralf Renkwitz and Manja Placke for friendly helps to deal with the trivial personal problems popping up frequently.

I am gratefully indebted to all the colleagues of IAP for building this extremely nice working atmosphere. Big thanks are addressed but not restricted to Marion Strate, Angelika Kurreck, Renate Waschow, Angelika Ruβ, and Norbert Meesen for administrative supports as well as to Thomas Linow and Peter Schubert for computer supports. I would also like to thank Toralf Renkwitz, Dr. Norbert Engler, Anne Theuerkauf, Carsten Baumann and many others to pick me up for daily commute.

I would also like to address big thanks to the EISCAT staff for their continuous technical supports, specially to Dr. Mike Rietveld, Dr. Ingemar Häggström, and Dr. Assar Westman for their efforts to meet my requests regarding data layout and data analysis.

Furthermore, Prof. Jian Wu, Prof. Zhengwen Xu, and Dr. Jun Wu from CRIRP, China, always gave me great supports for dealing with personal issues in China. I thank them for friendly and continuous helps. I would also like to thank Prof. Ruiyuan Liu (PRIC, China) for his concern and help.

Last but not least I am deeply grateful to my parents for permanent support and encouragement during all my life. I am specially indebted to my wife Yi Liu for her loving supports and patience even during the tough times of my Ph.D. pursuit as well as my beloved daughter Chuqiao Li (Koukou) whose birth made our life more joyful and brilliant. Of course two grandmas deserved big thanks for their helps early after Chuqiao's birth, which made it possible that I can concentrate on this thesis preparation.

Erklärung

Hiermit versichere ich an Eides statt, dass ich die vorliegende Arbeit selbstständig angefertigt und ohne fremde Hilfe verfasst habe, keine außer den von mir angegebenen Hilfsmitteln und Quellen dazu verwendet habe und die den benutzten Werken inhaltlich oder wörtlich entnommenen Stellen als solche kenntlich gemacht habe.

Die Arbeit wurde bisher weder im Inland noch im Ausland in gleicher oder ähnlicher Form einer anderen Prüfungsbehörde vorgelegt. Weiterhin erkläre ich, dass ich ein Verfahren zur Erlangung des Doktorgrades an keiner anderen wissenschaftlichen Einrichtung beantragt habe.

Li Qiang

Kühlungsborn, den 18. März 2011

Lebenslauf

Name	Qiang Li
Geburtsdatum	17.06.1979
Geburtsort	Hebei, China
Familienstand	verheiratet
Staatsangehörigkeit	China
Wohnsitz	Hebei, China
Nebenwohnsitz	Rostock, Deutschland

1986 – 1992	Grundschule Nanjiedong, Hebei, China
1992 – 1995	Allgemeinbildende Mittelschule Chewang, Hehei, China
1995 – 1998	Allgemeinbildende Mittelschule Weixian Nr. 1, Hebei, China
1998 – 1999	Allgemeinbildende Mittelschule Handan Nr. 1, Hebei, China
Juni 1999	Abitur
1999 – 2003	Studium an der Universität Wuhan, Wuhan, China, Studiengang: Bachelor Physik
2003 – 2004	Studium an der Universität Xidian, Xi'an, China, Studiengang: Master Elektromagnetisches Feld
2004 – 2006	Masterarbeit an CRIRP, Beijing, China zum Thema: "Research on the Long-term Trends of Solar Activity and Ionospheric Behaviors"
seit Nov. 2006	Doktorand in am Leibniz-Institut für Atmosphärenphysik e.V. an der Universität Rostock, Anfertigung der Dissertation